2016

MODELLING OF THE NANOWIRE CdS-CdTe DEVICE DESIGN FOR ENHANCED QUANTUM EFFICIENCY IN WINDOW-ABSORBER TYPE SOLAR CELLS

Rasika Ganvir
University of Kentucky, rasikaganvir@gmail.com
Digital Object Identifier: http://dx.doi.org/10.13023/ETD.2016.036

STUDENT AGREEMENT:

I represent that my thesis or dissertation and abstract are my original work. Proper attribution has been given to all outside sources. I understand that I am solely responsible for obtaining any needed copyright permissions. I have obtained needed written permission statement(s) from the owner(s) of each third-party copyrighted matter to be included in my work, allowing electronic distribution (if such use is not permitted by the fair use doctrine) which will be submitted to UKnowledge as Additional File.

I hereby grant to The University of Kentucky and its agents the irrevocable, non-exclusive, and royalty-free license to archive and make accessible my work in whole or in part in all forms of media, now or hereafter known. I agree that the document mentioned above may be made available immediately for worldwide access unless an embargo applies.

I retain all other ownership rights to the copyright of my work. I also retain the right to use in future works (such as articles or books) all or part of my work. I understand that I am free to register the copyright to my work.

REVIEW, APPROVAL AND ACCEPTANCE

The document mentioned above has been reviewed and accepted by the student's advisor, on behalf of the advisory committee, and by the Director of Graduate Studies (DGS), on behalf of the program; we verify that this is the final, approved version of the student's thesis including all changes required by the advisory committee. The undersigned agree to abide by the statements above.

Rasika Ganvir, Student

Dr. Vijay P. Singh, Major Professor

Dr. Caicheng Lu, Director of Graduate Studies

MODELLING OF THE NANOWIRE CdS-CdTe DEVICE DESIGN FOR ENHANCED QUANTUM EFFICIENCY IN WINDOW-ABSORBER TYPE SOLAR CELLS

THESIS

A thesis submitted in partial fulfillment of the
Requirements for the degree of Master of Science in Electrical
Engineering in the College of Engineering at the
University of Kentucky

By
Rasika Ganvir
Lexington, Kentucky

Director: Dr. Vijay P. Singh
Professor of Electrical and Computer Engineering
University of Kentucky
Lexington, Kentucky
2016

ABSTRACT OF THESIS

Numerical simulations of current-voltage characteristics of nanowire CdS/CdTe solar cells are performed as a function of temperature using SCAPS-1D. This research compares the experimental current-voltage (I-V) characteristics with the numerical (I-V) simulations obtained from SCAPS-1D at various temperatures. Various device parameters were studied which can affect the efficiency of the nanowire-CdS/CdTe solar cell. It was observed that the present simulated model explains the important effects of these solar cell devices, such as the crossover and the rollover effect. It was shown that the removal of defect in i-SnO_2 is responsible for producing the crossover effect. In the past, the rollover effect has been explained by using back to back diode model in the literature. In this work, simulations were performed in order to validate this theory. At the back electrode, the majority carrier barrier height was varied from 0.4 to 0.5 eV, the curve corresponding to the 0.5 eV barrier showed a strong rollover effect, while this effect disappeared when the barrier was reduced to 0.4 eV. Thus, it was shown that the change of barrier height at the contact is a critical parameter in the rollover effect.

Keywords: Nanowire Cadmium Sulfide; Cadmium Telluride; Solar Cells, SCAPS-1D, Simulation; Interface States

RASIKA GANVIR

March 7, 2016

MODELLING OF THE NANOWIRE CDS-CDTE DEVICE DESIGN FOR ENHANCED QUANTUM EFFICIENCY IN WINDOW-ABSORBER TYPE SOLAR CELLS

By

RASIKA GANVIR

Dr. Vijay P. Singh
Director of Thesis

Dr. Caicheng Lu
Director of Graduate Studies

March 7, 2016

Dedicated to my Husband

Kaustubh Ghodeswar

Acknowledgments

I would like to sincerely thank my academic advisor and thesis committee chairperson Dr. Vijay Singh for his invaluable guidance, encouragement and time during my Master's program, and for giving me an opportunity to work in his lab. I appreciate his knowledge in the field and his willingness to share it with me. His appetite for research and his kind and helpful nature always inspire me to work hard.

I would like to thank my thesis committee members Dr. Todd Hastings and Dr. Donald Colliver for their encouragement and valuable time to review my thesis.

I would like to thank Dr. Mark Burgelman for providing SCAPS-1D software. I wish to thank Dr. Praveen Kumar Sivakumar and Karen Sampson, with whom I performed the simulations mentioned in this thesis and for their valuable insights. I wish to thank Dr. Hongmei Dang for providing the experimental data.

I sincerely appreciate love and help from my friends especially Samaneh, Jayanti, Shreya and Mansoor, who encouraged me during this phase of my life.

I would like to thank my parents for being always patient, calm and supportive throughout my life. I would like to thank my husband Kaustubh who has motivated and inspired me to pursue this dream. His constant support has made this dream come true.

March 7, 2016

Table of Contents

List of Figures

List of Tables

1. Introduction

1.1. Solar cells

The conventional energy sources like fossil fuels are going to deplete over the years and thus, the world is beginning to focus on renewable energy sources. The solar energy is abundant as well as environmentally friendly. It is versatile and the solar technology is making significant advances over the years.

Since 2010, the world has added more solar photovoltaic (PV) capacity than in the previous four decades. The solar photovoltaic global capacity has been increased to 177 Gigawatts in 2014, with an increase of 40 GW from 2013. [1] Figure1.1 shows the solar PV generation and projection until 2020 [2].

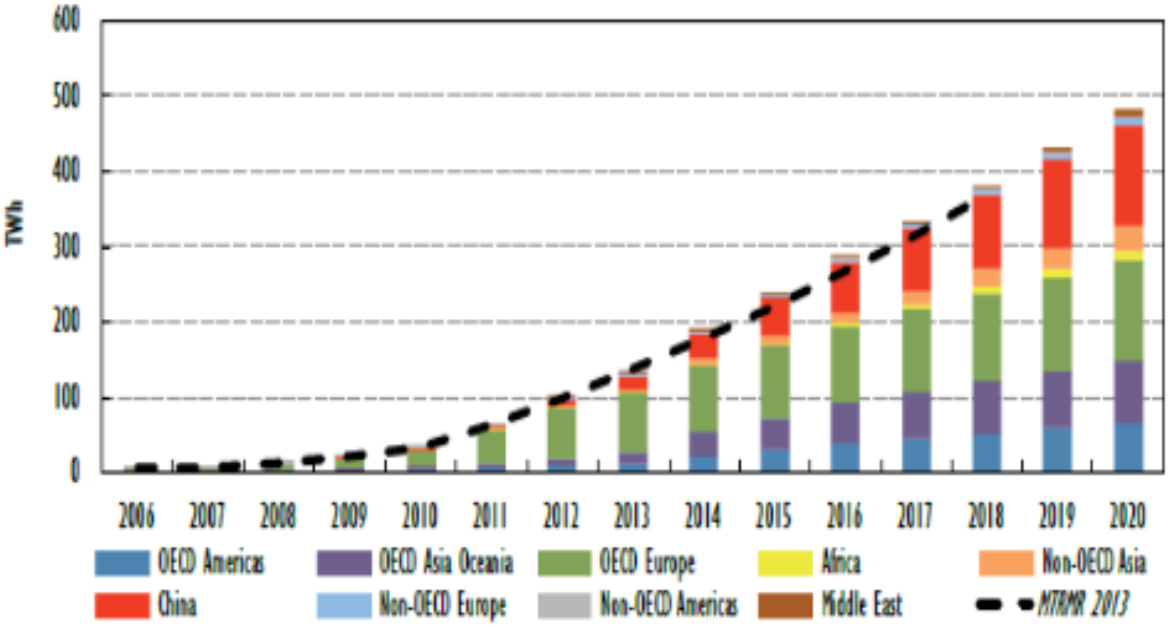

Figure 1.1 Solar PV generation and projection by region

Figure1.2 shows the roadmap for PV's share of global electricity reaching 16% by 2050, a significant increase from the 11% goal in the 2010 roadmap [3].

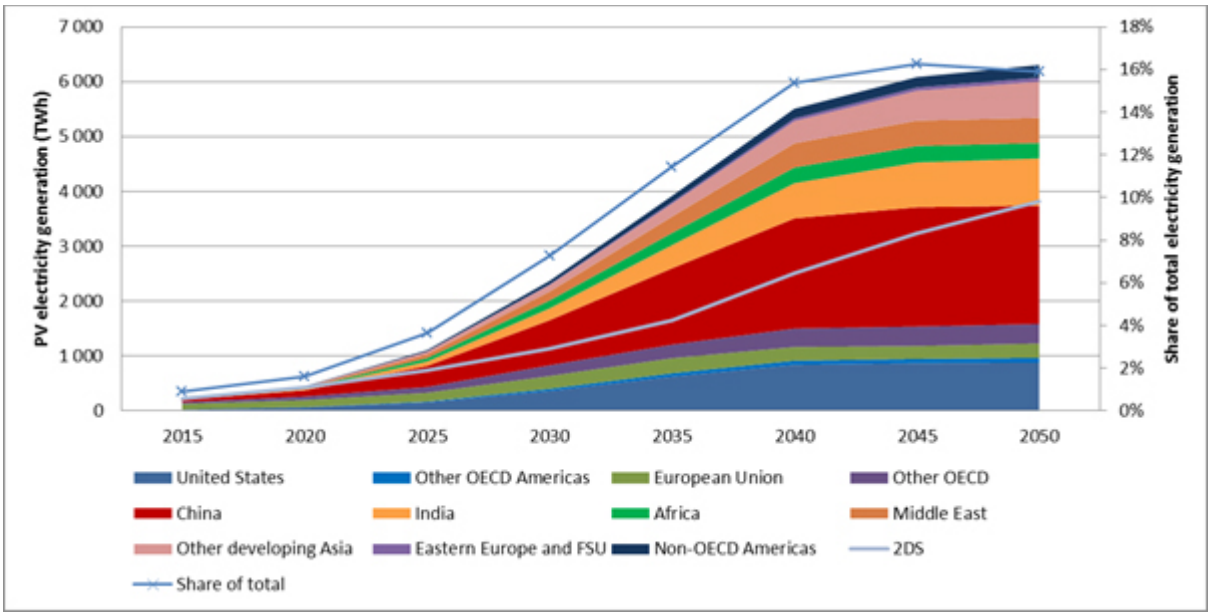

Figure 1.2 Regional production of PV electricity envisioned in the roadmap

The global investment in solar energy sector has increased by 25% in 2014 over 2013. Figure1.3 shows the global new investment in Renewable energy [1].

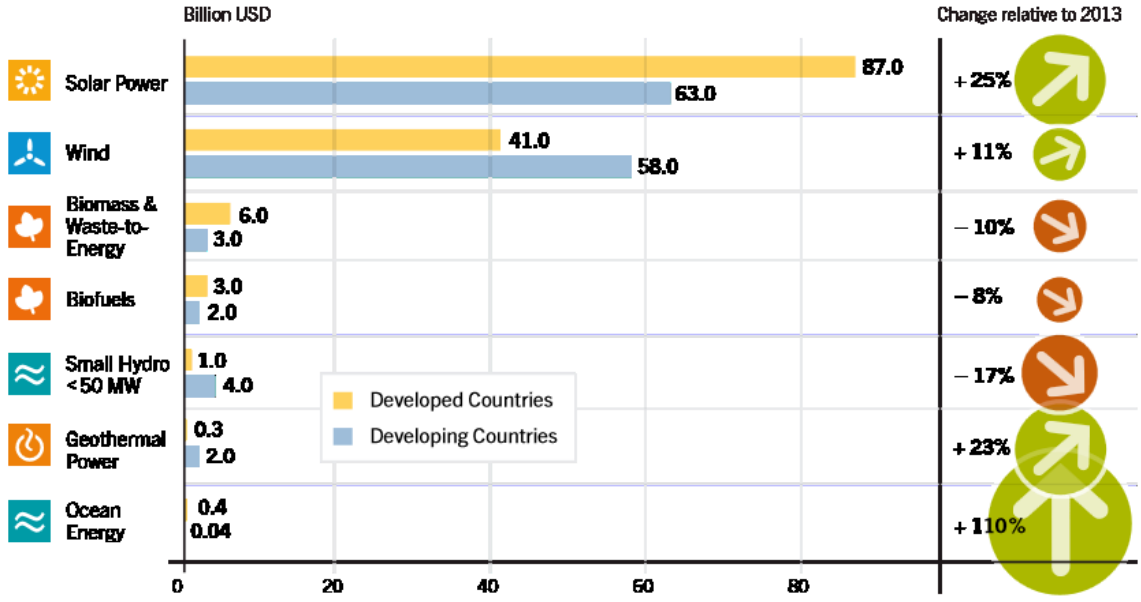

Figure 1.3 Global New Investment in Renewable Energy by Technology, Developed and Developing Countries, 2014

1.1.1 History of solar cells

The photovoltaic effect was discovered by French physicist Alexandre-Edmond Becquerel in 1839. This was the beginning of the solar cell technology. In 1905, Albert Einstein published his paper on photoelectric effect that explained very well the absorption of the photons regarding to the frequency of light. Audobert and Stora discover the photovoltaic effect in cadmium sulfide (CdS) in 1932 [4]. Russell Ohl observed the first photovoltaic effect of substantial EMF voltage on a silicon p-n junction in 1940 [5]. In 1954, Gerald Pearson, Daryl Chapin and Calvin Fuller, at Bell Laboratories discovered a silicon solar cell, which was the first material to directly convert sunlight into electricity to run electrical devices. The efficiency of this silicon solar cell, was 4%, which later increased to 11% [5]. Over several decades, different types of solar cells (multi-junction) using new materials have been fabricated in order to improve the efficiency of solar cells to reach Shockley – Queisser limit.

1.1.2 Generations of solar cells

Solar cells are mainly categorized into three generations. The first generation of solar cells has the major portion of the present market. The benefits of this solar cell technology are good performance and high stability. The materials use for this generation solar cells include GaAs and crystalline Silicon However, the production costs is high due to high energy in production and material costs mostly for the silicon wafer. This generation of solar cells has higher efficiency (around 40%) as shown in Figure1.4 [6].

The second generation of solar cells managed to reduce the material cost by eliminating the use of silicon wafer and replacing it with thin-film technology. This technology is based on amorphous silicon, CIGS, CdTe etc. where the typical efficiency is around 20% (Figure 1.4). The energy consumption associated with the production of these solar cells is quite high due to the use of vacuum processes and high temperature treatments.

The third generation of solar cells includes Quantum Dot, Polymer, Perovskite, Nanocrystalline and Dye- sensitized solar cells. The benefits of these types of solar cells are low cost and large scale production capability with flexibility. The disadvantages are low efficiency and low stability compared to traditional solar cells.

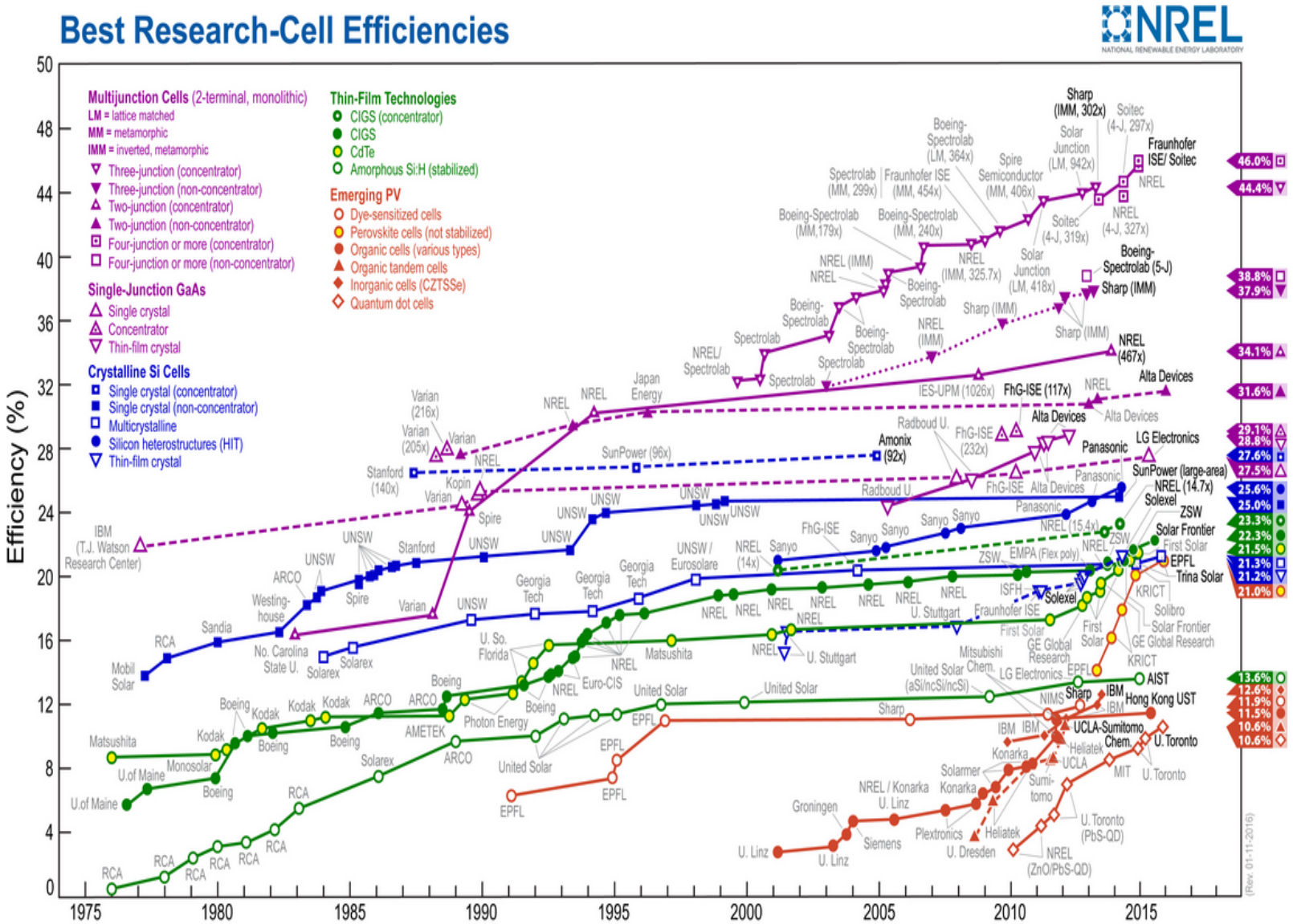

Figure 1.4 Best Research Cell efficiencies of three generations of solar cells, Source: National Renewable Energy Laboratory [6]

1.2. Basics of solar cells

1.2.1. Photovoltaic effect and P-N junction theory

The discovery of the photovoltaic effect was the major step towards the invention of solar cells. The photovoltaic effect is a physical and chemical phenomenon. It is the creation of voltage or electric current in the material when the light is exposed on it.

P-N junction is formed by the P-type and N-type semiconductor. If the material used in the p-type and n-type semiconductor is same, it is called as the homojunction. When the materials used for p-type and n-type are different, it is called as the heterojunction.

Figure 1.5 shows the abrupt p-n junction in equilibrium. The diffusion process occurs because of the thermal gradient and scattering. The electrons and holes migrate from the high concentration to low concentration region in order to reach an equilibrium. During this process, the electrons and holes are removed from n-type and p-type regions respectively, which creates uncompensated donor and acceptor ions as shown in Figure1.5 [5]. This region is called as the depletion region as it is depleted from the free electrons and holes.

The uncompensated charge creates an electric field which is also referred to as the built-in field. There is a difference between the electric potential at the edges of the depletion layer due to the built-in electric field, which is called as built-in voltage (Vbi). The current due to the built-in field is called as drift current. In equilibrium diffusion current is equal to the drift current.

The solar cell is essentially a p-n junction device, where n-type material is kept thin to allow light to pass through the solar cell. Light is composed of photons. When the photon is incident on the material and if the energy of photon is greater than the energy band gap of the material, an electron-hole pair is created.

Once the electron – hole pair is created in n and p type regions, most electrons combine with majority carriers (i.e. holes) in p-type and most holes combine with majority carriers (i.e. electrons) in n-type. Only those carriers which have not been combined with majority carriers can move towards the other region, resulting the photocurrent. It depends upon the diffusion length and carrier lifetime. The diffusion length is the distance, carriers can diffuse in carrier lifetime before they are annihilated. [5]

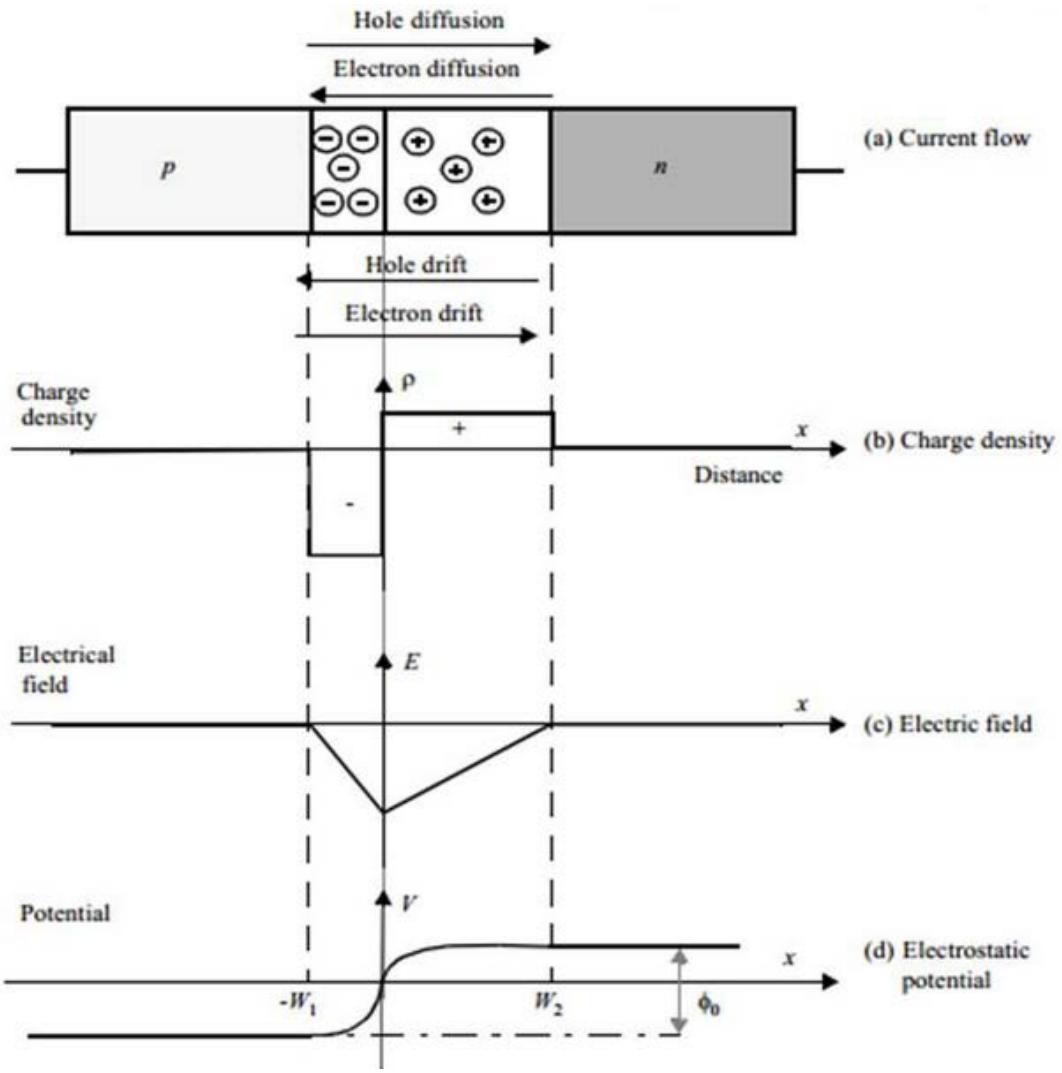

Figure 1.5 Abrupt p-n junction under equilibrium bias [5]

1.2.2. Quantum efficiency

Quantum efficiency is the ratio of the number of charge carriers collected by a solar cell to the number of photons of a given energy incident on the solar cell. It is related to the response of a solar cell to the various wavelengths in the spectrum of light which is incident on the cell. Thus, the quantum efficiency is expressed as a function of either wavelength or energy.

There are two type of quantum efficiency of a solar cell. External quantum efficiency (EQE) considers the losses due to the recombination, transmission and reflection losses. It is the ratio of number of charge carriers collected by the solar cell to the number of

incident photons of a given energy. Internal quantum efficiency (IQE) is the efficiency with which light not transmitted through or reflected away from the cell can generate charge carriers—specifically electrons and holes—that can generate current. By measuring the transmission and reflection of a solar device, the external QE curve can be corrected to obtain the internal QE curve. [7]

Figure1.6 [8] shows the the curve of external quantum efficiency as a function of wavelenth. The quantum efficiency is reduced by the surface recombination , reflection and low diffusion length. The quantum efficency is also dependent on the series and shunt resistance, energy bandgap and temperature.

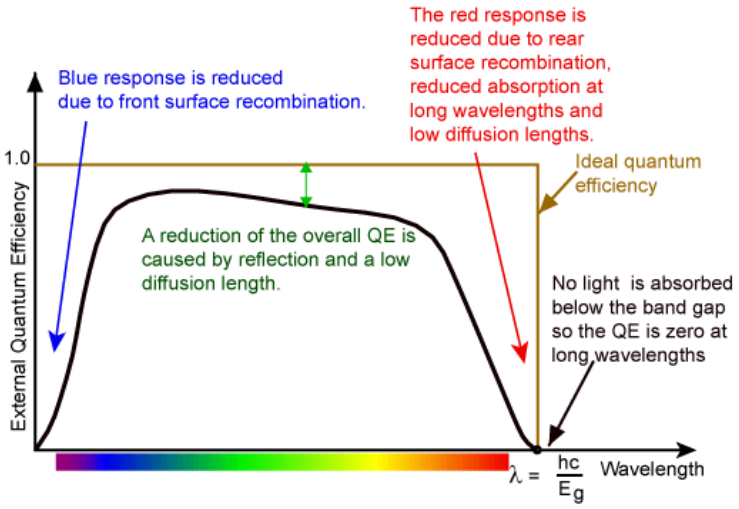

Figure 1.6 External quantum efficency as a function of wavelength [8]

1.2.3. I-V characteristics of a solar cell

The equivalent circuit of the solar cell consists of the constant current source I_L and a diode as shown in Figure1.7 [5]. I_L denotes the photocurrent, R_L is the load resistance, I_s is the diode saturation current.

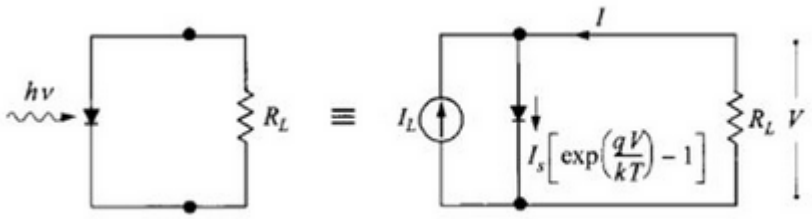

Figure 1.7 Equivalent circuit of a solar cell in light conditions [5]

The dark I-V characteristics of the solar cell follow the ideal I-V characteristics of a diode and is given by the following equation:

$$I(dark) = I_s\left[\exp\left(\frac{qV}{kT}\right) - 1\right] \quad (1)$$

Where, k is Boltzmann constant

The ideal saturation current for the solar cell is given by

$$I_s = AqN_CN_V\left(\frac{1}{N_A}\sqrt{\frac{D_n}{\tau_n}} + \frac{1}{N_D}\sqrt{\frac{D_p}{\tau_p}}\right)exp\left(\frac{-E_g}{kT}\right) \quad (2)$$

From the above equation, it can be observed that the saturation current depends on diffusion coefficient of minority carriers (D_n, D_p), energy bandgap (E_g), carrier lifetime (τ_n , τ_p), Donor impurity concentration (N_d), Acceptor impurity concentration (N_a) , Effective density of states in conduction band (N_c) and valence band (N_v).

The total current is the summation of dark current and the photocurrent (I_L), which is given by:

$$I = I_s\left[\exp\left(\frac{qV}{kT}\right) - 1\right] - I_L \quad (3)$$

The above equation depicts the total I-V characteristics of the solar cell under illumination.

The open circuit voltage (V_{oc}) is the maximum voltage available from a solar cell, which occurs when the current is zero. The equation for V_{oc} can be derived by putting the value of current to be zero in equation (3), which is given by

$$V_{oc} = \frac{kT}{q} ln\left(\frac{I_L}{I_s} + 1\right) \approx \frac{kT}{q} ln\left(\frac{I_L}{I_s}\right) \qquad (4)$$

The open circuit voltage increases logarithmically with the decrease in the saturation current.

The short circuit current (I_{sc}) is the current through the solar cell when the voltage across the solar cell is zero. In the ideal case, the short circuit current is equal to the photocurrent.

The typical I-V curve of the solar cell is shown in the Figure 1.8[9].

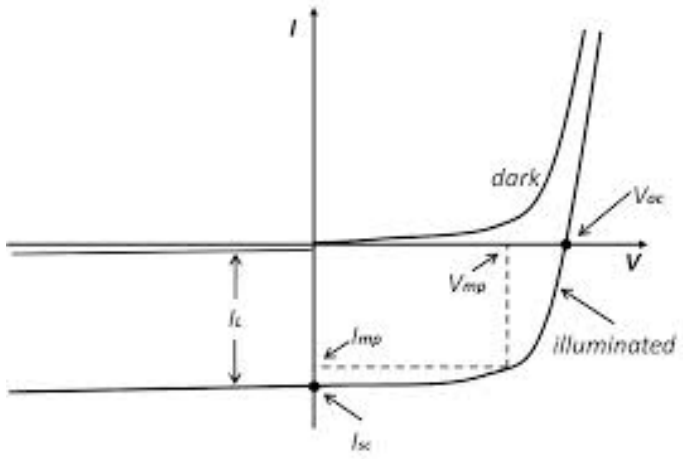

Figure 1.8 I-V characteristics of a solar cell under illumination [9]

The output power cannot be determined by the short circuit current (V=0) and open circuit voltage (I=0). It is given by the following equation

$$P = IV = I_s V\left[\exp\left(\frac{qV}{kT}\right) - 1\right] - I_L V \qquad (5)$$

The maximum power is obtained when dP/dV=0

The maximum current and maximum voltage are given by:

$$I_m = I_s \beta V_m \exp(\beta V_m) \approx I_L \left(1 - \frac{1}{\beta V_m}\right) \quad (6)$$

$$V_m = \frac{1}{\beta} ln \left[\frac{(I_L/I_S)+1}{1+\beta V_m}\right] \approx V_{oc} - \frac{1}{\beta} \ln(1 + \beta V_m) \quad (7)$$

where, β=q/kT.

The maximum power thus obtained is given by

$$P_m = I_m V_m = F_F I_{sc} V_{oc} \approx I_L \left[V_{oc} - \frac{1}{\beta} \ln(1 + \beta V_m) - \frac{1}{\beta}\right] \quad (8)$$

The fill factor is another important parameter in solar cell theory. It measures the sharpness of the I-V curve.

$$F_F \equiv \frac{I_m V_m}{I_{sc} V_{oc}} \quad (9)$$

The ideal conversion efficiency is given by the ratio of the maximum power output to the incident power P_{in}

$$\eta = \frac{P_m}{P_{in}} = \frac{I_m V_m}{P_{in}} = \frac{V_m^2 I_s (q/kT) \exp(qV_m/kT)}{P_{in}} \quad (10)$$

To optimize the maximum efficiency, optimum value of the energy bandgap is used.

1.3 Background On The Solar Cell Devices, Which Were Studied Through Simulation

1.3.1. Device Design

The device fabricated comprises of CdS nanowires which are embedded in a transparent anodized aluminum oxide (AAO) matrix. This device has been fabricated by Dr. Hongmei Dang for her PhD work [10]. The experimental procedures, figures 1.9-1.12 and the experimental results presented here are obtained from her dissertation.

The schematic structure of the solar cell comprising of planar CdS and its carrier transport process is shown in figures 1.9 A and C respectively. Figure 1.9 B shows the structure of Nanowire CdS solar cell. Figure 1.9 D shows the carrier transport process of nanowire CdS/CdTe solar cell [10].

The use of AAO matrix and CdS nanowires in the nanowire CdS/CdTe solar cell resulted in the better transmittance of incident light, which improved the short circuit current. The open circuit voltage was improved due to the reduction of interface recombination and decreased effective reverse saturation current, which was the result of reduced junction interface area between the CdS nanowires and the polycrystalline CdTe.

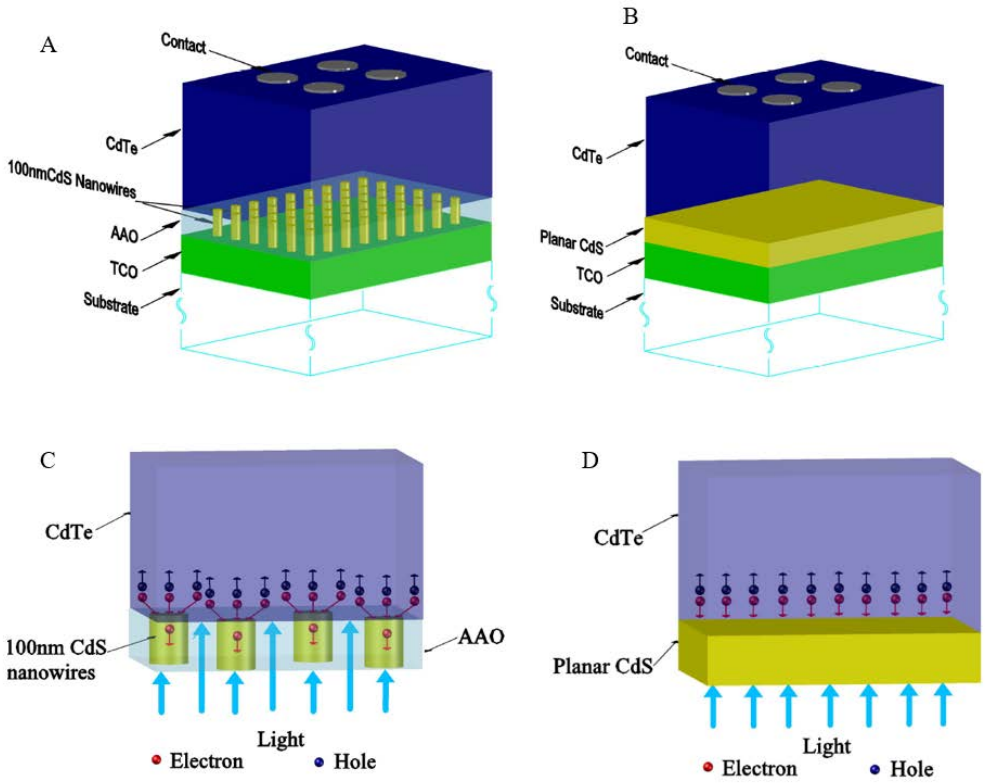

Figure 1.9 A. Schematic structure of a vertical stack nanowire CdS/CdTe solar cell, where light blue color represents absorption- negligible AAO, B. Schematic structure of a planar CdS/CdTe solar cell, C. Electron and hole transport through reduced junction interface area in a nanowire CdS/CdTe solar cell, D. Electron and hole transport through junction interface in a conventional planar CdS/CdTe solar cell [10]

1.3.2. Experimental Procedure

1.3.2.1 Fabrication of AAO Membrane

The AAO membrane was fabricated on commercially available ITO/ soda-lime glass substrates of cross section 1 inch x 1 inch. ITO/ soda-lime glass substrates sheet resistance of 23-28 Ω/square. The substrate was cleaned in acetone, methanol, de-ionized water for 30 minutes each and dried in nitrogen flow. After cleaning, 100 nm thick tin oxide (intrinsic SnO_2) layer and a 5 nm thick titanium (Ti) layer were sputtered on ITO by magnetic sputtering. 100nm thick aluminum (Al) layer is deposited on the top of Ti layer by electron beam evaporation.

The Al film was anodized in a 0.3 M oxalic acid solution at 50 V bias until Al was completely anodized. The temperature of the electrolyte was maintained at approximately 5 °C. Ti layer improves adhesion and passivation. The as-anodized samples were etched in 5% phosphoric acid (H_3PO_4) for 40 minutes to partially remove the barrier layer. Reactive ion etch (RIE) was used to completely remove the barrier layer. The RIE process was set as an anisotropic etching with 90W of RF and 250W of ICP power. After RIE process, the samples were etched in 5% phosphoric acid solution for 5 minutes to dissolve removed barrier layer particles. Figure 1.10 (A) and (B) show Al layer on ITO and AAO membrane. [10]

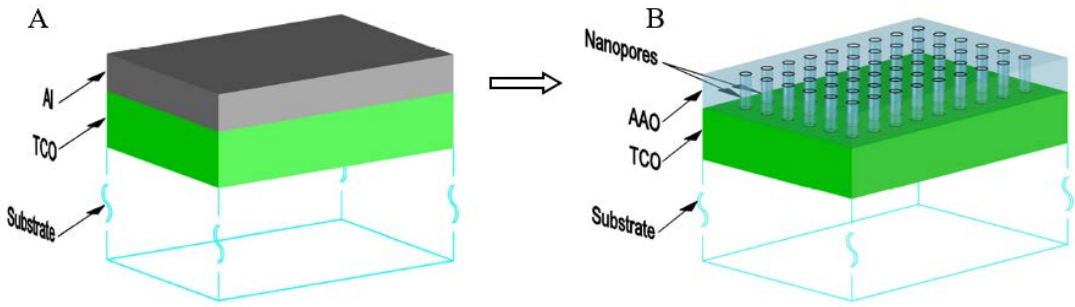

Figure 1.10 Schematics of (A) Al layer on ITO and (B) formed AAO membrane [10]

1.3.2.2 Fabrication of CdS Nanowire

The electrodeposition method was used for the growth of CdS nanowires. Figure 1.11shows the schematics illustration of CdS nanowires embedded into nanopores of AAO membrane [10]. The CdS nanowires were deposited in mixture of 0.5g cadmium chloride ($CdCl_2$) and 0.5g elemental sulfur in 50mL dimethyl-sulfoxide (DMSO) solution under a high dc current density of 7mA/cm^2 and at a high deposition temperature of 160°C to form nanowires. Then the CdS nanowires were soaked in a 75%-saturated $CdCl_2$ for 15 minutes, and are annealed at 400°C for 30 minutes with 100-sccm Argon purge.

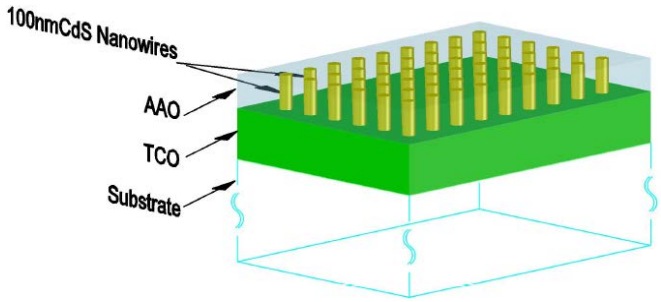

Figure 1.11 Schematics illustration of CdS nanowires embedded into nanopores of AAO membrane [10]

1.3.2.3 Fabrication of CdTe absorber layer

The two step closed-space sublimation process was used for depositing CdTe absorber layer. In first step, the CdTe source plate was fabricated. CdTe was sublimated from a graphite boat packed with a chunk of CdTe powder (99.99% Alfa Aesar) on Mo substrate, for source plate fabrication at 15-torr He, with a sample temperature of 625°C, Mo substrate temperature of 525°C, 2 mm spacing, and a deposition time of 20 min. [10]. In the second step, this substrate was considered as the source and the sample (nw-CdS/ i-SnO_2/ ITO/ glass) as the substrate. The source-substrate distance was kept at 2 mm. The chamber was pumped down to a background pressure of approximately 0.35 torr; then 5% O_2 was introduced at a total pressure of 15 torr. The source and substrate were ramped together to 570°C, and then the source temperature was quickly increased to 630°C.The source and substrate were maintained at 570°C, and 630°C for 2.3 min deposition. [10].

When the substrate was cooled down to 400°C in the CSS chamber, films were annealed in-situ for 10 minutes. In-situ annealing helps removing stress and shunts CdTe recrystallization. Next, they were soaked in a 75%-saturated $CdCl_2$ in methanol solution for 30 min at room temperature. Then, the pieces were then placed on an aluminum plate in a tube furnace that was purged with Argon. The furnace was then set at 400°C and left on for 30 min with a flow of 100-sccm Argon. After cooling to a maximum of 50°C, the pieces were rinsed in DI water to remove any excess $CdCl_2$.

1.3.2.4 Back Contact Formation

After the deposition of CdTe layer, the cells were etched in a solution of nitric and phosphoric acid (NP) (1% HNO_3, 88% H_3PO_4, 35% DI-water) for 35 seconds. The cells were then masked and 5 nm thick copper layer was deposited onto the back contact area by sputtering. Graphite paste (with 1200-2400 Ω/ml) and silver paste electrodes were painted on to the back contact area. These samples were then heated at 150°C for 10 min to facilitate forming a Cu_2Te layer and for curing the graphite/silver paste electrode Figure 3.4 shows the schematic of the finished nanowire CdS-CdTe solar cell [10].

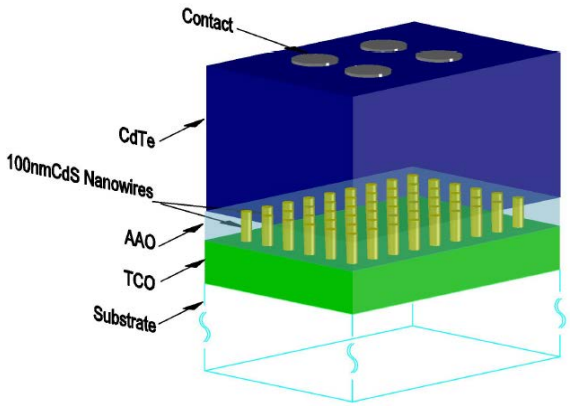

Figure 1.12 Schematic of the nanowire CdS-CdTe solar cells [10]

1.3.3 Results obtained from the experiment

SEM images of the CdS nanowires were obtained where it was observed that CdS nanowires take about 32% and AAO membranes take 68% of the physical area. Thus, the optical and electrical properties of CdS nanowires will be different from planar CdS window layer. It was observed that the AAO membranes have negligible absorption.

Thus, AAO membranes have the ability to transmit the incident light and the transmission of the incident light is better through CdS nanowires due to their larger effective energy band gap. Thus, more incident light reaches the absorber CdTe layer. [10]

The open-circuit voltage V_{oc} of 770 mV, a short current density J_{sc} of 26 mA/cm^2, a fill factor, FF of 60%, and power conversion efficiency (PCE) of 12% was obtained.

1.4. Motivation

We need to find the ways to improve the efficiency of solar cells, in order to provide green energy to the world. The nw-CdS/CdTe solar cell was invented in our lab which has the efficiency of 12%. This thesis is focused on the analysis of the parameters of this device.

The objective of this thesis is to understand the J-V characteristics of nw-CdS/CdTe solar cell and identify and evaluate the importance of various device parameters that affect the efficiency of nw-CdS/CdTe solar cell.

In order to achieve this, the simulations were performed using SCAPS-1D and the plots of J-V characteristics were obtained. The experimental and theoretical plots were compared and the results are presented and interpreted in this thesis.

2. Theory of SCAPS-1D

2.1 Numerical Modeling

Numerical Modeling has been increasingly used as a tool to understand the physical operation of the solar cells. Various measurements are done to understand the optical and electrical properties of the solar cell. However, it is difficult to analyze these measurements without the precise model. Therefore, numerical modeling is necessary to interpret the advanced measurement on complicated structures, design and optimization of advanced cell structures.

Following are the most important things to consider in a simulation software [11]: Capability of solving the basic equations –Poisson equation and the continuity equation for electron and holes

(1) Allow multiple semiconductor layers with available option of material grading
(2) Correct depiction of the discontinuities in the energy bands Ec and Ev at the interface
(3) Provide the convergence for most solar cell structures
(4) Capability of handling various tunneling mechanisms
(5) Fast and user friendly

There are several solar cell simulation programs available at present. Mark S. Lundstrom developed the first solar cell simulation program as a part of his PhD Thesis [12]. Other programs are Thin-Film Semiconductor Simulation Program (TFSSP) [13], Solar Cell Analysis Program in 1Dimension (SCAPlD), Solar Cell Analysis Program in 2 Dimension (SCAP2D) [14], PUPHS, and PUPHS2D [15]. These have been used to model a number of solar cells -thin-film Si: H, CdS/CIS, CdS/CdTe, Si, Ge, & GaAs cells in one spatial dimension and high efficiency Si and GaAs solar cells in two-dimensions.

The more common available simulation software programs are one dimensional programs, which include AMPS (Analysis of Microelectronic and Photonic Structures), ASA (Amorphous Semiconductor Analysis), PC1D and SCAPS. [11]

AMPS was written by S. Fonash and coworkers of Pennsylvania State University [16]. In this software, all parameters are independent of temperature. It is possible to simulate the graded junctions. When the definition of the device is completed, the user can simulate J -V in dark and light as well as spectral response measurements. However, AMPS is slow in solving the problem compared to other simulation programs.

ASA was written by M. Zeman, M. Kroon, J. van den Heuvel and others at the Delft University of Technology [17]. It is especially designed for amorphous silicon devices. The number of layers which can be used are very large compared to other programs. The user can simulate J-V, capacitance-voltage (C-V) characteristics in dark and light as well as spectral response measurements. It does not use graphical user interface for defining the problem. The problem is defined in ASCII input file. Therefore, it is difficult to start the problem from scratch.

PC1D was first written by Basore and coworkers at Sandia National Labs and further developed at UNSW, Australia [18]. It is very popular in PV community for modeling of crystalline Si solar cells. It has a clear user interface and defining a problem is easy. However, only five layers can be used in the defining the problem.

This thesis is focused on one-dimensional simulation and SCAPS-1D has been used as the tool for the simulations of nw-CdS/CdTe solar cell.

2.1.1 Introduction to SCAPS-1D

SCAPS-1D (a solar cell capacitance simulator in one dimension) is written and maintained at the University of Gent [19]. It is mainly used for modelling CdTe, CIS and CIGS based thin film solar cells. The SCAPS-1D is a Windows application program and has been written in C code.

We can add up to seven layers to the device and the physical and electrical parameters can be entered to each layer. Simple models are used for the temperature dependence of the effective density of states and the thermal velocity. Other parameters

such as the bandgap and the mobilities are independent of temperature. We can define up to three deep levels for each layer and three interface states can be placed in between these three layers. These deep levels can be energetically distributed in the forbidden zone (single level, uniform, gauss or exponential tail). The deep bulk levels can also vary spatially inside the layer (uniform, step, linear or exponentially). All other properties are spatially uniform for each layer. So, in order to introduce the graded junctions in the device, several layers must be used.

Recombination in deep bulk levels and their occupation has been described by the Shockley–Read–Hall (SRH) formalism. Recombination at the interface states is described by an extension of the SRH formalism, which allows the exchange of electrons between the interface state and the two adjacent conduction bands, and of holes between the state and the two adjacent valence bands.

Excitation parameters are displayed in a separate window, together with the parameters that are necessary for defining the measurements. SCAPS can simulate: J (V), C (V), C (f) and spectral response. Each measurement can be calculated for light or dark conditions and as a function of temperature. During the process of solving the simulations, the energy band diagram and the charge and currents in the device are shown on screen for each intermediate bias voltage or wavelength. These intermediate solutions can then be saved to a file. When the simulation is completed, the characteristics can be viewed and compared with characteristics from other simulations, which also can be saved to a file. This feature makes SCAPS a very interactive program.

2.2 Mathematical model of SCAPS-1D

2.2.1Basic Equations

SCAPS-1D solves the one dimensional semiconductor equations. The equations are as follows:

A. Current –density equations:

The current conduction mainly consists of two components, namely drift component, which is caused by the electric field and diffusion component, which is caused by the carrier-concentration gradient. These are also called as the constitutive equations. [5]

The equations are as follows:

$$J_n = q\mu_n n\mathcal{E} + qD_n \frac{dn}{dx} = q\mu_n \left(n\mathcal{E} + \frac{kT}{q}\frac{dn}{dx}\right) = \mu_n n \frac{dE_{Fn}}{dx} \quad (15)$$

$$J_p = q\mu_p p\mathcal{E} + qD_p \frac{dp}{dx} = q\mu_p \left(p\mathcal{E} + \frac{kT}{q}\frac{dp}{dx}\right) = \mu_p p \frac{dE_{Fp}}{dx} \quad (16)$$

where, $\mathcal{E}$- Electric field

μ_n , μ_p -Mobility of electron and hole respectively

J_n, J_p- Electron and hole current density respectively

D_n , D_p-Diffusion coefficient for electrons and holes respectively

E_{Fn}, E_{Fp}- Quasi-Fermi level for electron and hole respectively

B. Continuity equations:

In semiconductor, there are various carrier transport mechanisms. The continuity equations include the time-dependent phenomena such as generation, recombination and low-level injection. The effect of drift, diffusion, indirect or direct thermal generation or recombination give rise to the change in carrier concentration with respect to time. The net change of carrier concentration is the difference between generation and recombination, plus the net current flowing in and out of the specified region.

The continuity equations are given by:

$$-\frac{\partial J_n}{\partial x} - U_n + G = \frac{\partial n}{\partial t} \qquad (17)$$

$$-\frac{\partial J_p}{\partial x} - U_p + G = \frac{\partial p}{\partial t} \qquad (18)$$

where, G- Generation rate

U_n, U_p-Net recombination/generation rate

C. Poisson equation:

Poisson equation gives the starting point in obtaining the qualitative solution for electrostatic variables in a semiconductor. It is given by

$$\frac{\partial}{\partial x}\left(\varepsilon_0 \varepsilon \frac{\partial \Psi}{\partial x}\right) = -q(p - n + N_D - N_A) \qquad (19)$$

where, $q(p - n + N_D - N_A) = \rho$ (charge density), considering the dopants to be fully ionized.

N_D , N_A-Donor and acceptor impurity concentration respectively

Together with appropriate boundary conditions at the interfaces and contacts, this results in a system of coupled differential equations in (Ψ, n, p) or (Ψ, E_{Fn}, E_{Fp}).

The steady state and small signal solution of this system is numerically calculated by SCAPS-1D.

At first, the dc solution is calculated by the dc algorithm. Then the ac algorithm calculates the complex admittance from the dc solution.

2.2.2 DC Analysis

The dc analysis of the problem is explained in this section. The simulation domain is partitioned into number of subdomains. The differential equations are replaced by algebraic equations, in each subdomain. The unknown functions are potential and carrier concentrations. They are replaced by their values in the nodes. Then, these nonlinear algebraic equations are solved iteratively [20].

The classical three point discretization method is used in this analysis. By assuming the electric field is constant within each subdomain, the discrete Poisson equation is

obtained. The discretization of continuity equations are obtained by using exponentially fitted finite difference scheme.

For the dc solution of the problem, the normalized electrostatic potential qΨ /kT and the following functions of quasi-Fermi energies are used as a set of variables:

$$u = exp\left(\frac{E_{Fn}}{kT}\right) - exp\left(\frac{qV}{kT}\right) \qquad (20)$$

$$v = exp\left(\frac{E_{Fp}}{kT}\right) - 1 \qquad (21)$$

where, V is the applied bias and E_{Fn} and E_{Fp} are the quasi-Fermi energies of the electrons and holes respectively.

Here, the electrostatic potential is referenced to its value at the absorber contact and the quasi-Fermi energy are referenced to the equilibrium Fermi energy E_F. The discrete continuity equations are linear in u and v, if the recombination terms are ignored. All the coefficients are scaled to make them dimensionless and in order to obtain the better conditioned numerical values of coefficient matrices.

A nonlinear system of 3N equations with 3N variables is obtained with N nodes:

$$F_{\Psi}^{dc}\left(\vec{\Psi}, \vec{u}, \vec{v}\right) = 0 \quad (22)$$

$$F_{u}^{dc}\left(\vec{\Psi}, \vec{u}, \vec{v}\right) = 0 \quad (23)$$

$$F_{v}^{dc}\left(\vec{\Psi}, \vec{u}, \vec{v}\right) = 0 \quad (24)$$

where, F_{Ψ}^{dc} denotes the N- dimensional vector function with components, the discrete Poisson equation with N nodes and arguments, the variables $\left(\vec{\Psi_i}, \vec{u_i}, \vec{v_i}\right)$, with i=1,2…N.

The total system of 3N equations is separated into three subsystems of N equations with N variables. These subsystems are solved by Newton Raphson method.

The correction vector is solved in three steps. Poisson equation is solved for the electrostatic potential and values of u and v are taken from the previous step in order to

calculate the coefficients. Similarly, continuity equations are used for the calculation of u and v. Here, the first estimate of the potential for the calculation at applied bias (ΔV) is given by $\Psi_i - (x_i/L)\Delta V$, where i=1, 2,…N and L is the device length, x_i is the distance from the node I to the back contact and Ψ_i is the equilibrium potential.

2.2.3 AC Analysis

The time dependent semiconductor equations are discretized and considering the variables (Ψ, n, p), the equations are given by: [20]

$$F_{\Psi i}\left(\overrightarrow{\Psi}, \vec{n}, \vec{p}\right) = 0 \qquad (25)$$

$$F_{\mathrm{n}i}\left(\overrightarrow{\Psi}, \vec{n}, \vec{p}\right) = -\frac{\partial n_i}{\partial t} \qquad (26)$$

$$F_{\mathrm{p}i}\left(\overrightarrow{\Psi}, \vec{n}, \vec{p}\right) = -\frac{\partial p_i}{\partial t} \qquad (27)$$

The equation in the frequency domain is obtained by linearizing equations (25), (26) and (27) around the dc solution. The derivatives with respect to time are replaced by jω where ω is the angular frequency of the ac-excitation. With the dc solution,
$F_{\mathrm{n}i}\left(\overrightarrow{\Psi_0}, \overrightarrow{n_0}, \overrightarrow{p_0}\right) = 0$

The first order Taylor expansion of the discrete continuity equations for electrons at node i is given by:

$$\sum_{k=1}^{N} \frac{\partial F_{ni}}{\partial \Psi_k}\tilde{\Psi}k + \frac{\partial F_{ni}}{\partial \mathrm{n}_k}\tilde{\mathrm{n}}k + \frac{\partial F_{ni}}{\partial \mathrm{p}_k}\tilde{\mathrm{p}}k = -j\omega\tilde{\mathrm{n}}_i \qquad (28)$$

where, $(\widetilde{\Psi_\iota}, \widetilde{n_\iota}, \widetilde{p_\iota})$ are the small signal amplitudes of the potential, carrier concentrations at node i. After linearization of the Poisson equation and continuity equations, linear system of 3N equations with 3N variables are obtained. As the system is linear, the solution is found by finding the lower-upper decomposition of N x N matrix with 3x3 matrices as elements.

For node i, 3x3 matrix A_{ik} is given by:

$$A_{i,k} = \begin{pmatrix} \frac{\partial F_{\Psi i}}{\partial \Psi_k} & \frac{\partial F_{\Psi i}}{\partial \mathrm{n}_k} & \frac{\partial F_{\Psi i}}{\partial \mathrm{p}_k} \\ \frac{\partial F_{\mathrm{n}i}}{\partial \Psi_k} & \frac{\partial F_{\mathrm{n}i}}{\partial \mathrm{n}_k} + j\omega\delta_{ik} & \frac{\partial F_{\mathrm{n}i}}{\partial \mathrm{p}_k} \\ \frac{\partial F_{pi}}{\partial \Psi_k} & \frac{\partial F_{pi}}{\partial \mathrm{n}_k} & \frac{\partial F_{pi}}{\partial \mathrm{p}_k} + j\omega\delta_{ik} \end{pmatrix} \qquad (29)$$

$$\widetilde{w_i} = \begin{pmatrix} \widetilde{\Psi_i} \\ \widetilde{n_i} \\ \widetilde{p_i} \end{pmatrix} \quad (30)$$

$$\widetilde{z_N} = \begin{pmatrix} -\tilde{V} \\ 0 \\ 0 \end{pmatrix} \quad (31)$$

$\widetilde{z_i}$=0 for i<N and $\tilde{V}$ is the small signal amplitude of the applied bias. The ac system thus becomes:

$$A\tilde{w} = \tilde{z} \quad (32)$$

In order to avoid the numerical problem, equation (32) is scaled using the S (n x n) scaling matrix. The elements of scaling matrix is given by:

$$S_{i,k} = \delta_{ik} A_{i,i}^{-1} \quad (33)$$

The small signal amplitude $\tilde{J}$ is calculated after obtaining the solution for potential and carrier concentrations. Thus, the capacitance and conductance can be calculated by using the following equation:

$$G(\omega) = Re\left(\frac{\tilde{J}}{\nabla}\right) \quad (34)$$

$$C(\omega) = \frac{1}{\omega} Im\left(\frac{\tilde{J}}{\nabla}\right) \quad (35)$$

2.2.4 Physical Model

For interface recombination, SCAPS-1D uses Pauwells Vanhoutte model [20]. The model considers four bands for interface states i.e. conduction and valence bands of both semiconductors at the interface.

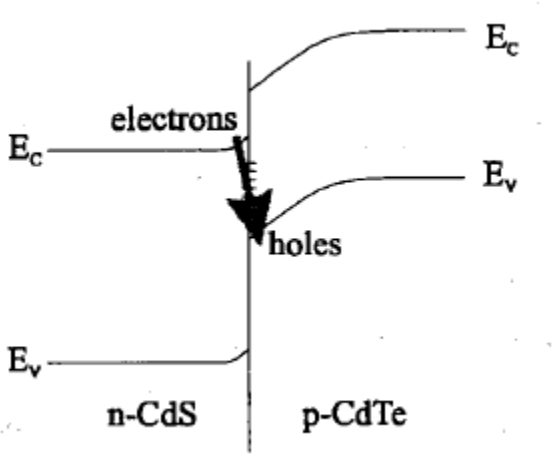

Figure 2.1 Pauwells Vanhoutte Model for CdS/CdTe heterojunction [20]

This theory considers the recombination of electrons of one semiconductor with holes of another semiconductor along with the standard recombination of electrons with holes within the same semiconductor. Here, the most important recombination path is the recombination of window electrons with the absorber holes. The total charge in the interface states equals the discontinuity in the dielectric displacement at the interface.

It is assumed in SCAPS-1D that the quasi fermi levels of electrons and holes are discontinuous at the interface when the current flows through the interface. It is taken care by including one extra node at the interface in the numerical algorithm. The electrostatic potential is assumed continuous at the interfaces.

Thermionic emission theory has been used to explain the transport of free carriers across the interface. Thermionic emission current for electrons for two direct bandgap semiconductors with identical effective masses, is given by

$$j_{th\,n} = v_{th\,n}(n^{(1)} exp\left(-\frac{|\Delta E_c|}{kT}\right) - n^{(2)}) \qquad (36)$$

Where, $j_{th\,n}$=particle current from semiconductor 1 to 2
$v_{th\,n}$ = thermal velocity of electrons
$n^{(1)}$, $n^{(2)}$= electron concentrations
ΔE_c= conduction band discontinuity

Similarly, thermionic emission current for holes can be calculated.

At the metal semiconductor contact, the boundary equations are imposed on the continuity equation for the electrons:

$$j_n = S_n(n - n_{eq}) \qquad (37)$$

where, n_{eq} is the number electrons at the contact in equilibrium. If the electrons are the majority carriers at the contact, then

$$S_n = \frac{A^* T^2}{qN_c} = v_{th\,n} \qquad (38)$$

where, A^* is the effective Richardson constant.

When the electrons are minority carriers at the contact, then S_n in equation (37) is the surface recombination velocity of electrons.

3. Simulation Procedures

SCAPS-1D was used for doing the simulating the J-V characteristics of nanowire CdS-CdTe solar cell. The main screen which pops up after running the SCAPS-1D is as shown in figure 3.1.

In the working point panel, the temperature (K), voltage (V), frequency (Hz) and number of operations are entered. Series resistance, shunt resistance, Illumination (dark/ light) are entered in the startup panel.

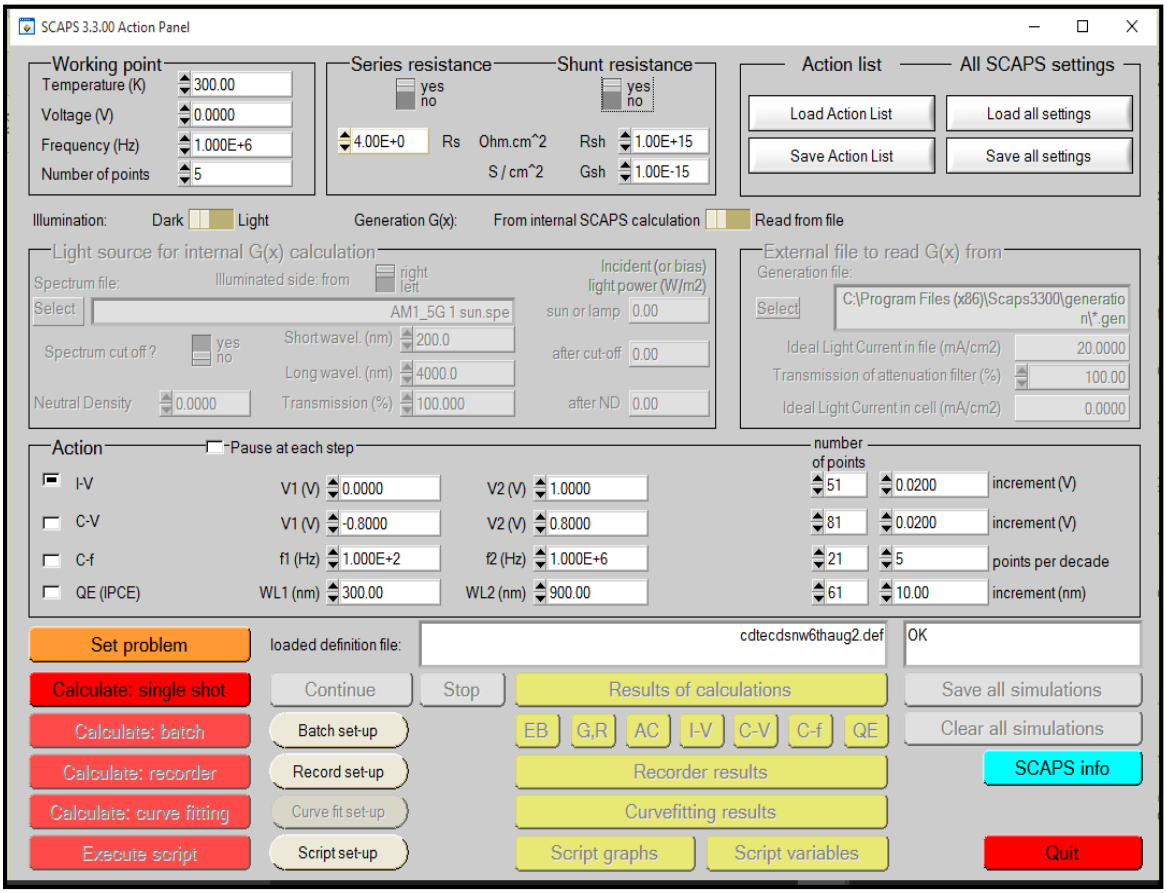

Figure 3.1 The SCAPS start up panel

In SCAPS-1D, the problem is defined by specifying the key inputs such as the geometry and the material properties of the layers and contacts. The parameters of all the layers in nw-CdS/CdTe device were entered in the SCAPS-1D, including the front and back contact.

The thickness of the layers was entered as per the experimental data. The material properties of the layers and contacts were selected from literature [21]-[24] and in some cases such as interface state density, defect density, surface recombination velocity, bulk resistance, effective state densities and metal work function, were estimated and adjusted in order to get the curve fit to the experimental I-V curve at 300K. The range of the parameters used for the simulations are discussed in section 4.1. It is worthwhile to mention here that the parameters were kept same for all the temperatures.

It is to be noted here that SCAPS-1D only takes the thin layer parameters, the nanowire-CdS layer was presented as the thin layer with the higher absorption constant (9.6x10^5). As mentioned in section 1.3.3, nanowire-CdS layer has proven to be more improving light transmission through the window layer and enhancing absorption and carrier generation in absorber. [25]

The problem is defined by clicking the SET PROBLEM in the startup panel. Figure 3.2 shows the SCAPS solar cell definition panel.

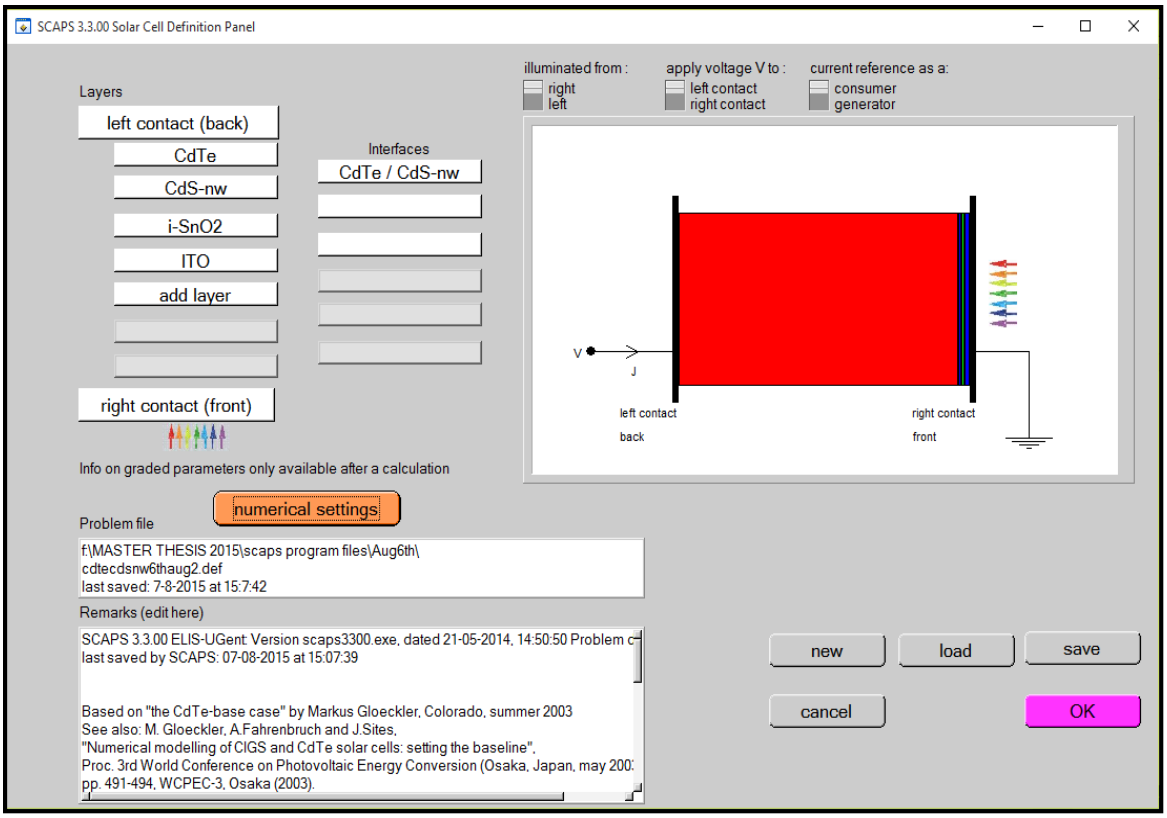

Figure 3.2 The SCAPS solar cell definition panel

In each layer, specific parameters are to be entered as shown in the figure 3.3 and figure 3.4. The whole screen is shown in two parts here. Between any two layers, interface layer can be defined.

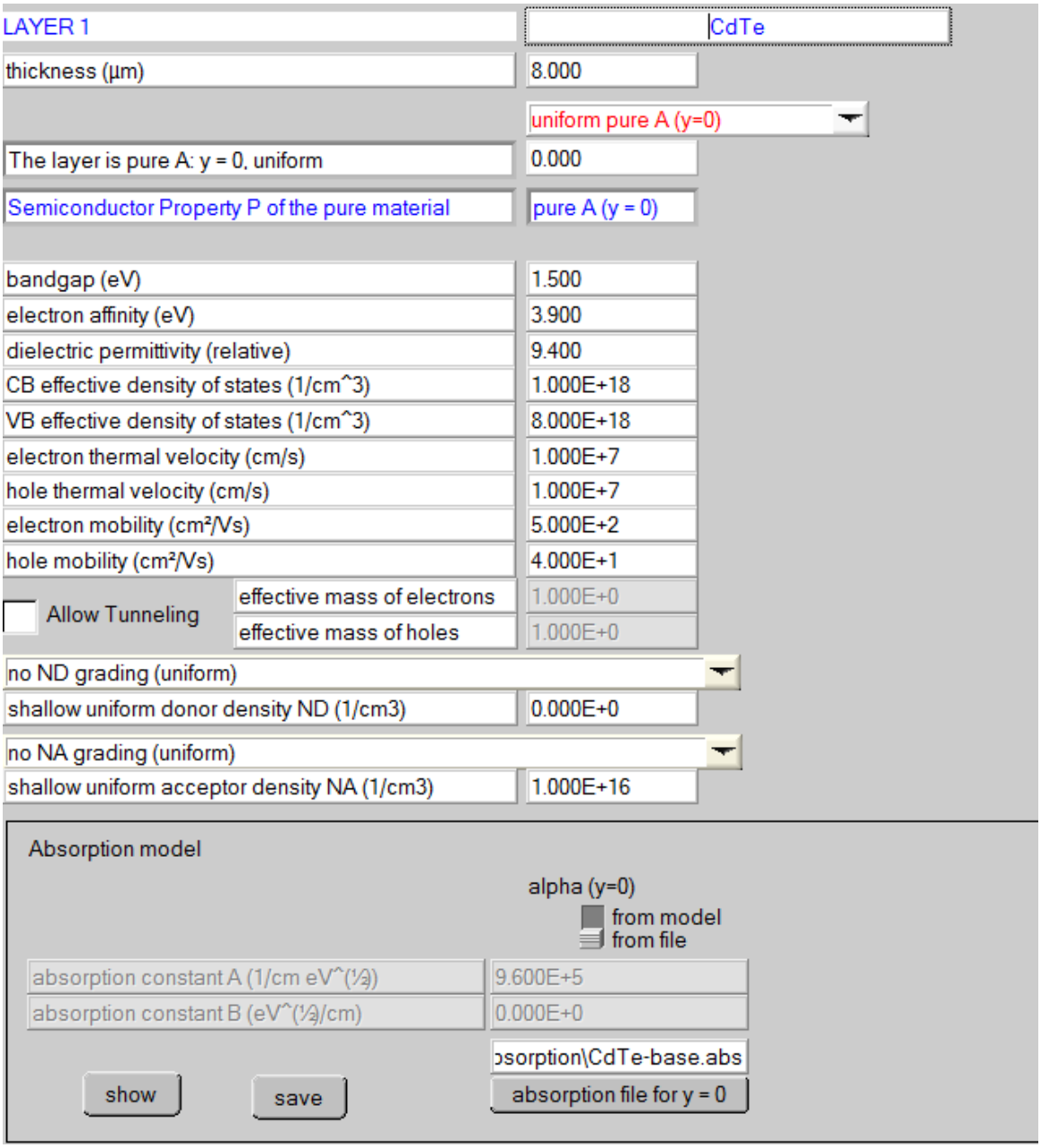

Figure 3.3 Parameters for each layer in SCAPS

The optical absorption constant α can be set either from the model or from a file. When it is set from a model, as it is wavelength dependent, is calculated using following equation in the program.

$$\alpha(\lambda) = \left(A + {}^{B}/_{h\upsilon}\right)\sqrt{h\upsilon - E_g} \qquad (39)$$

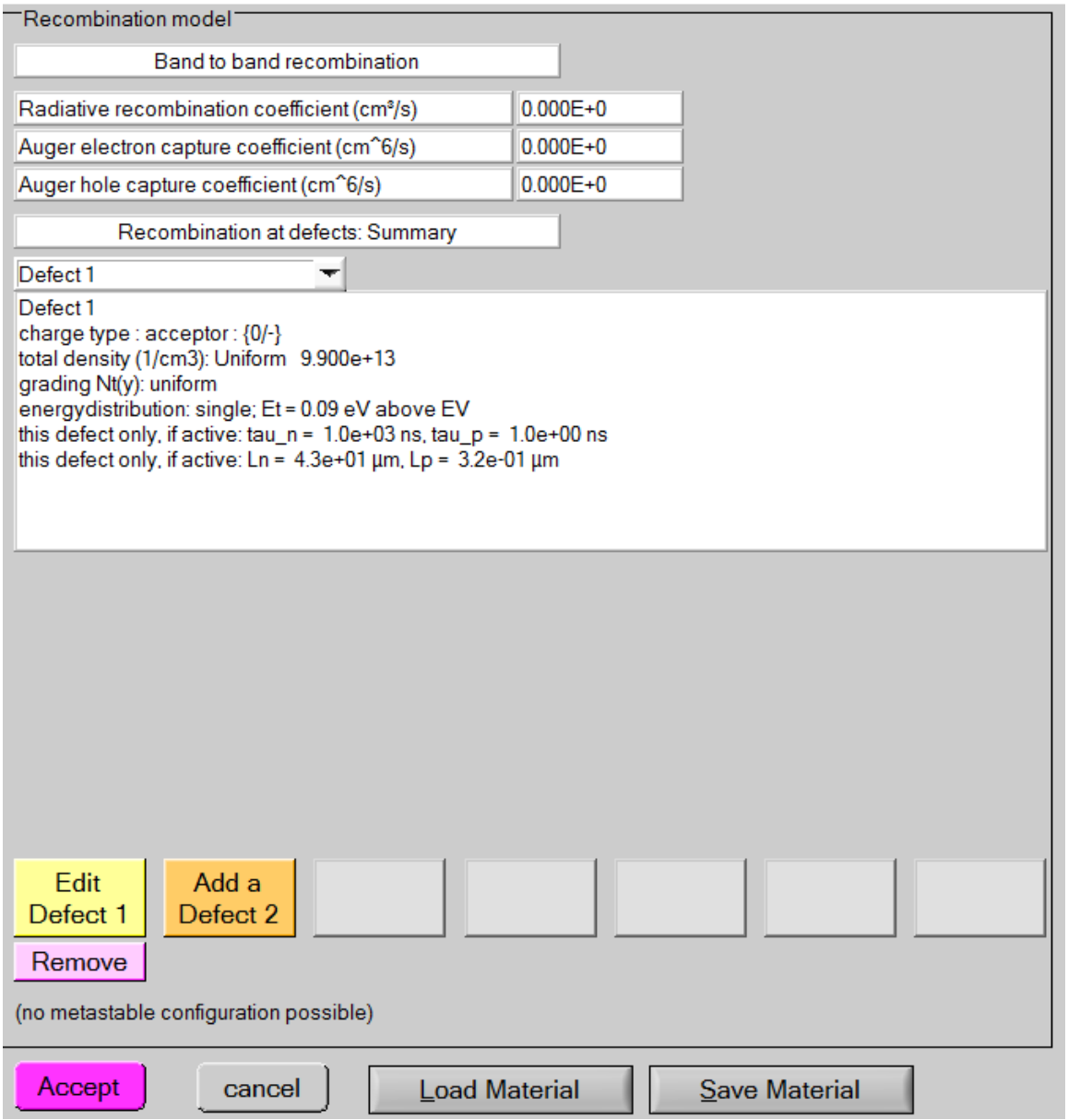

Figure 3.4 Parameters including defect type for each layer in SCAPS

The defects can be added by clicking on “add a defect” button. The new window appears on the screen as shown in figure 3.5. The program allows to set up to seven defects for each layer.

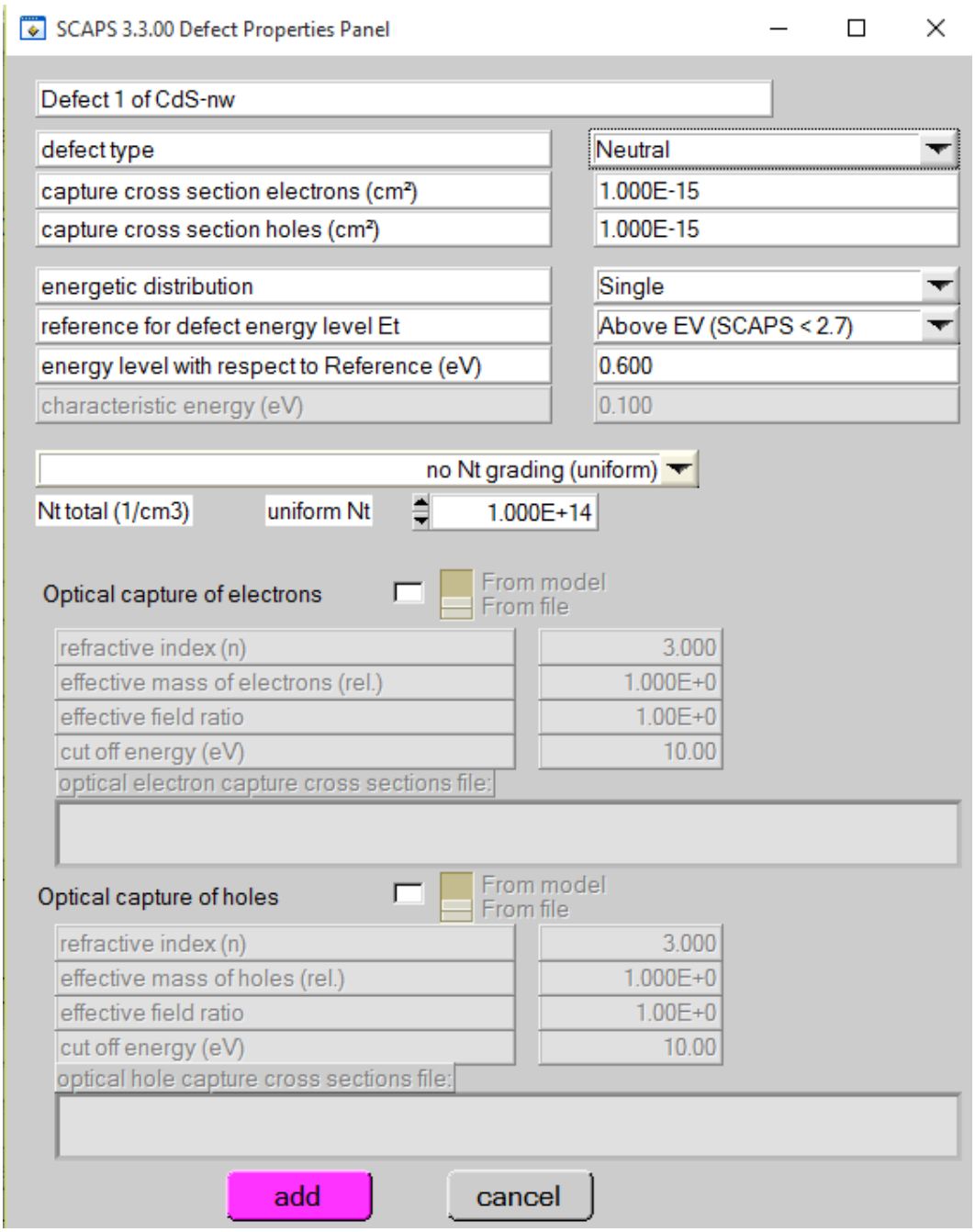

Figure 3.5 Defect properties panel

The contact properties can be entered by either clicking on front or back contact button on the cell definition panel, which opens the contact properties panel as shown in figure 3.6.

The metal work function (φ_m) needs to be entered here. The program calculates metal work function at various temperature if flat band option is used. It calculates the barrier height relative to fermi level and conduction /valence band and displays on the screen. [26]

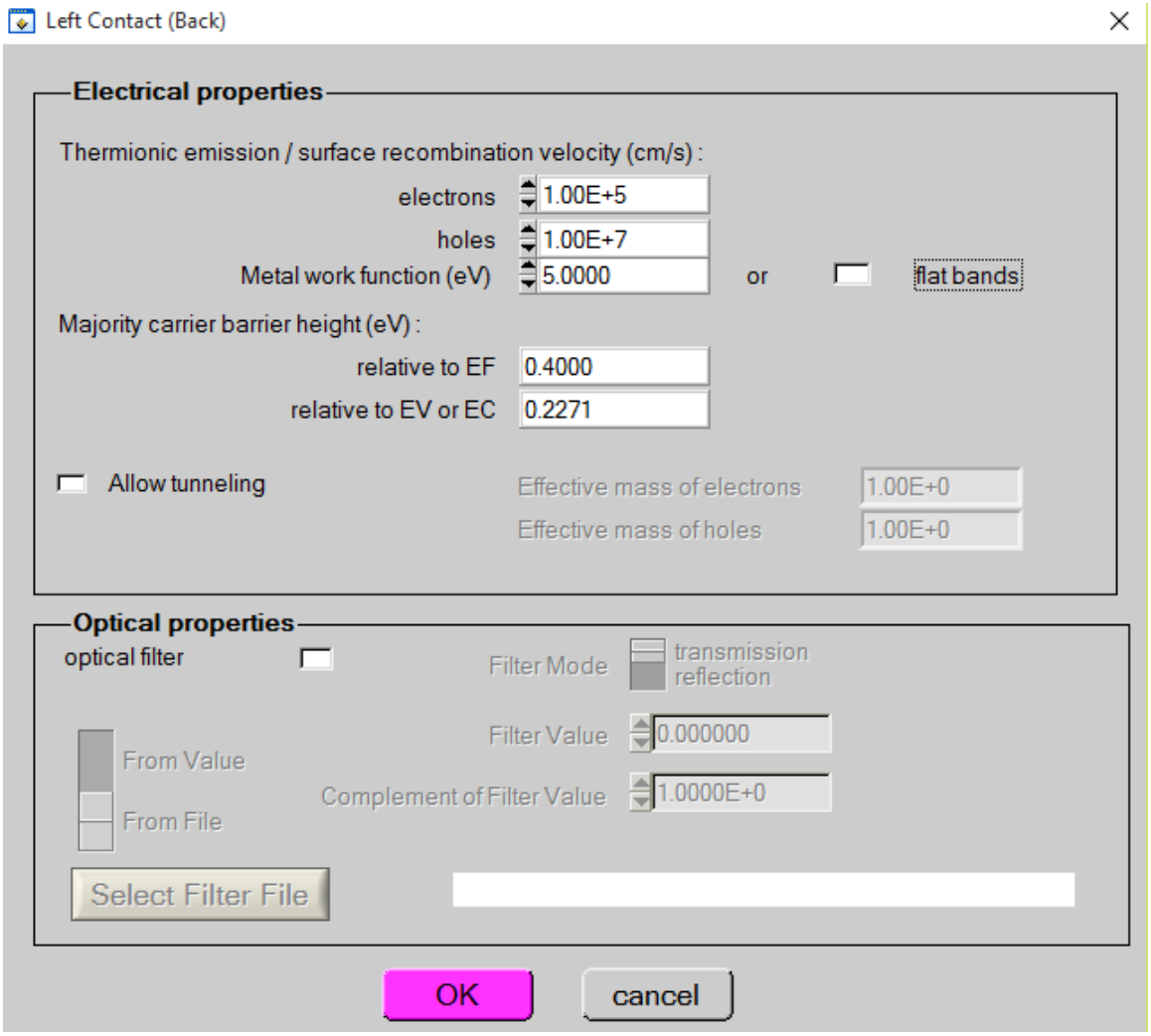

Figure 3.6 Contact properties panel

The density of states in conduction band (N_c) and valence band (N_v), thermal velocity (v_{th}) and diffusion co-efficient are temperature dependent. In SCAPS-1D, all the parameters are defined at T_0 (default temperature-300K). N_c, N_v and v_{th} are calculated as follows for various temperatures. [26]

$$Nc(T) = Nc(T_0)\left(\frac{T}{T_0}\right)^{1.5} \qquad (40)$$

$$Nv(T) = Nv(T_0)\left(\frac{T}{T_0}\right)^{1.5} \quad (41)$$

$$v_{th}(T) = v_{th}(T_0)\left(\frac{T}{T_0}\right)^{0.5} \quad (42)$$

The other parameters are considered temperature independent.

SCAPS-1D allows the user to set tunneling in each layer for band to band tunneling, intra-band tunneling, tunneling to interface states and tunneling to contacts.

The table 3.1 shows the parameters used in the SCAPS-1D simulations at various temperatures.

Table 3.1 Parameters used for simulations in SCAPS-1D

Parameters	Value
CdS-nw/CdTe interface	
defect type	acceptor
capture cross section electrons (cm^2)	1.00E-13
capture cross section holes (cm^2)	1.00E-13
energetic distribution	single
reference for defect energy level Et	Above Ev of CdTe
Parameters	
energy with respect to Reference (eV)	0.100
total density (integrated over all energies) ($1/cm^2$) at CdS/CdTe interface	1.60E+12
CdTe	
thickness (µm)	8
bandgap (eV)	1.5
electron affinity (eV)	3.9
dielectric permittivity (relative)	9.4
CB effective density of states ($1/cm^3$)	1.000E+18

Parameters	Value
VB effective density of states (1/cm^3)	8.000E+18
electron thermal velocity (cm/s)	1.000E+7
hole thermal velocity (cm/s)	1.000E+7
electron mobility (cm²/Vs)	5.000E+2
hole mobility (cm²/Vs)	4.000E+1
shallow uniform acceptor density NA (1/cm^3)	1.000E+16
absorption constant A (1/cm eV$^{(½)}$)	9.600E+5
Defect 1 of CdTe	
defect type	Single Acceptor
capture cross section electrons (cm²)	1.000E-15
capture cross section holes (cm²)	1.000E-12
energetic distribution	Single
reference for defect energy level Et	Above Ev
energy level with respect to Reference (eV)	0.090
Nt total (1/cm^3) uniform	9.900E+13
CdS-nw	
thickness (µm)	0.090
bandgap (eV)	3.490
electron affinity (eV)	4.000
dielectric permittivity (relative)	9.000
CB effective density of states (1/cm^3)	8.000E+19
VB effective density of states (1/cm^3)	8.000E+18
electron thermal velocity (cm/s)	1.000E+7
hole thermal velocity (cm/s)	1.000E+7
electron mobility (cm²/Vs)	1.000E+2
hole mobility (cm²/Vs)	2.500E+1
shallow uniform donor density ND (1/cm^3)	1.150E+17

Parameters	Value
absorption constant A (1/cm $eV^{(½)}$)	9.600E+5
Allow Tunneling	Yes
effective mass of electrons	1.900E+1
effective mass of holes	8.000E+1
i-SnO2	
thickness (µm)	0.100
bandgap (eV)	3.600
Parameters	Value
electron affinity (eV)	4.400
dielectric permittivity (relative)	9.000
CB effective density of states ($1/cm^3$)	2.200E+19
VB effective density of states ($1/cm^3$)	1.800E+19
electron thermal velocity (cm/s)	1.000E+7
hole thermal velocity (cm/s)	1.000E+7
electron mobility (cm^2/Vs)	1.000E+2
hole mobility (cm^2/Vs)	2.500E+1
shallow uniform acceptor density NA ($1/cm^3$)	1.000E+15
shallow uniform donor density ND ($1/cm^3$)	1.000E+15
absorption constant A (1/cm $eV^{(½)}$)	1.000E+5
ITO	
thickness (µm)	0.150
bandgap (eV)	3.650
electron affinity (eV)	4.800
dielectric permittivity (relative)	8.900
CB effective density of states ($1/cm^3$)	5.200E+18
VB effective density of states ($1/cm^3$)	1.000E+18
electron thermal velocity (cm/s)	2.000E+7
hole thermal velocity (cm/s)	1.000E+7

Parameters	Value
electron mobility (cm^2/Vs)	1.000E+1
hole mobility (cm^2/Vs)	1.000E+1
shallow uniform donor density ND ($1/cm^3$)	1.000E+15
absorption constant A ($1/cm\ eV^{(½)}$)	1.000E+5
BACK CONTACT (CdTe)	
Thermionic Emission/ surface recombination velocity (cm/s)	
(a) electrons	1.000E+5
(b) holes	1.000E+7
Metal work function (eV)	5
Majority Carrier barrier height(eV)	
(a) relative to Ef	0.4
(b) relative to Ev	0.2271
FRONT CONTACT	
Thermionic Emission/ surface recombination velocity (cm/s)	
(c) electrons	1.000E+5
(d) holes	1.000E+7
Metal work function (eV)	5.0216
Majority Carrier barrier height(eV)	
(a) relative to Ef	0.2216
(b) relative to Ec	0

I-V measurements are done by clicking on the checkbox in startup panel and selecting dark/ light condition. The range of voltage can be set in the panel. Then either the “Calculate: single shot” or “Calculate: Batch” can be used to get the measurements. When we click on the “Calculate: Batch”, the panel opens where we can choose which parameter to vary, over which range, and in which mode (Lin, Log or custom). We can also define more than one parameter, and vary all of them (in a nested way or ‘simultaneous’).

SCAPS uses a start point (initial guess) in order to get the solution under specified working point conditions and at the first measurement point. Every calculation starts at a start point. Here, it is assumed that the quasi fermi levels are zero throughout the structure and there is no potential drop. This is used as an initial guess to get equilibrium where there is no illumination and voltage is zero. So, when the calculations are done in dark condition, this is considered as an initial guess to calculate the solution in working point conditions.

In light condition, the intermediate step is used in order to calculate the short circuit situation. The intermediate steps between the start point and the working point have to be close in order to get convergence. The number of intermediate steps can be entered in the action panel. When the working point situation is calculated, the program calculate the first calculation point. In I-V measurement, the working point is usually considers as 0 V and then the first calculation is done from the start point of the voltage range setup in the main panel.

When we click on the “Calculate” button, the energy bands panel opens and the calculations start. SCAPS shows the movie how the conduction band, valence band and fermi levels are evolving. Once it is completed, energy band and current densities are shown. I-V curves can be seen after clicking on the “I-V” buttons. Figure 3.7 shows the I-V curve at 300K (dark).

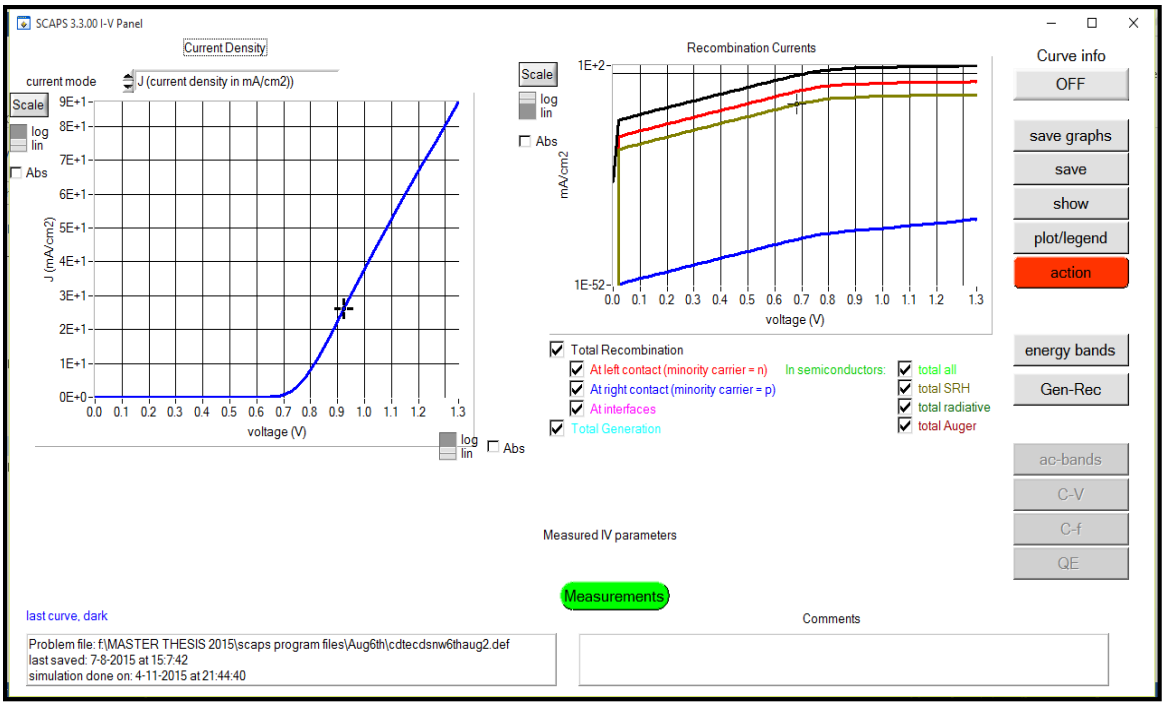

Figure 3.7 SCAPS I-V panel

The parameters such as the CdTe defect, CdS/ CdTe interface layer defect, etc. were adjusted in order to get the fit for the experimental I-V characteristics at various temperatures. The feature “Calculate: Batch” was used to perform number of simulations at the same time.

I-V measurements were obtained at dark and light for the temperatures 296K, 275K, 250 K and 225 K. The results were compared with the experimentally obtained data.

4. Results and Discussion

4.1. Effect of various parameters on light I-V characteristics

Effect of various parameters such as interface state density, CdS and CdTe state densities, trap concentration, metal work function on light I-V curves were studied by using SCAPS-1D and are presented in this section.

4.1.1. Effect of interface state density

The charge Q_{it} in the interface traps exists within the forbidden gap due to the interruption of the periodic lattice structure at the surface of a crystal. [5] Q_{it} can be very high because the density of ions at the interface can be quite high, in the order of 10^{15} ionscm^{2}. Similar to bulk impurities, an interface trap is considered as a donor when neutral (filled with electrons) and can become positively charged by donating an electron. An interface trap is considered as an acceptor when neutral (empty) and can become negatively charged by accepting an electron.

To study the effect of interface state density on I-V characteristics, the interface state densities (N_{it}) between nw-CdS and CdTe layers were varied in the simulations from the range of 5.88×10^{11} to 6.35×10^{14} cm^{-2}. This range related to the simulated J-V curves obtained by SCAPS-1D with no convergence failure. In this model, the defect type for the interface state is considered as an acceptor with single level energetic distribution. Figs. 4.1-4.15 show the simulated J-V characteristics of solar cell for the range of interface state densities.

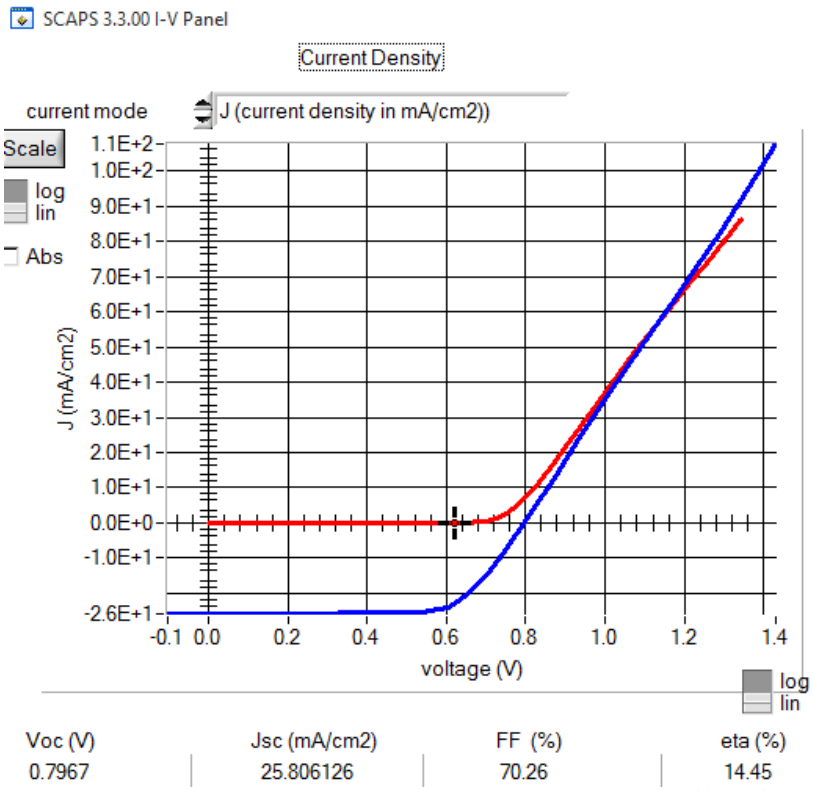

Figure 4.1 Simulated J-V characteristics at 300 K for Nit: 5.88 x$10^{11}$$cm^{-2}$

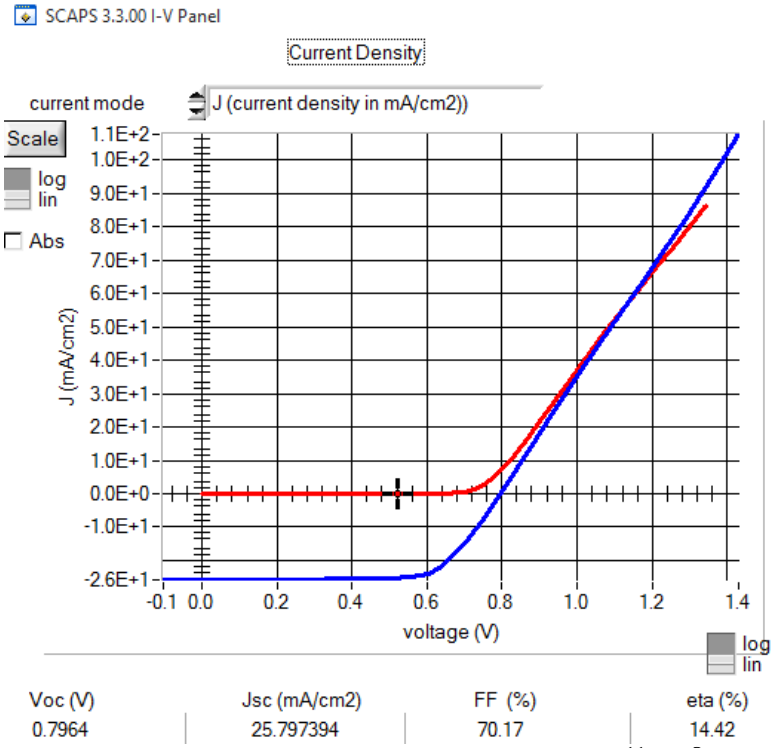

Figure 4.2 Simulated J-V characteristics at 300 K for N_{it}: 6 x$10^{11}$$cm^{-2}$

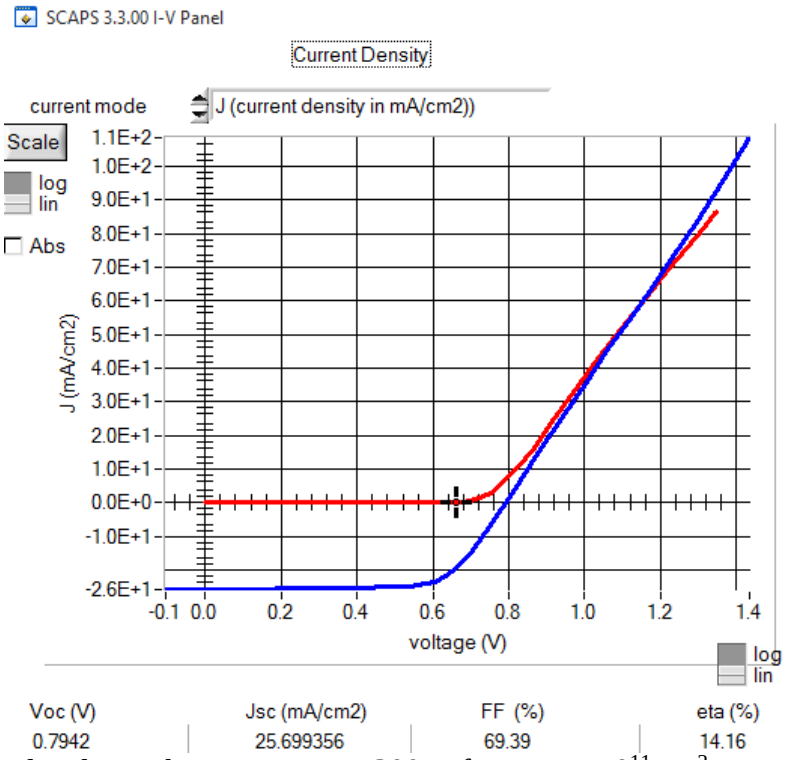

Figure 4.3 Simulated J-V characteristics at 300 K for N_{it}: 7 x$10^{11}$$cm^{-2}$

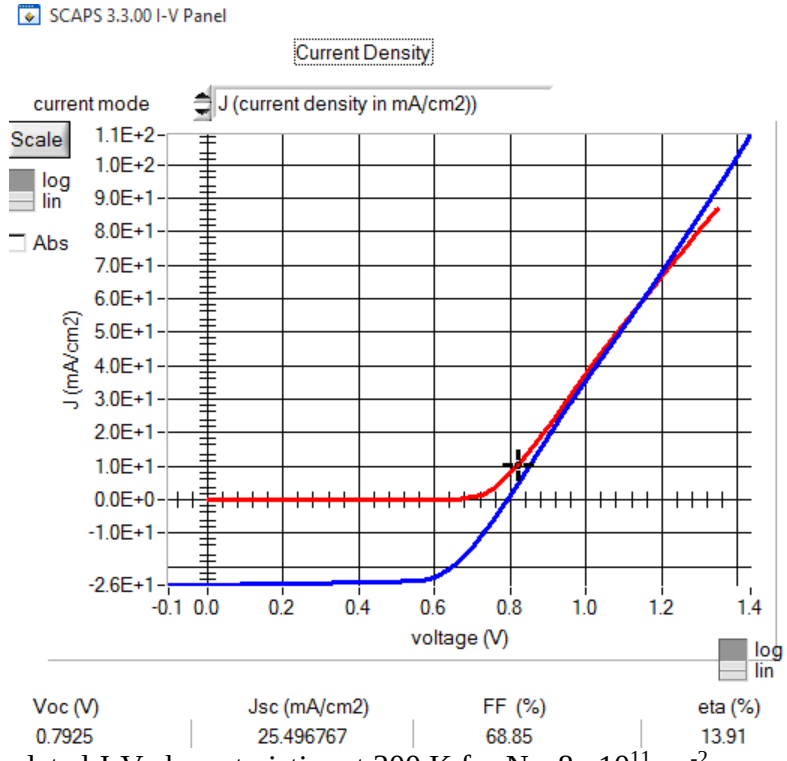

Figure 4.4 Simulated J-V characteristics at 300 K for N_{it}: 8 x$10^{11}$$cm^{-2}$

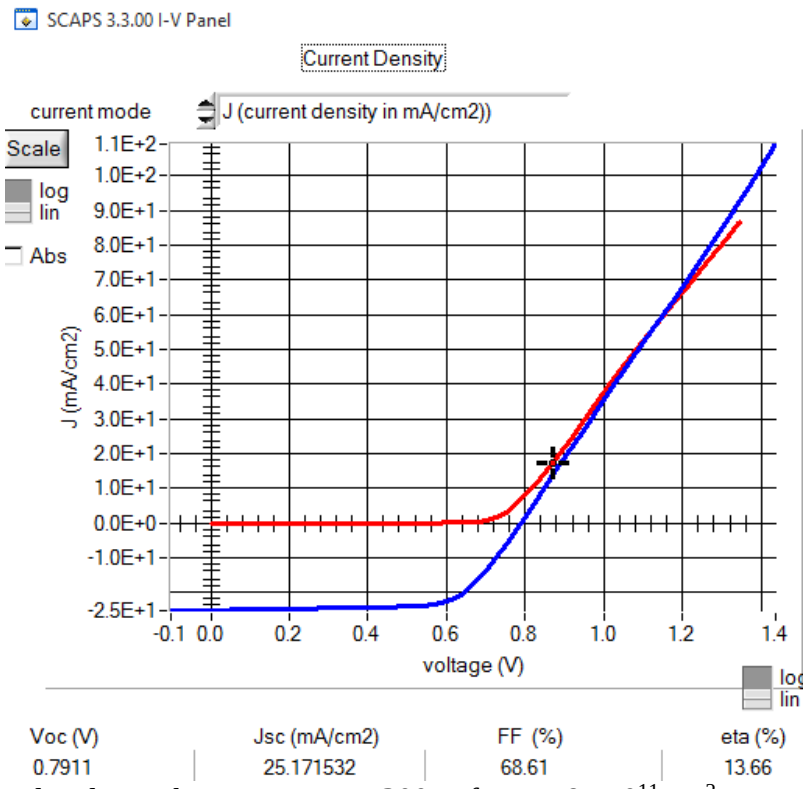

Figure 4.5 Simulated J-V characteristics at 300 K for N_{it}: 9 x10^{11}cm^{-2}

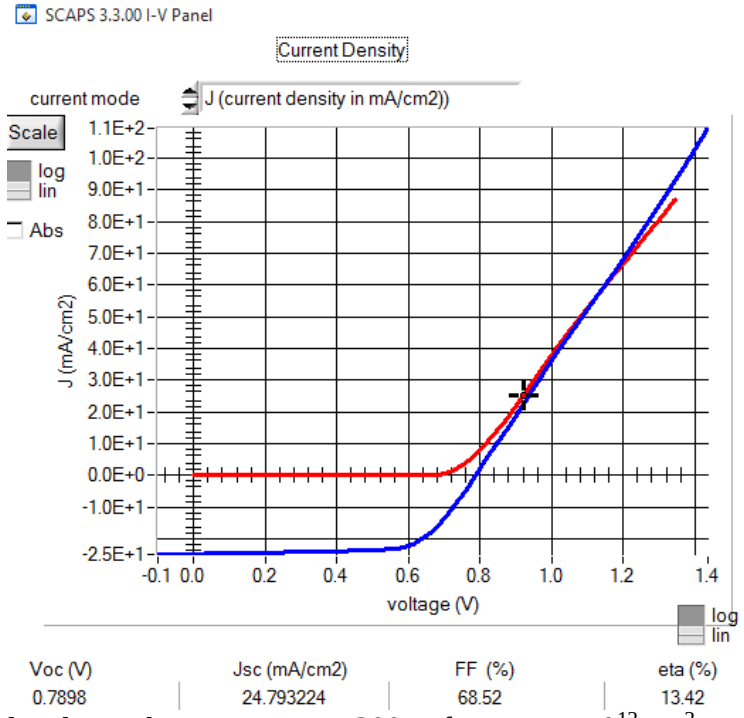

Figure 4.6 Simulated J-V characteristics at 300 K for Nit: 1 x10^{12}cm^{-2}

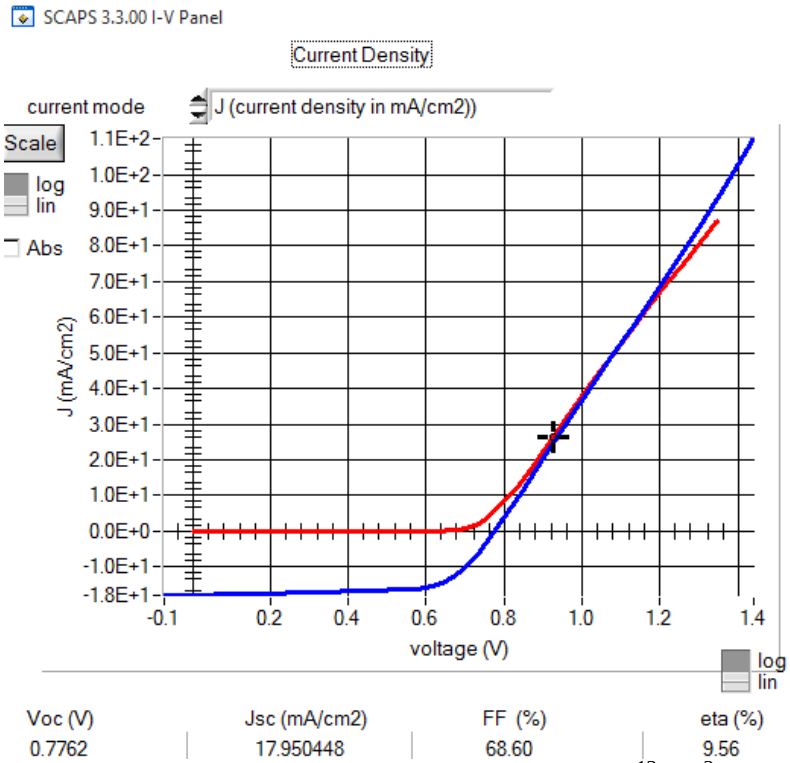

Figure 4.7 Simulated J-V characteristics at 300 K for Nit: 3 x$10^{12}$$cm^{-2}$

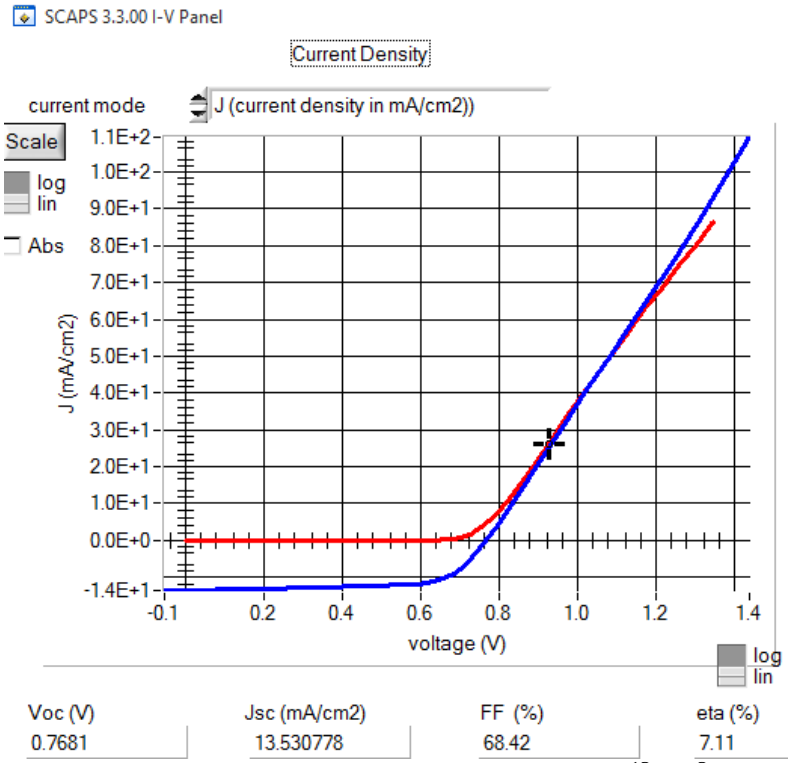

Figure 4.8 Simulated J-V characteristics at 300 K for N_{it}: 5 x$10^{12}$$cm^{-2}$

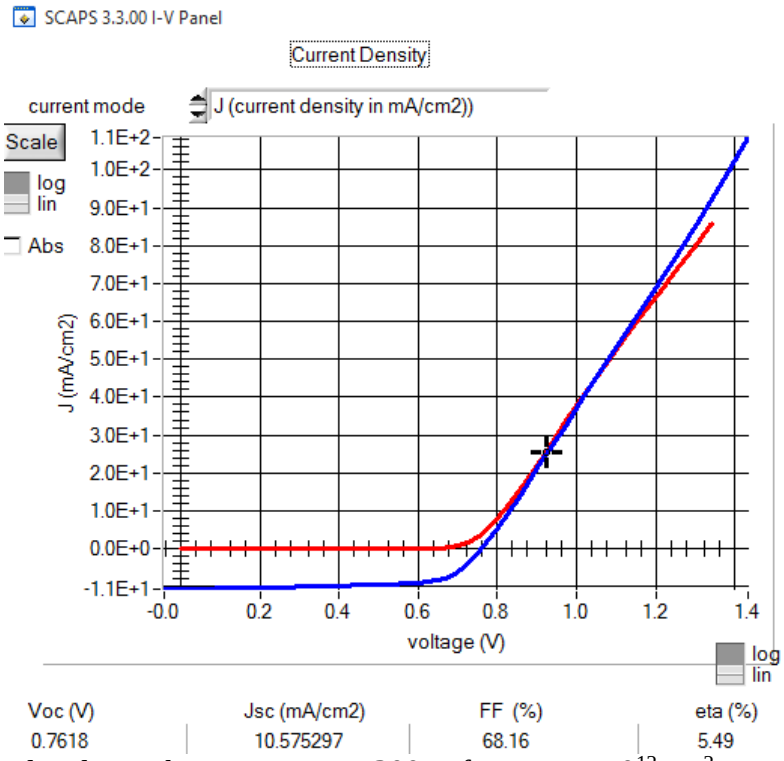

Figure 4.9 Simulated J-V characteristics at 300 K for Nit: 7 x$10^{12}$$cm^{-2}$

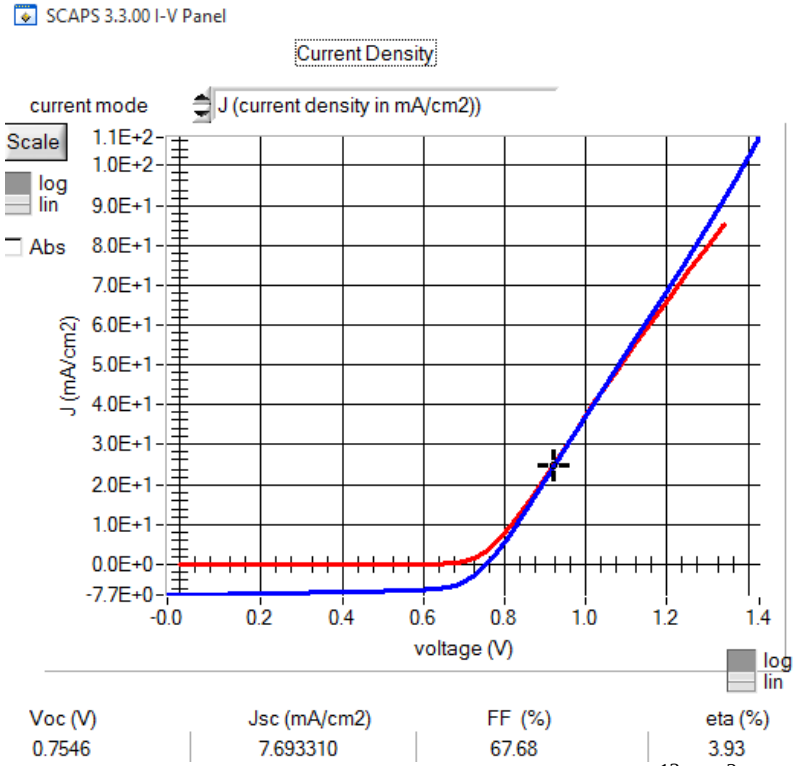

Figure 4.10 Simulated J-V characteristics at 300 K for Nit: 1 x$10^{13}$$cm^{-2}$

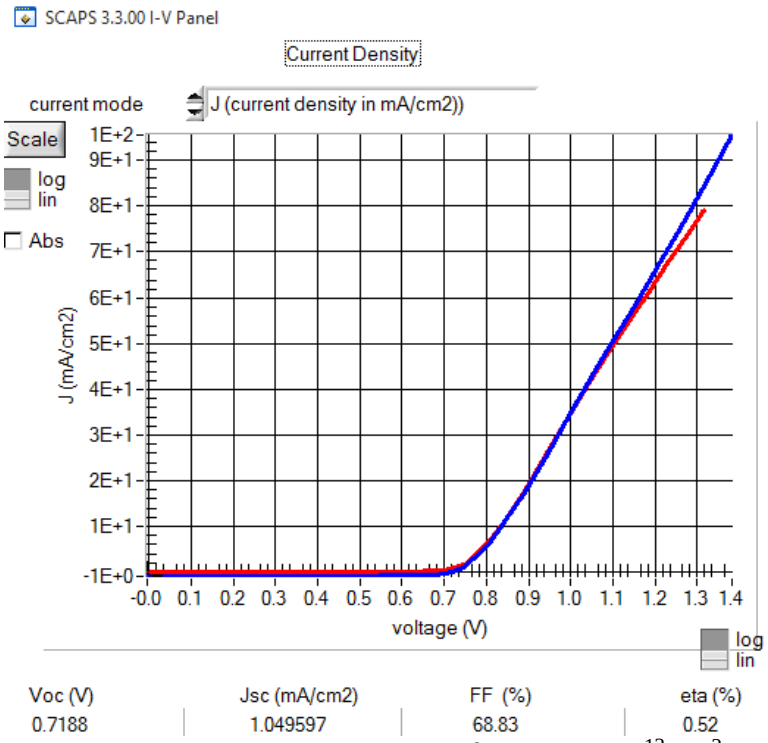

Figure 4.11 Simulated J-V characteristics at 300 K for Nit: 5 x$10^{13}$$cm^{-2}$

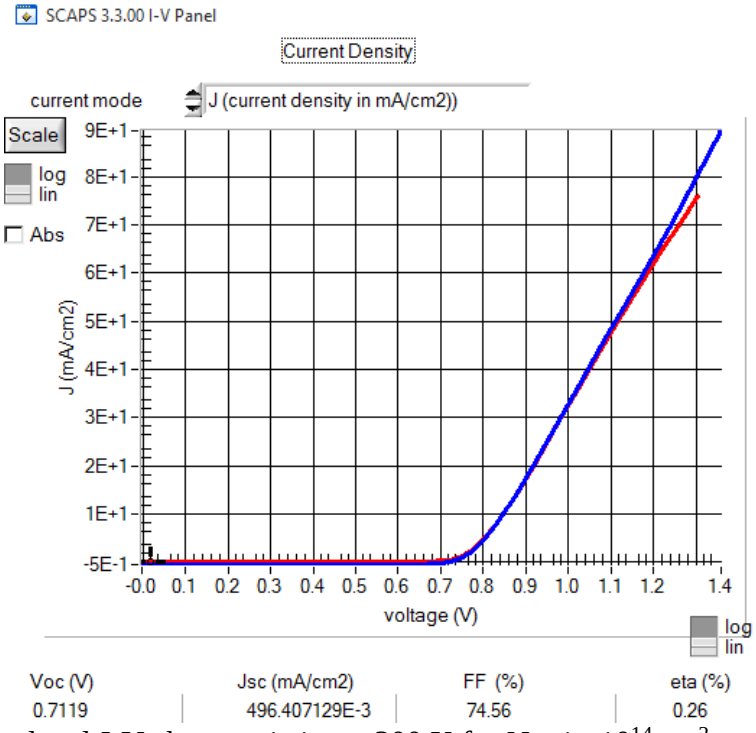

Figure 4.12 Simulated J-V characteristics at 300 K for N_{it}: 1 x$10^{14}$$cm^{-2}$

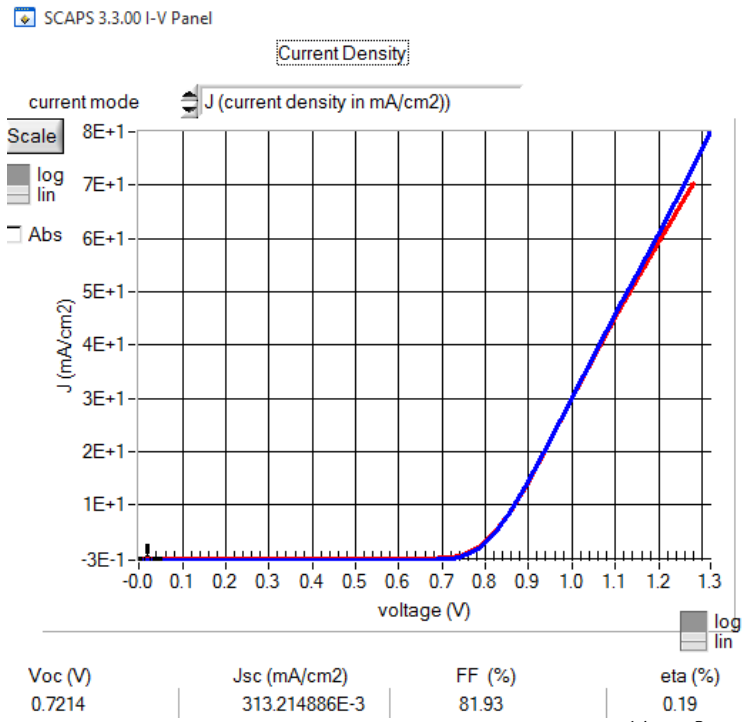

Figure 4.13 Simulated J-V characteristics at 300 K for N_{it}: 3 x$10^{14}$$cm^{-2}$

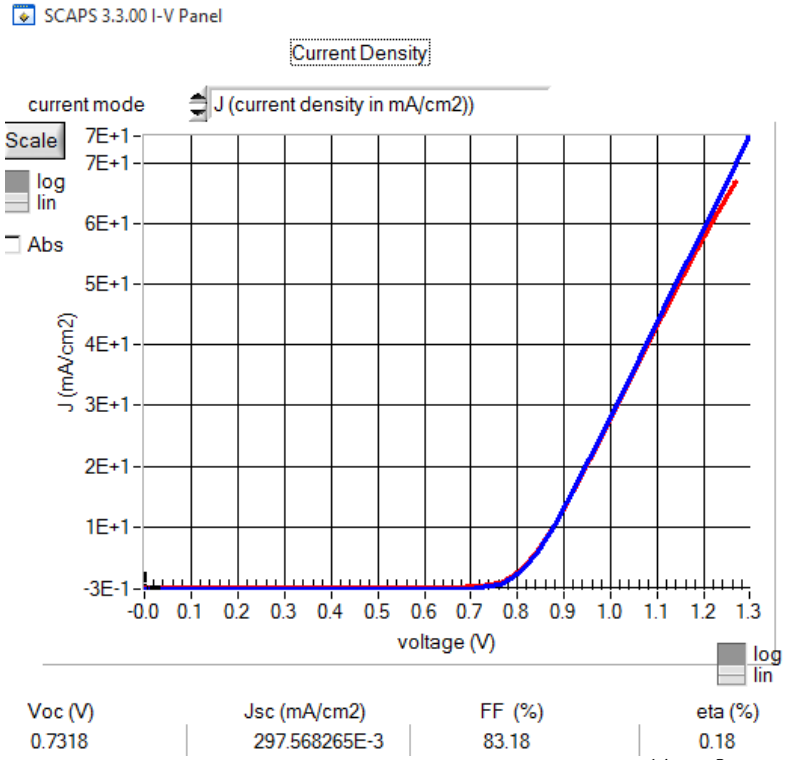

Figure 4.14 Simulated J-V characteristics at 300 K for N_{it}: 6 x$10^{14}$$cm^{-2}$

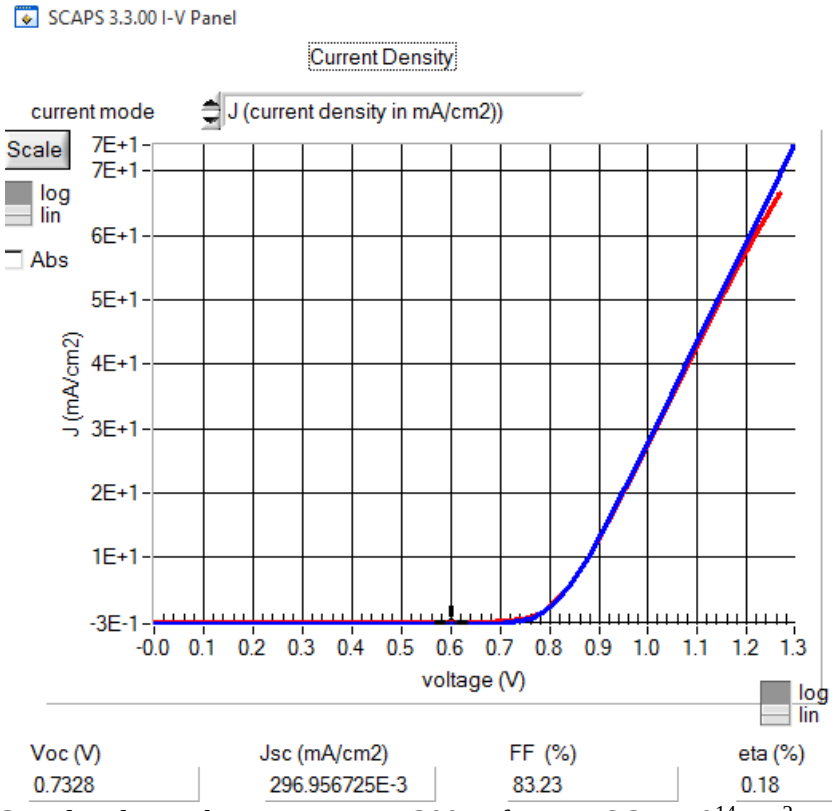

Figure 4.15 Simulated J-V characteristics at 300 K for Nit: 6.35 x$10^{14}$$cm^{-2}$

Figure 4.16 shows the simulated I-V curves and table 4.1 shows the values of Voc, Jsc, FF and efficiency at various interface state densities. The interface recombination current increases the dark saturation current of the solar cell and decrease the collection efficiencies. Thus, it decreases the short circuit current and therefore, the efficiency of the solar cell. [27] As can be seen from the figure 4.16 and table 4.1, Voc and Jsc decreases as the total density of interface states increases, and thus, the efficiency is reduced.

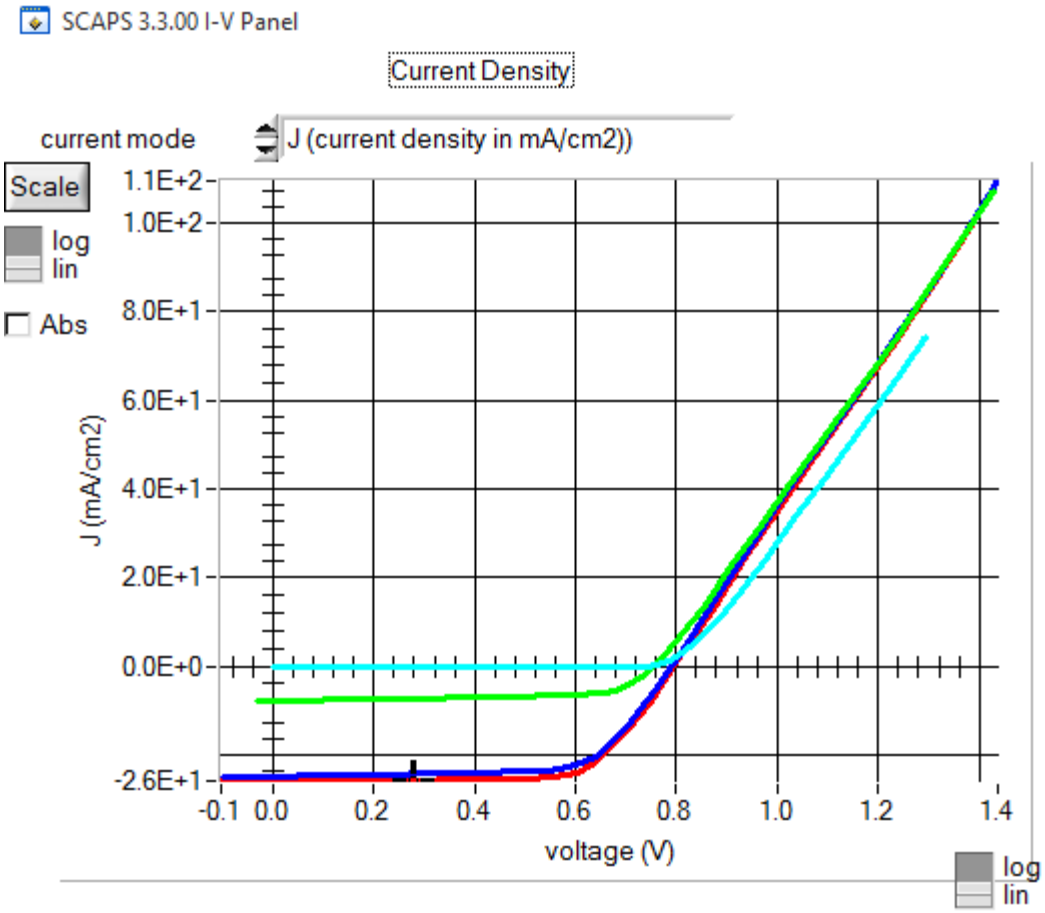

Figure 4.16: Simulated light I-V curves of nw-CdS/CdTe device at various interface state densities

Table 4.1 Effect of interface state density on Voc, Isc, FF and Efficiency

	Red curve	Blue curve	Light Green curve	Aqua Blue curve
Total density (1/cm^2) at CdS/CdTe interface	6.000e+11	1.000e+12	1.000e+13	6.350e+14
RESULTS				
Voc(V) ↓	0.7964	0.7898	0.7546	0.7328
Jsc(mA/cm^2) ↓	25.79	24.79	7.69	0.296
FF (%)	70.17	68.52	67.68	83.23
Efficiency (%) ↓	14.42	13.42	3.93	0.18

4.1.2 Effect of Surface recombination velocity at interface

Surface recombination velocity is an important parameter that affects the dark saturation current and the quantum efficiency of a solar cell. Interfaces introduce band of electronic states in the band gap that can be ascribed to broken or strained bonds and impurities. [5]

The surface recombination velocity at the interface is given by

$$S_n = \sigma_n v_{th} N_{it} \text{ - For electrons} \quad (43)$$

$$S_p = \sigma_p v_{th} N_{it} \text{ – For holes} \quad (44)$$

Where, N_{it} - Density of interface traps

v_{th} - Thermal velocity

σ_p , σ_n –Capture cross section of holes and electrons, respectively

The interface recombination velocities were varied in the simulations from the range of 6x 10^2 -6x 10^7 cm/s and simulations were performed. Figures 4.17-4.22 show the simulated J-V characteristics of solar cell for the range of surface recombination velocities.

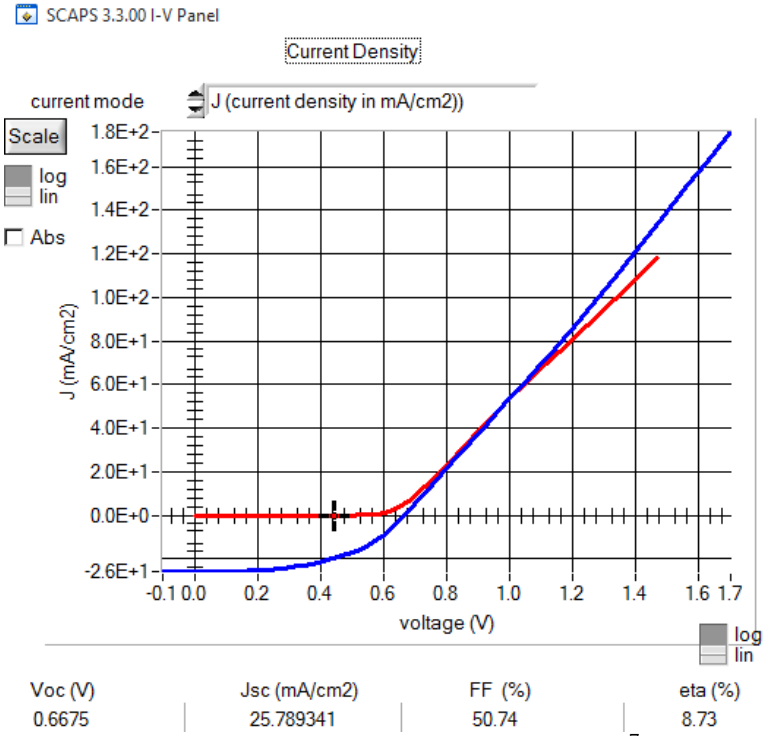

Figure 4.17 Simulated J-V characteristics at 300 K for Sn: 6x10^7 cm/s

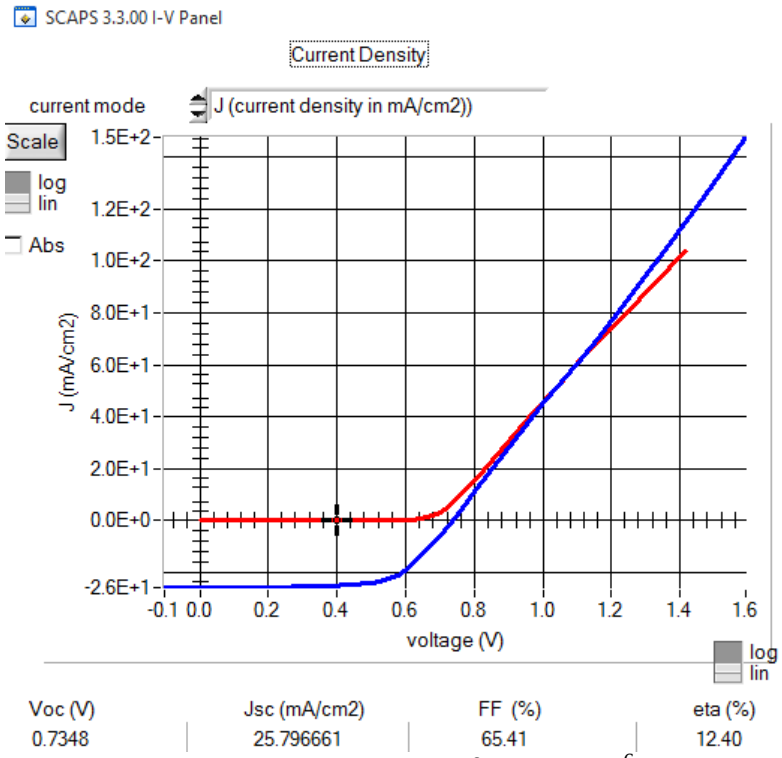

Figure4.18 Simulated J-V characteristics at 300 K for S_n: $6x10^6$ cm/s

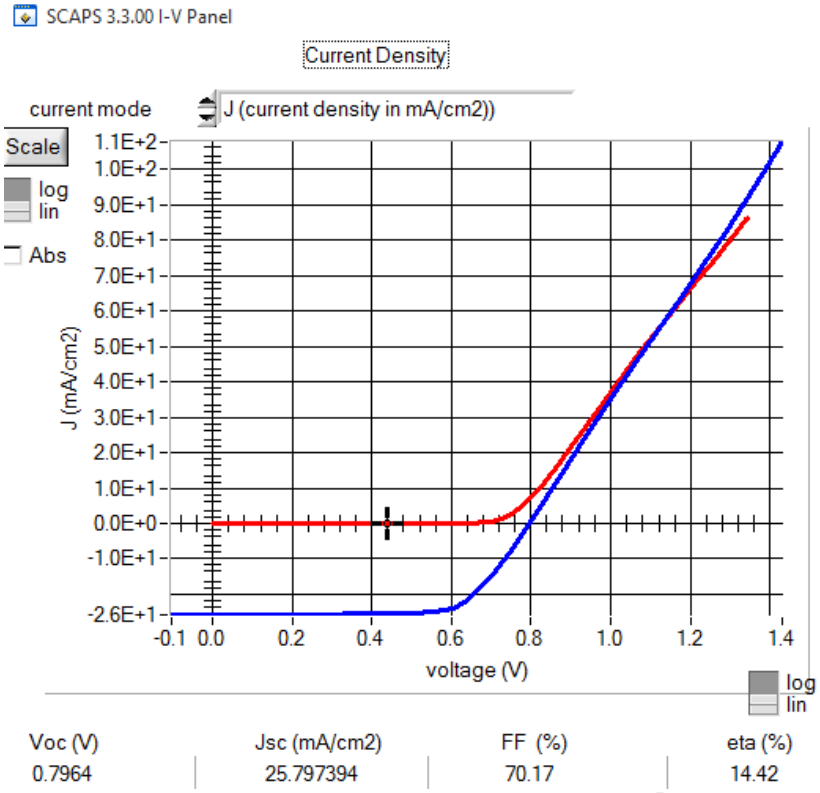

Figure 4.19 Simulated J-V characteristics at 300 K for Sn: $6x10^5$ cm/s

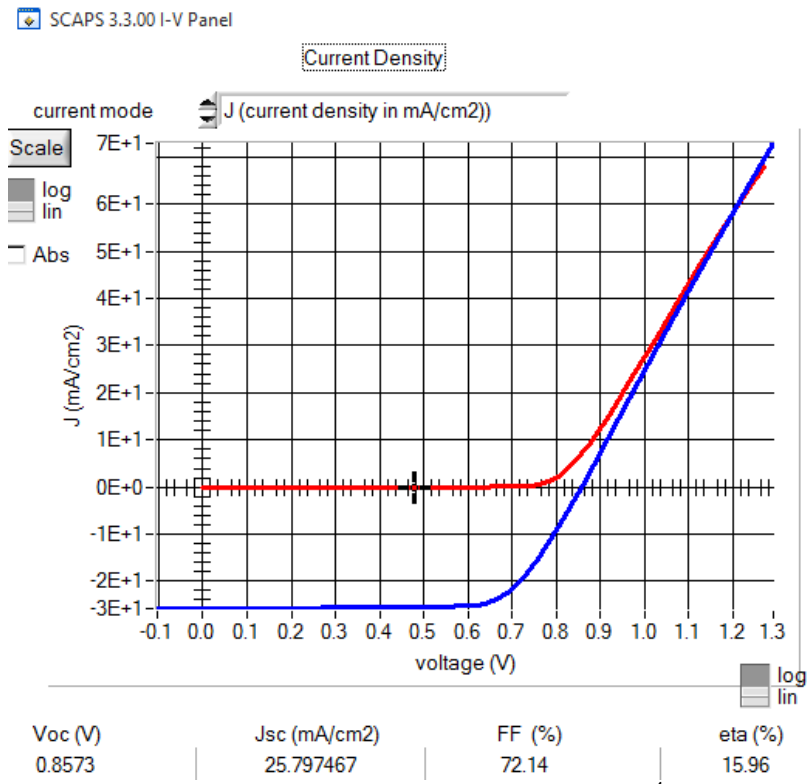

Figure 4.20 Simulated J-V characteristics at 300 K for Sn: $6x10^4$ cm/s

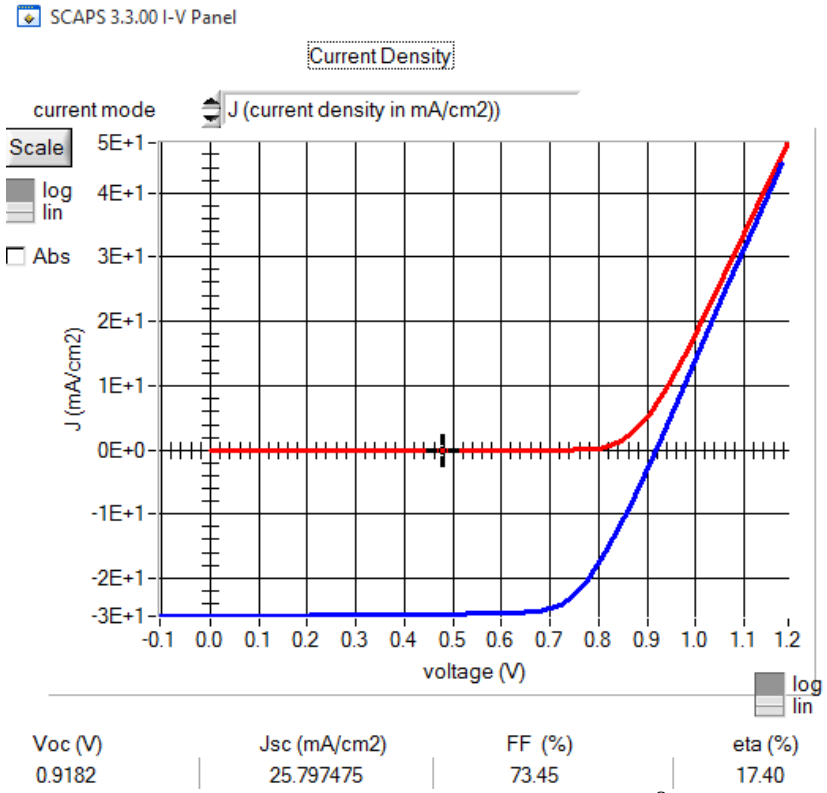

Figure 4.21 Simulated J-V characteristics at 300 K for S_n: $6x10^3$ cm/s

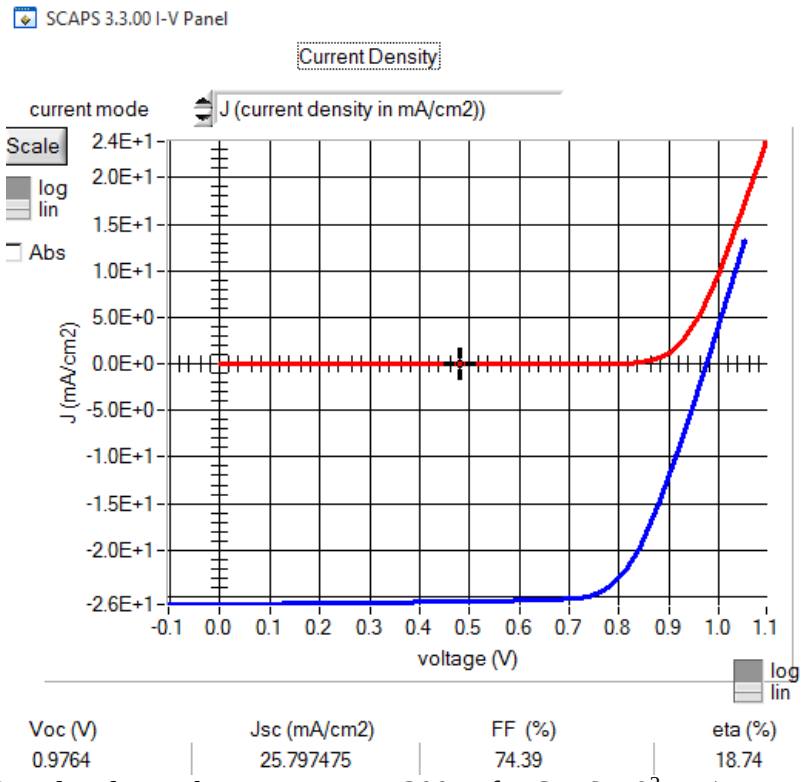

Figure 4.22 Simulated J-V characteristics at 300 K for Sn: $6x10^2$ cm/s

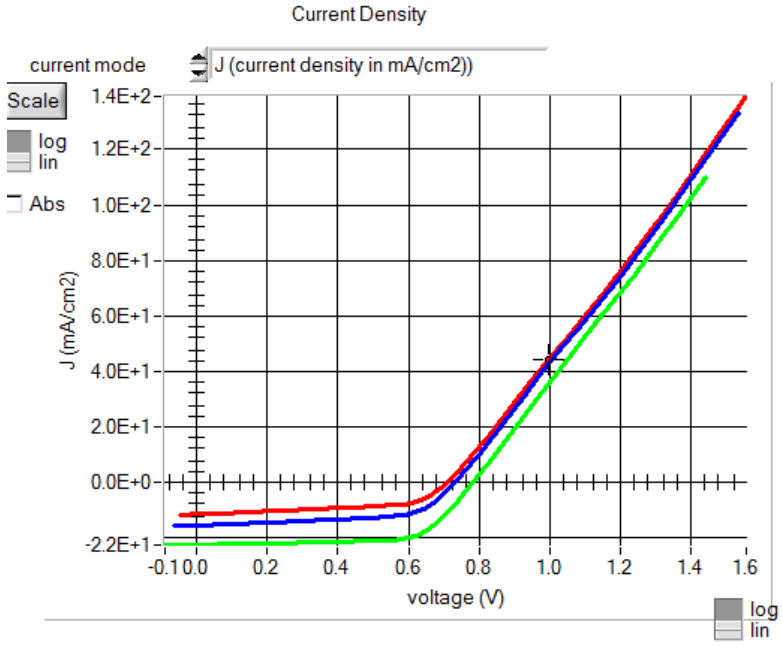

Figure 4.23 Simulated light I-V curves of nw-CdS/CdTe device at various interface recombination velocity

As can be seen from the figure 4.23 and table 4.2, Voc and Jsc increases as interface recombination velocity decreases, and thus, the efficiency increases.

Table 4.2 Effect of interface recombination velocity on Voc, Isc, FF and Efficiency

	Red	Blue	Light Green
Interface recombination velocity(cm/s)	$1.6x10^7$	$8.8\ x10^6$	$1.6x10^6$
RESULTS			
Voc(V) ↑	0.7103	0.7317	0.7839
Jsc(mA/cm^2) ↑	11.378436	15.40024	22.317618
FF (%) ↑	56.11	60.62	68.27
Efficiency (%) ↑	4.53	6.83	11.94

4.1.3. Effect of CdS and CdTe effective density of states

4.1.3.1 Effect of CdS effective density of states (N_c):

The effect of N_c and N_v can be explained from equation (2) – (4). As N_c/ N_v increases, the dark saturation current increases, thus open circuit voltage Voc decreases. Therefore, the efficiency of a solar cell decreases.

In order to verify the simulated model, the effective density of states in the conduction band of CdS-nw was varied from the range 8×10^{18} to 8×10^{19} cm^{-3} and I-V simulations were performed.

As can be seen from figure 4.24 and table 4.3, as N_c increases in CdS-nw, the open circuit voltage reduces and the efficiency is reduced.

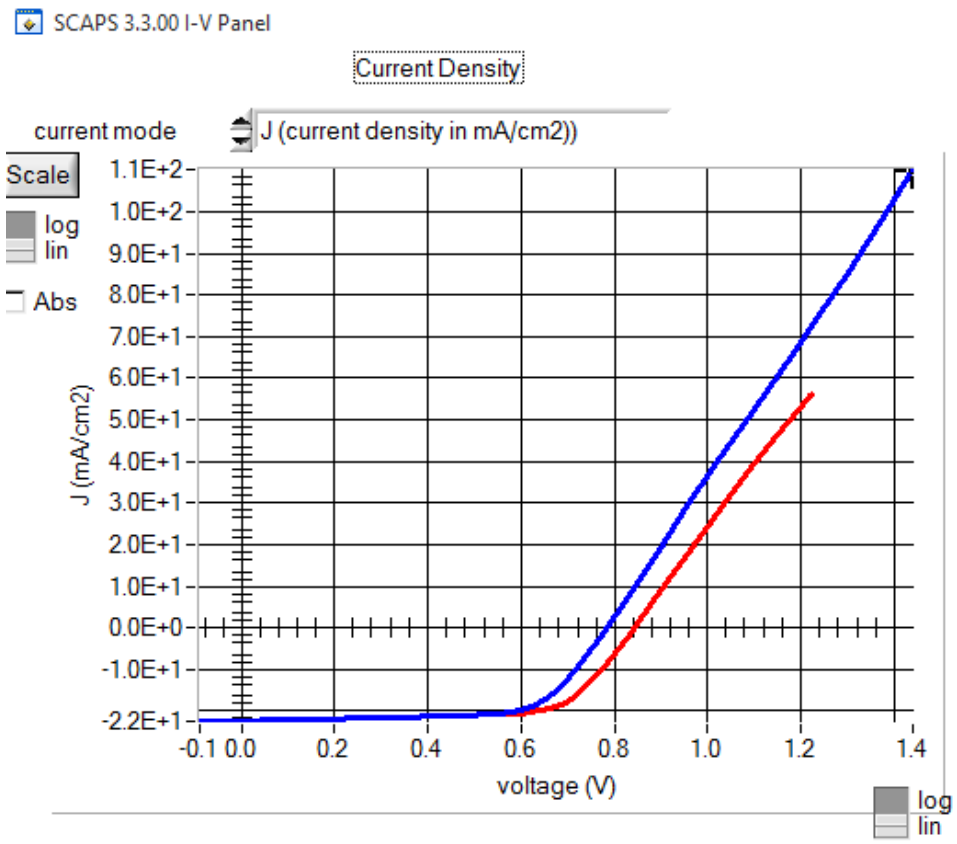

Figure 4.24 Simulated light I-V curves of nw-CdS/CdTe device at various Nc in CdS-nw

Table 4.3 Effect of Nc of CdS-nw on Voc, Isc, FF and Efficiency

	Red curve	Blue Curve
Nc in CdS-nw (1/cm^3)	8.000E+18	8.000E+19
RESULTS		
Voc(V) ↓	0.8441	0.7839
Jsc(mA/cm^2)	22.31	22.32
FF (%)	68.42	68.27
Efficiency (%) ↓	12.89	11.94

4.1.3.2 Effect of CdTe effective density of states (N_v)

The effective density of states in the valence band (N_v) were varied 8 x 10^{18} to 8 x 10^{19} cm^{-3} and I-V simulations were performed.

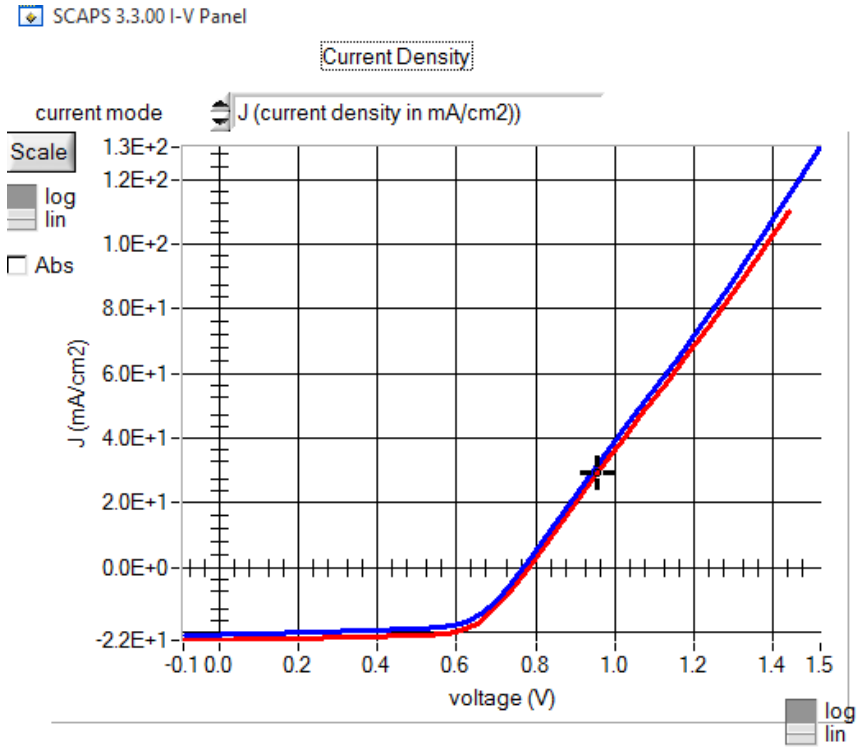

Figure 4.25 Simulated light I-V curves of nw-CdS/CdTe device at various Nv in CdTe

Table 4.4 Effect of N_v of CdTe on Voc, Isc, FF and Efficiency

	Red curve	Blue Curve
Nv in CdTe (1/cm^3)	8.000E+18	8.000E+19
RESULTS		
Voc(V) ↓	0.7839	0.722
Jsc(mA/cm^2)	22.32	20.71
FF (%)	68.27	66.99
Efficiency (%) ↓	11.94	10.71

As can be seen from figure 4.25 and table 4.4, as N_v increases in CdTe, the open circuit voltage reduces and the efficiency is reduced.

4.1.4. Effect of defect in CdTe layer

The recombination at defect level plays an important role in I-V characteristics. SCAPS-1D allows the user to specify the defect at each layer. The acceptor defect is simulated in CdTe layer for this model. The trap energy level E_t is 0.09 above the valence band of CdTe. The trap densities were varied from the range 9.9 $x10^{13}$ to 9.9 $x10^{17}$ cm^{-3} and simulations were performed at 300 K. Fig. 4.26-4.28 show the simulated J-V characteristics of solar cell for the range of defect densities.

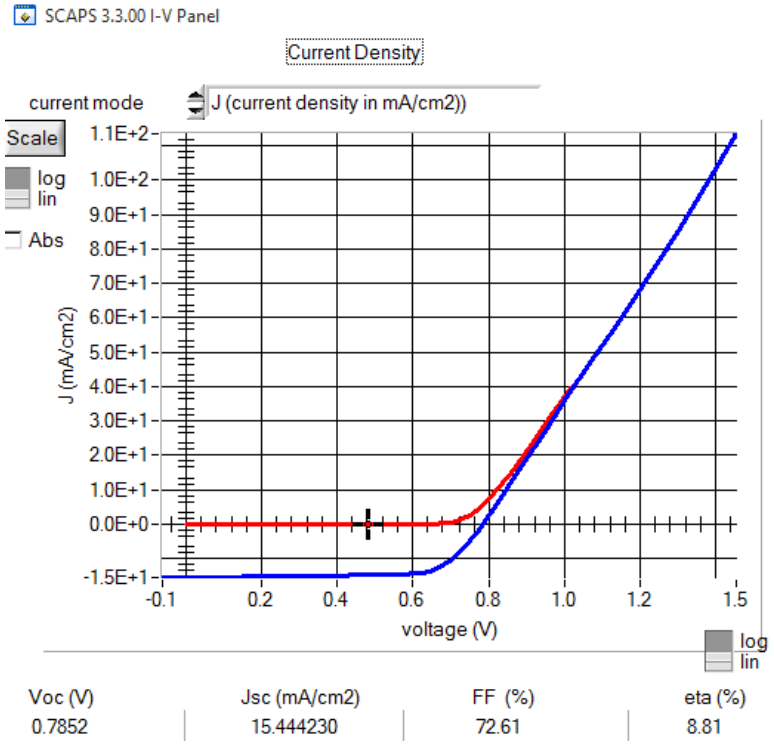

Figure 4.26 Simulated J-V characteristics at 300 K for N_t: 9.9 $x10^{17}cm^{-2}$

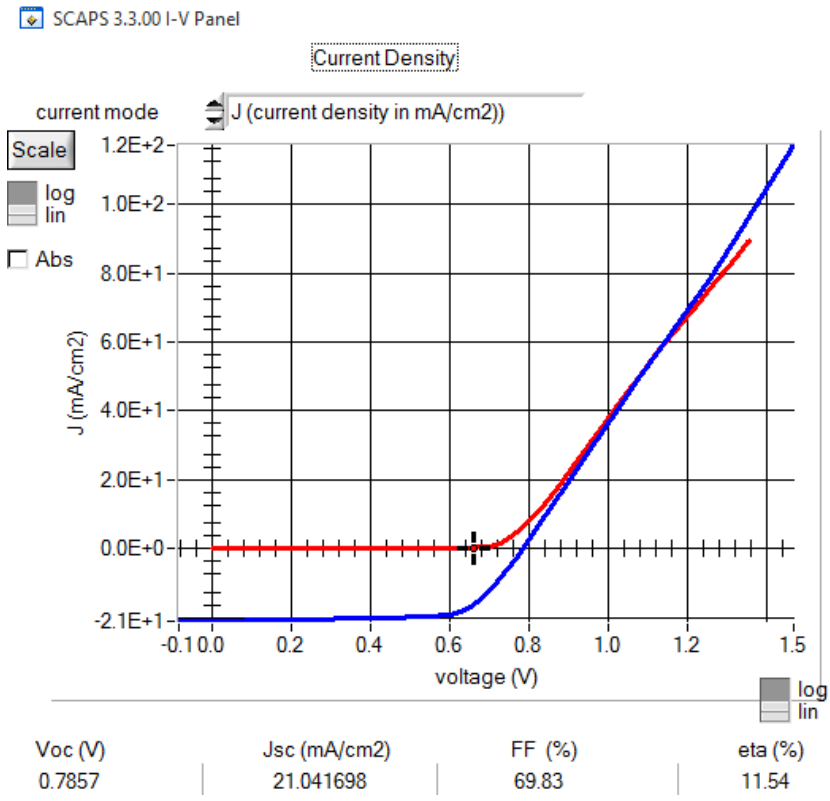

Figure 4.27 Simulated J-V characteristics at 300 K for Nt: 9.9 x$10^{16}$$cm^{-2}$

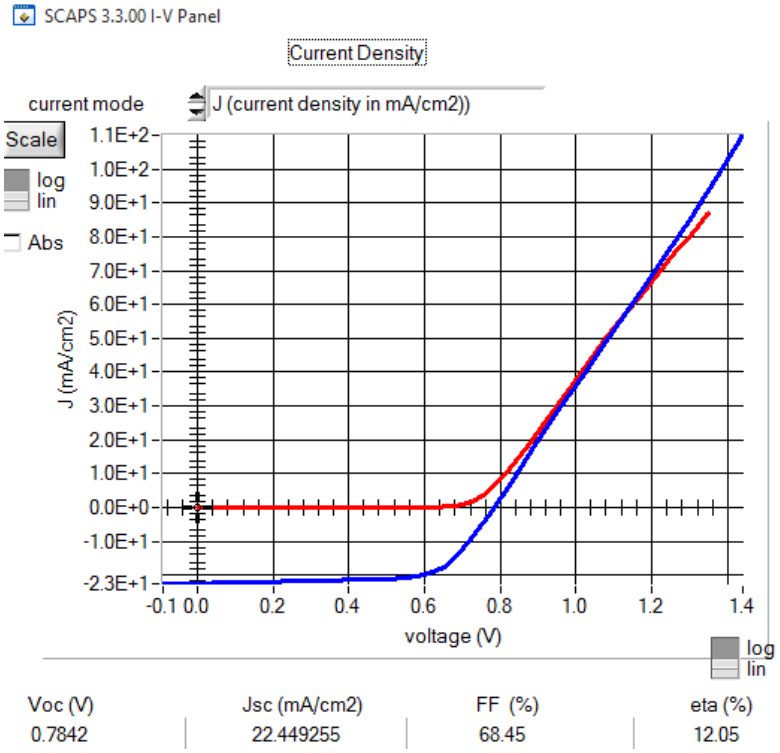

Figure 4.28 Simulated J-V characteristics at 300 K for Nt: 9.9 x$10^{13}$$cm^{-2}$

Table 4.5 Effect of trap density of CdTe on Voc, Isc, FF and Efficiency

	Red curve	Blue Curve
N_t in CdTe (1/cm^3)	9.9E+13	9.9E+16
RESULTS		
Voc(V)	0.7842	0.7857
Jsc(mA/cm^2) ↓	22.45	21.04
FF (%)	68.45	69.83
Efficiency (%) ↓	12.05	11.54

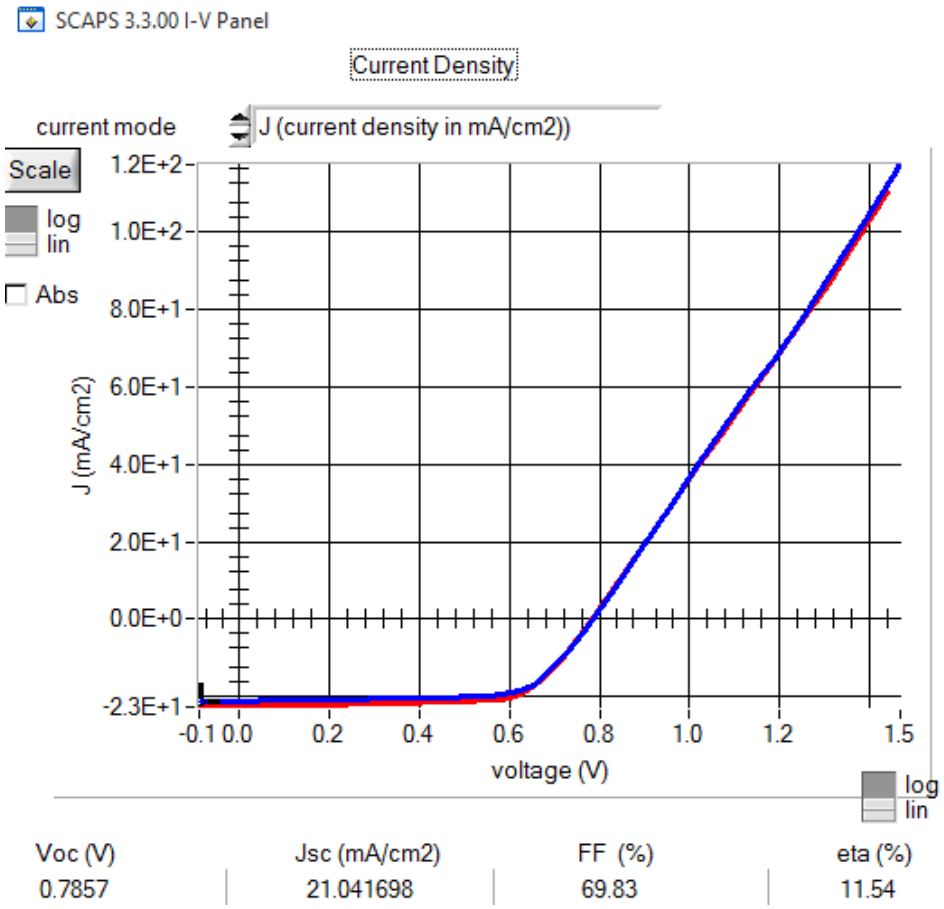

Figure 4.29 Simulated light I-V curves of nw-CdS/CdTe device at various Nt in CdTe

As can be seen from figure 4.29 and table 4.5, as N_t increases in CdTe, the short circuit current decreases and the efficiency is reduced.

4.1.5. Effect of metal work function

The metal work function is defined as the energy needed to bring an electron from the Fermi level to the vacuum level. The back contact can be ohmic or Schottky depending upon the work functions of metal and CdTe. An ohmic contact will allow the transfer of free carriers while the Schottky contact will have a barrier at the back contact for the transfer of carriers. The metal work function of the CdTe contact was varied from 5-5.7 eV and the simulations were performed. Fig. 4.30-4.38 show the simulated J-V characteristics of solar cell for the range of defect densities.

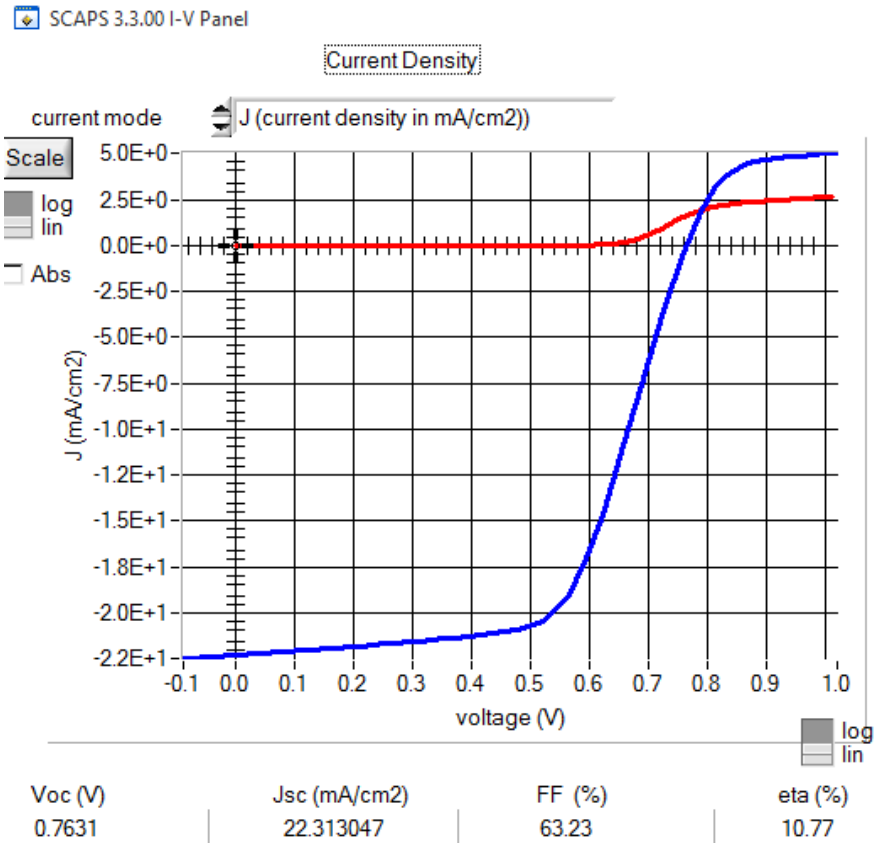

Figure 4.30 Simulated J-V characteristics at 300 K for metal work function: 4.87eV

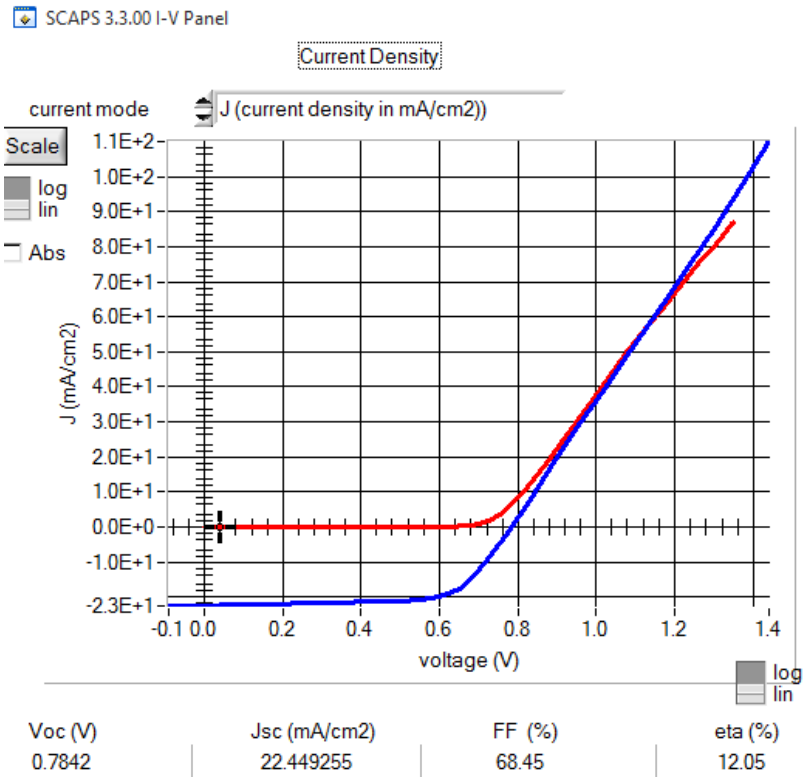

Figure 4.31 Simulated J-V characteristics at 300 K for metal work function: 5.0 eV

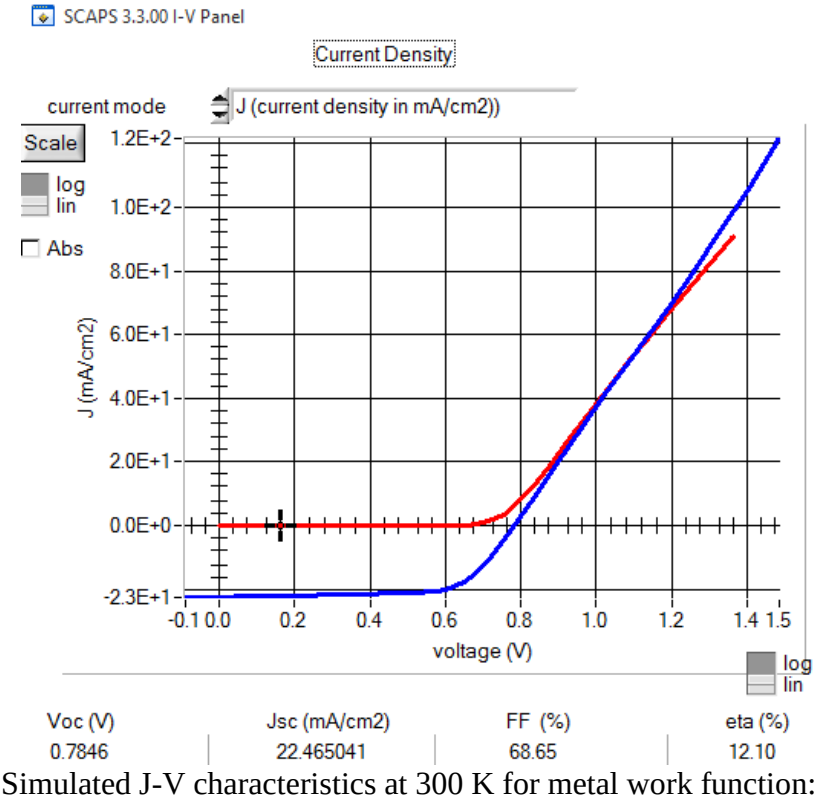

Figure 4.32 Simulated J-V characteristics at 300 K for metal work function: 5.1 eV

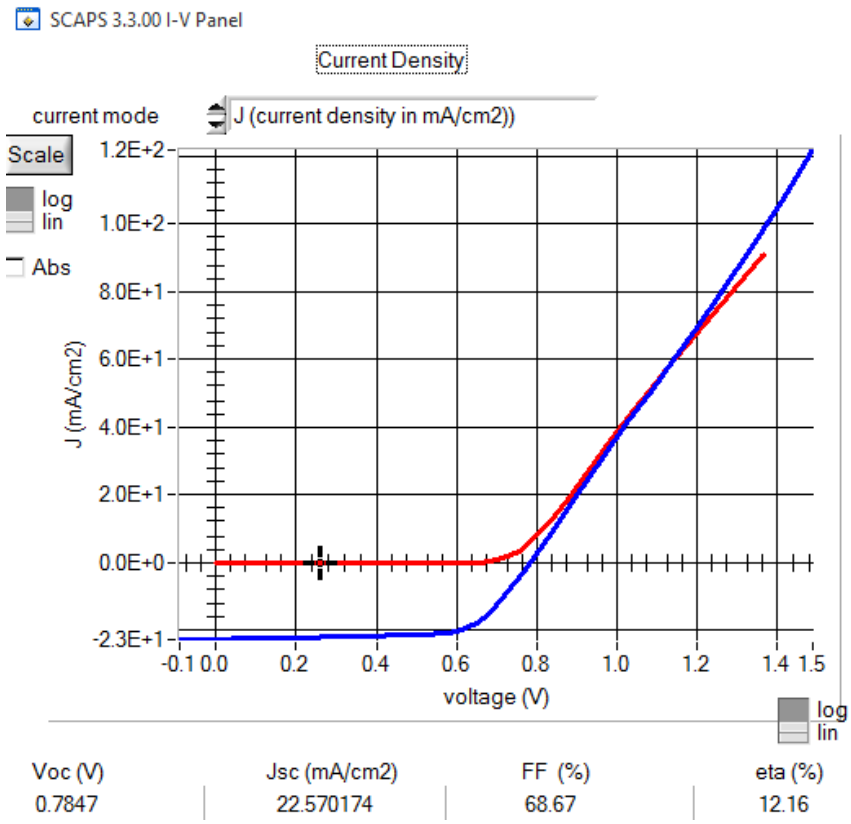

Figure 4.33 Simulated J-V characteristics at 300 K for metal work function: 5.2 eV

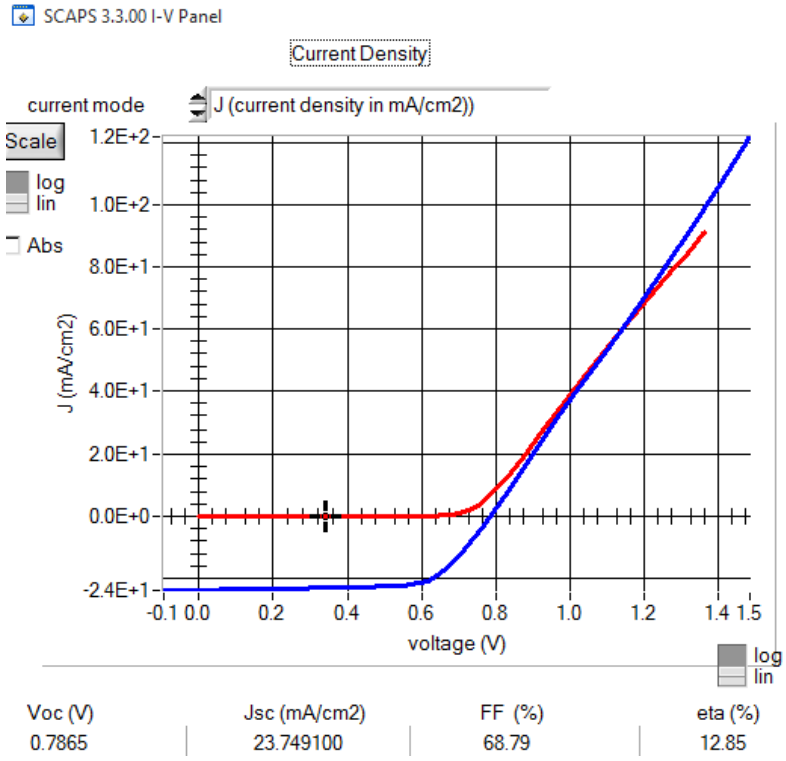

Figure 4.34 Simulated J-V characteristics at 300 K for metal work function: 5.3 eV

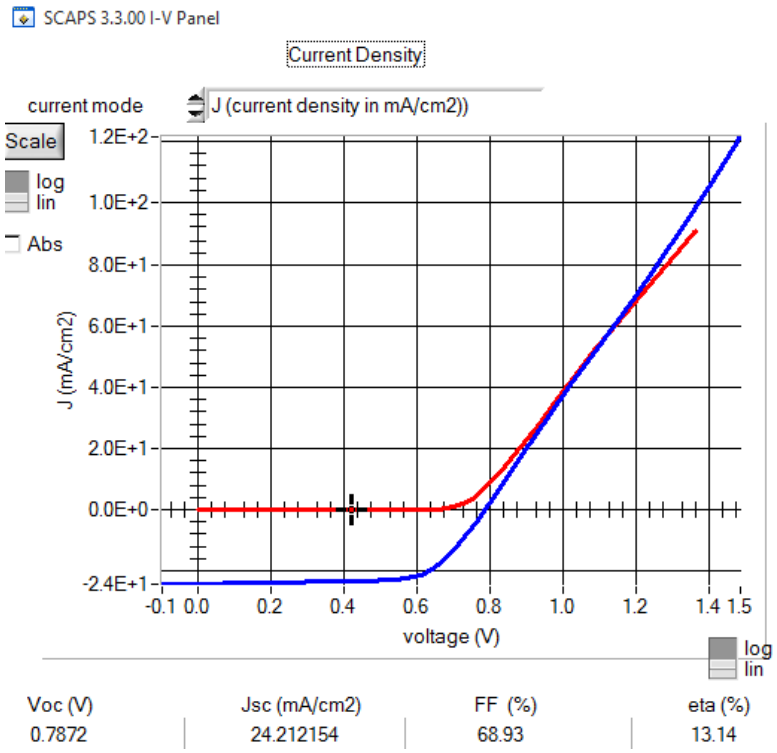

Figure 4.35 Simulated J-V characteristics at 300 K for metal work function: 5.4 eV

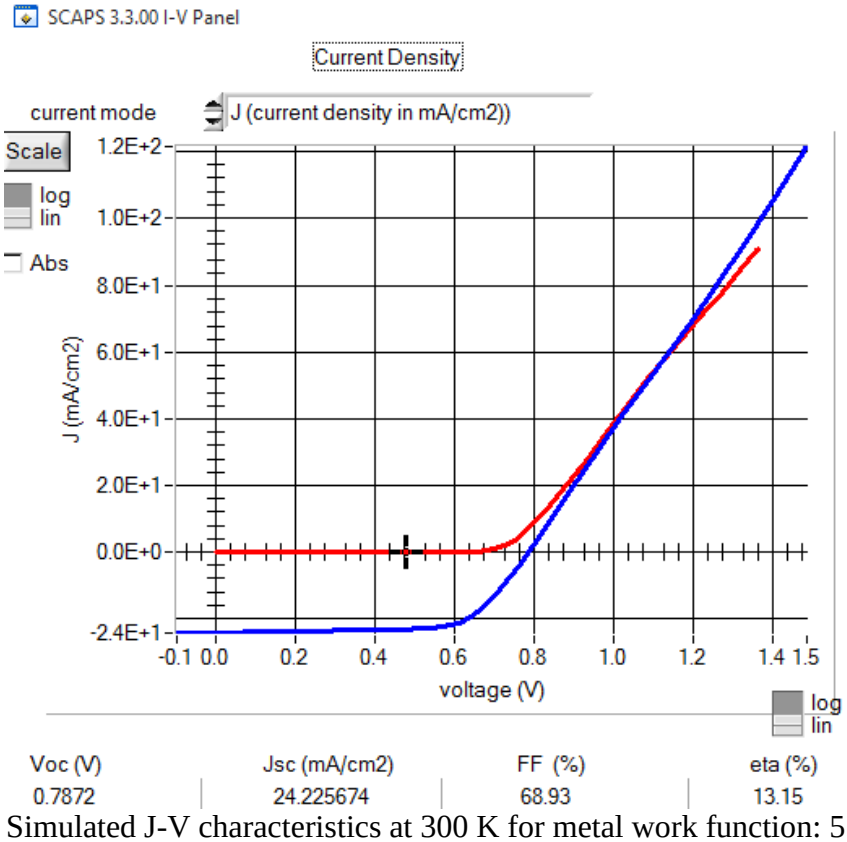

Figure 4.36 Simulated J-V characteristics at 300 K for metal work function: 5.5 eV

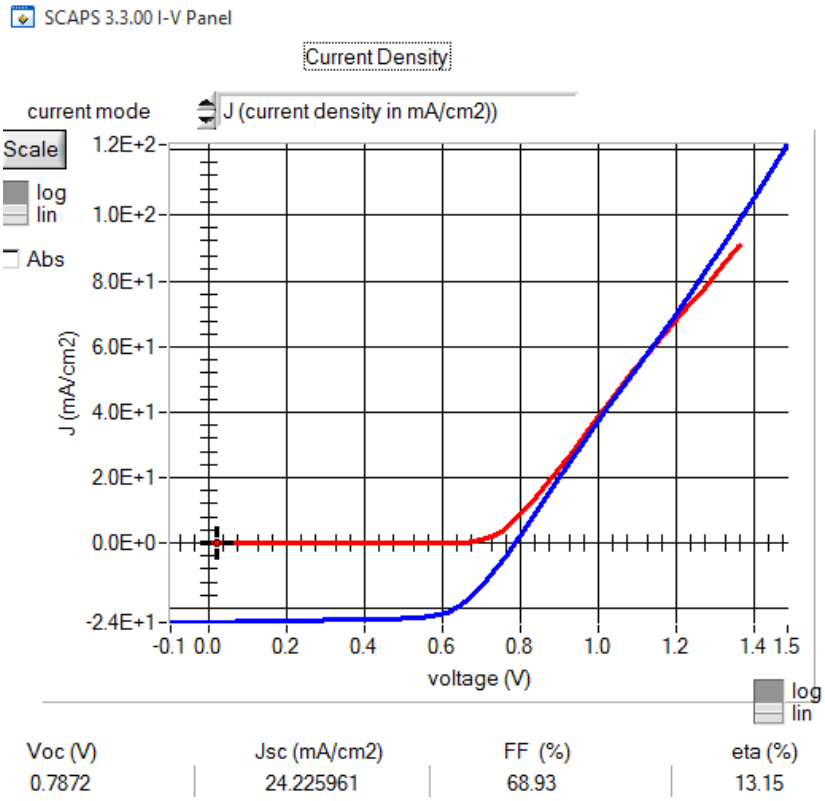

Figure 4.37 Simulated J-V characteristics at 300 K for metal work function: 5.6 eV

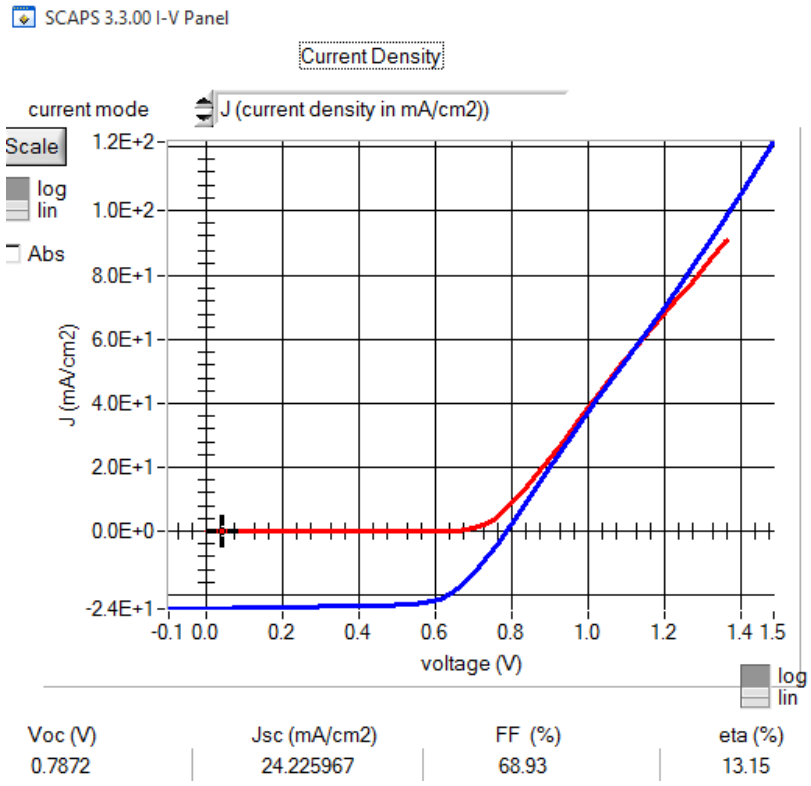

Figure 4.38 Simulated J-V characteristics at 300 K for metal work function: 5.7 eV

It can be observed from figures 4.35 to 4.38, the J-V characteristics show similar results as the CdTe contact becomes the ohmic contact from metal work function 5.4 and above and it allows the flow of carriers towards the absorber layer.

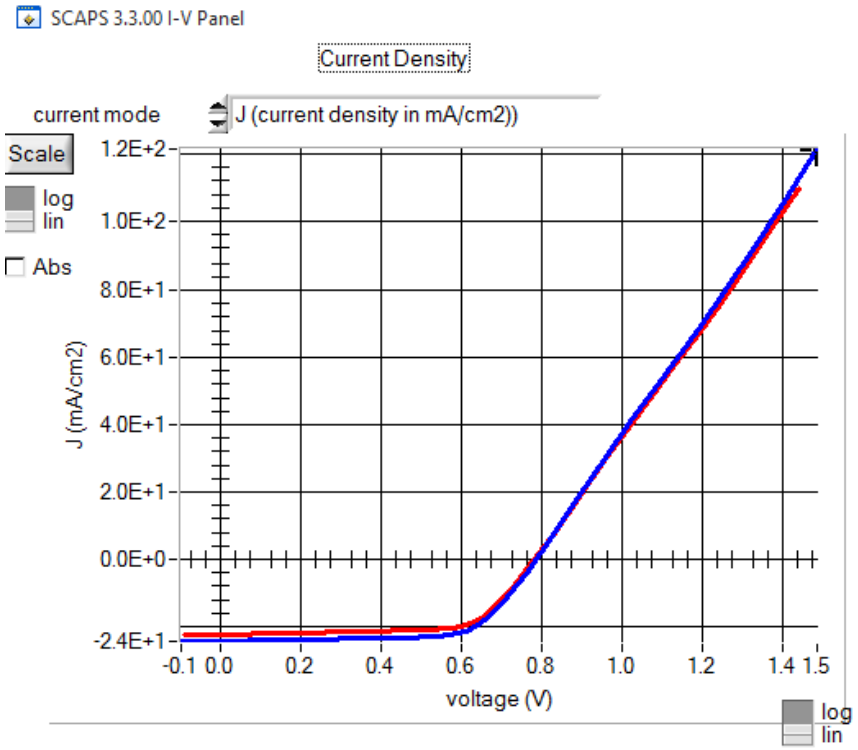

Figure 4.39 Simulated light I-V curves of nw-CdS/CdTe device at various metal work function

Table 4.6 Effect of metal work function on Voc, Isc, FF and Efficiency

	Red curve	Blue Curve
Metal work function (eV)	5	5.4
Majority carrier barrier height [relative to Ef](eV)	0.4	0.0
RESULTS		
Voc(V) ↑	0.7839	0.7872
Jsc(mA/cm^2) ↑	22.32	24.22
FF (%) ↑	68.27	68.93
Efficiency (%) ↑	11.94	13.14

As can be seen from figure 4.39 and table 4.6, as metal work function increases, the majority carrier barrier height with respect to the Fermi level is reduced. The open circuit voltage is increased and the efficiency is enhanced.

4.1.6 Simulated J-V characteristics at 300 K

J-V characteristics for 300 K were simulated using the optimum values of the interface state density, defect density, metal work function, surface recombination velocity, shunt and series resistance. The objective was to obtain the highest efficiency, with no convergence failure and no crossover or rollover effect.

The values for series resistance were varied from 0.5-5 ohm and shunt resistance from $1.0x10^{15}$ to $1.0\ x10^{20}$ ohm.cm^2. The range of the values for other parameters was varied as mentioned in the previous sections 4.1.1-4.1.5.

Figure 4.40 shows the simulated J-V characteristics at 300 K with the efficiency of 22.26%. The open circuit voltage of 0.9828 V and short circuit current of 26.724 mA/cm^2 with the fill factor of 84.73 was observed here. There was no crossover and rollover effect.

Table 4.7 shows the parameter values used for achieving highest efficiency of 22.26% and the parameters which were used in order to fit the experimental data at 300 K. Figure 4.40 shows no rollover or crossover effect and it can be concluded here that the efficiency of the solar cell can be improved by reducing the interface state density, surface recombination velocity at the interface, metal work function and the bulk resistance.

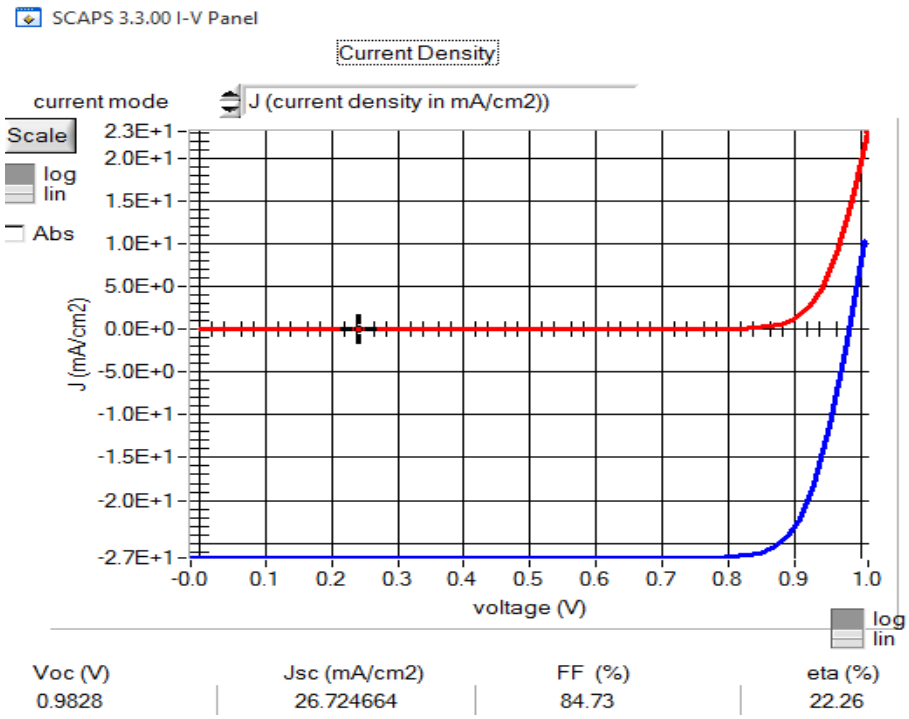

Figure 4.40 Simulated J-V curve at 300 K

Table 4.7 Parameters used for simulated J-V curves at 300 K with 22.26% efficiency and 12.08% efficiency

Parameters	Values used for achieving highest efficiency (η=22.26%)	Values used for J-V curve fitting (η=12.08%)
Total density (integrated over all energies) (1/cm^2) at CdS/CdTe interface	6.0x10^{11}	1.60 x10^{12}
Surface recombination velocity at the interface (cm/s)	6.0x10^2	1.6x10^6
Metal work function at CdTe contact (eV)	5.5	5
Series Resistance (ohm)	0.5	4.0
Shunt Resistance (ohm.cm^2)	1.0x10^{20}	1.0x10^{15}

4.2 J-V curve fitting

J-V characteristics of nanowire CdS/CdTe solar cell, tested under standard conditions of room temperature and 100 mW/cm^2 irradiation were experimentally obtained by Dr. Hongmei Dang [10]. The cell had an area of 0.018 cm^2, and yielded an open-circuit voltage V_{oc} of 770 mV, a short current density J_{sc} of 26 mA/cm^2, a fill factor, FF of 60%, and a power conversion efficiency (PCE) of 12%. It should be noted that the 12% efficiency value was achieved on an intrinsic SnO_2/ITO-soda-lime glass substrate and without antireflective coating.

Figure 4.41 shows the experimental curve under dark and 1-sun illumination at 296 K.

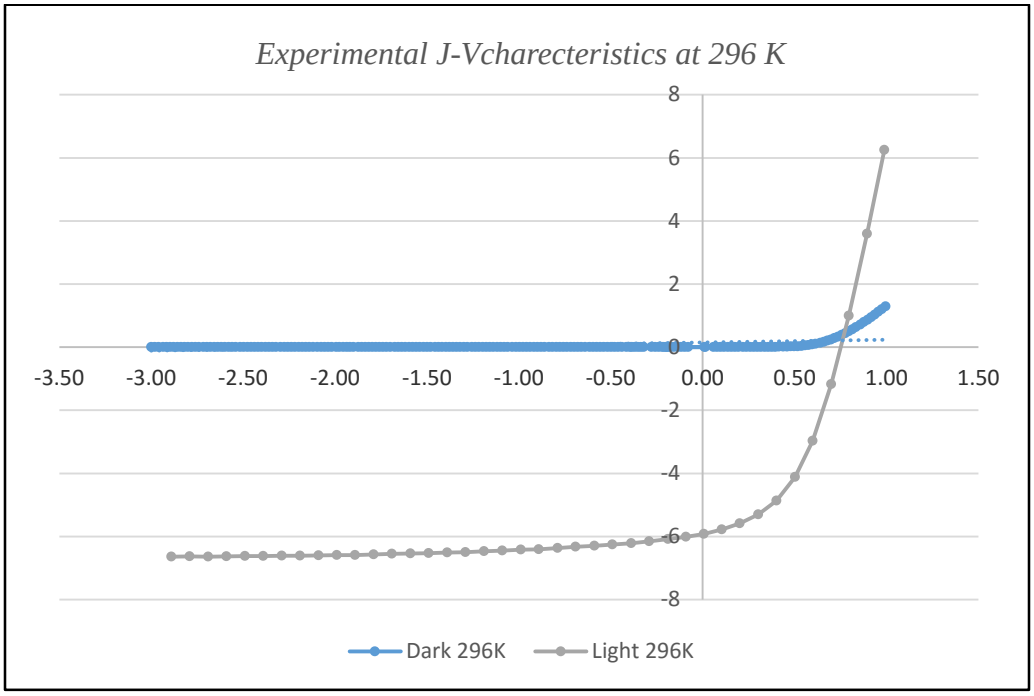

Figure 4.41 Experimental J-V curves (dark and light) of nw-CdS/CdTe device at 296K

The properties of the device in the simulations such as interface recombination velocity, interface state density, defects, Nc, Nv, etc. were varied in order to get the most perfect fit with the experimental results for the temperature 300 K. The parameters were kept constant for lower temperatures and the simulations were performed.

Figure 4.42 shows the simulated J-V light and dark curve at 296 K which is a best fit for the experimental curves.

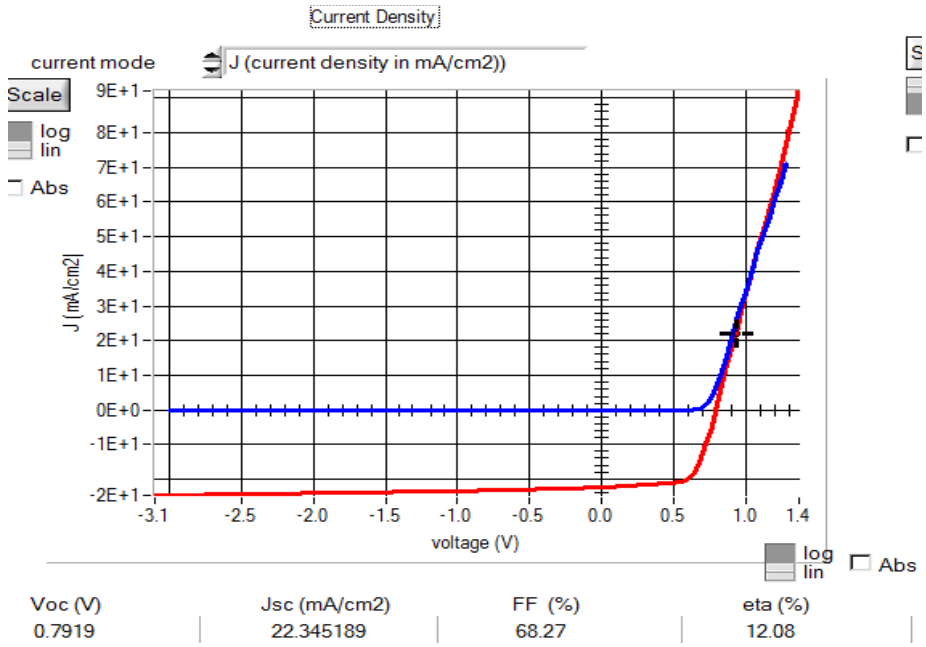

Figure 4.42 Simulated J-V curves (dark and light) of nw-CdS/CdTe device at 296K

Figure 4.43 – figure 4.50 show the experimental and simulated J-V light and dark curves at 296K, 275K, 250 K and 225K individually with R^2 co-efficient.

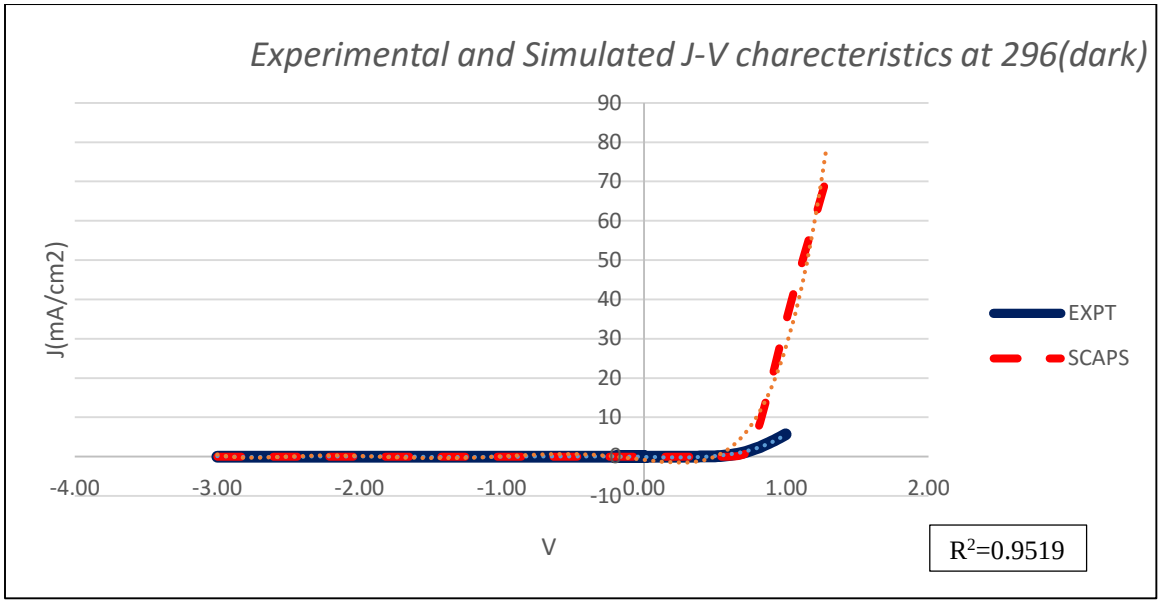

Figure 4.43 J-V curves fitting (dark) of nw-CdS/CdTe device at 296K

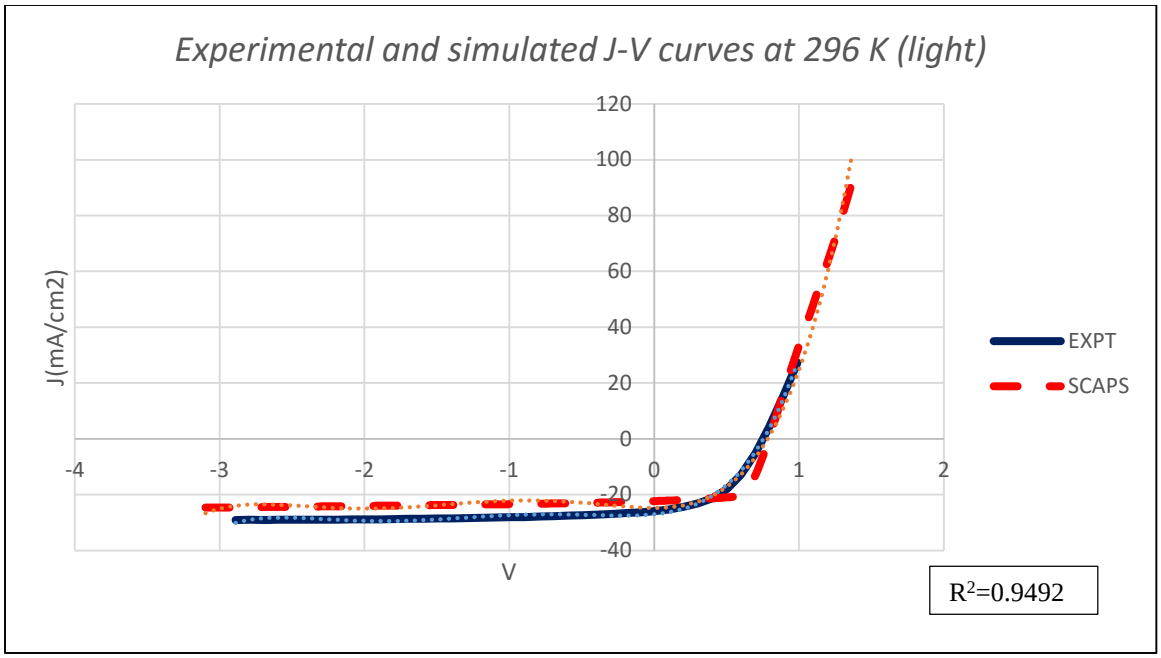

Figure 4.44 J-V curves fitting (light) of nw-CdS/CdTe device at 296K

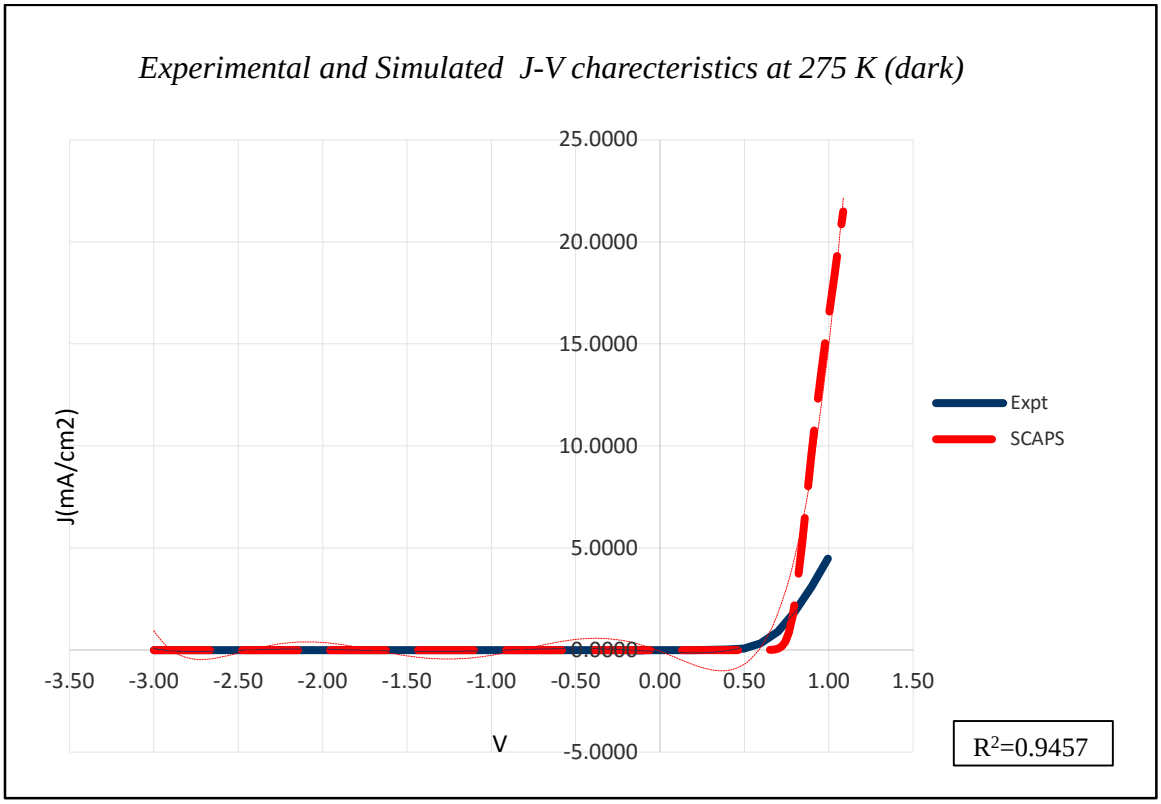

Figure 4.45 J-V curves fitting (dark) of nw-CdS/CdTe device at 275K

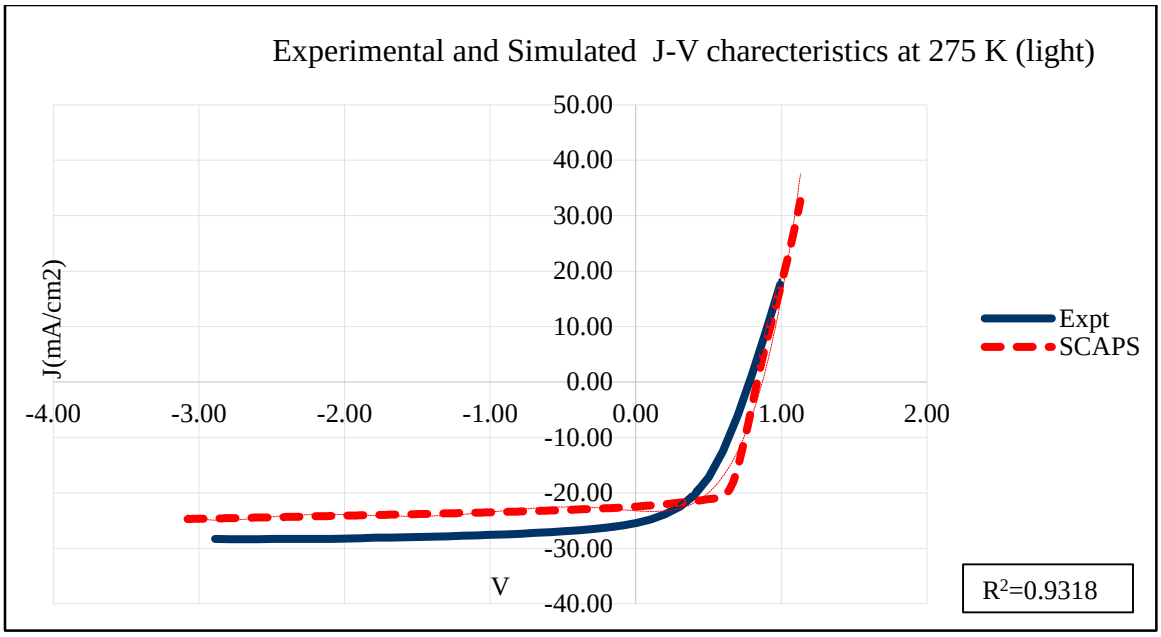

Figure 4.46 J-V curves fitting (light) of nw-CdS/CdTe device at 275K

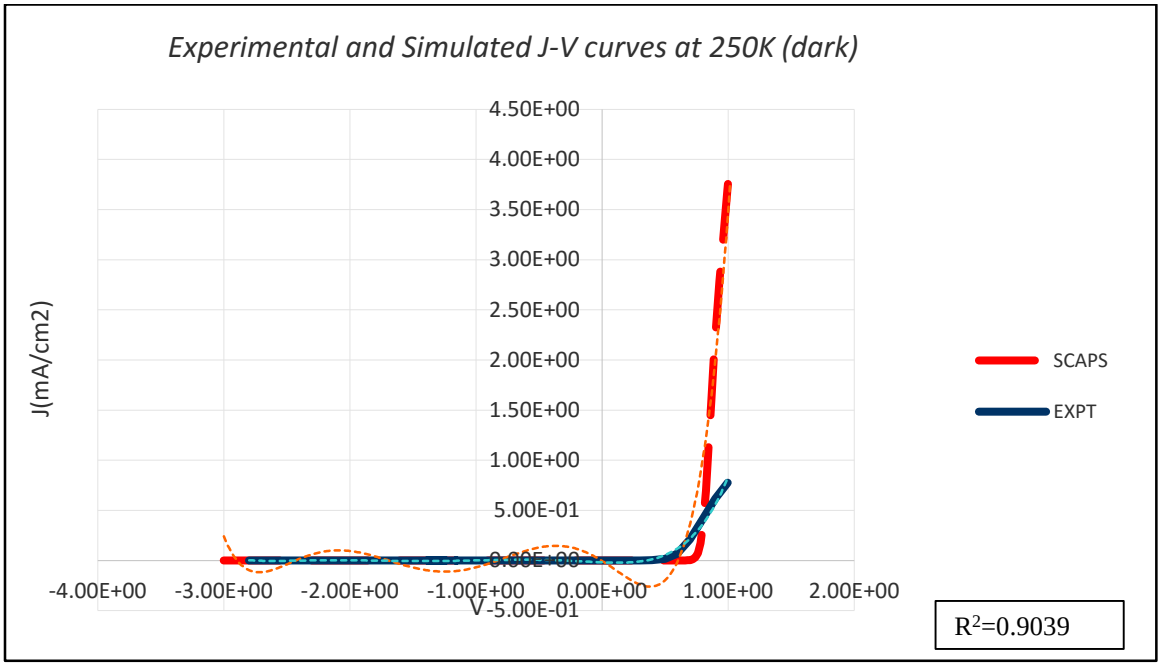

Figure 4.47 J-V curves fitting (dark) of nw-CdS/CdTe device at 250K

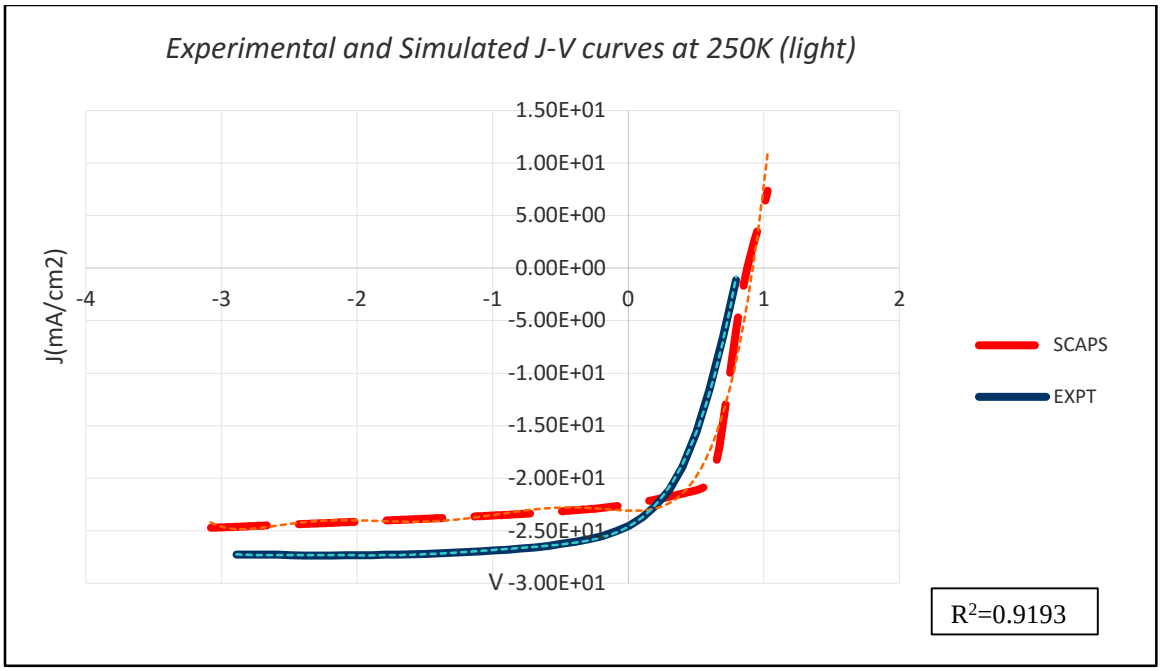

Figure 4.48 J-V curves fitting (light) of nw-CdS/CdTe device at 250K

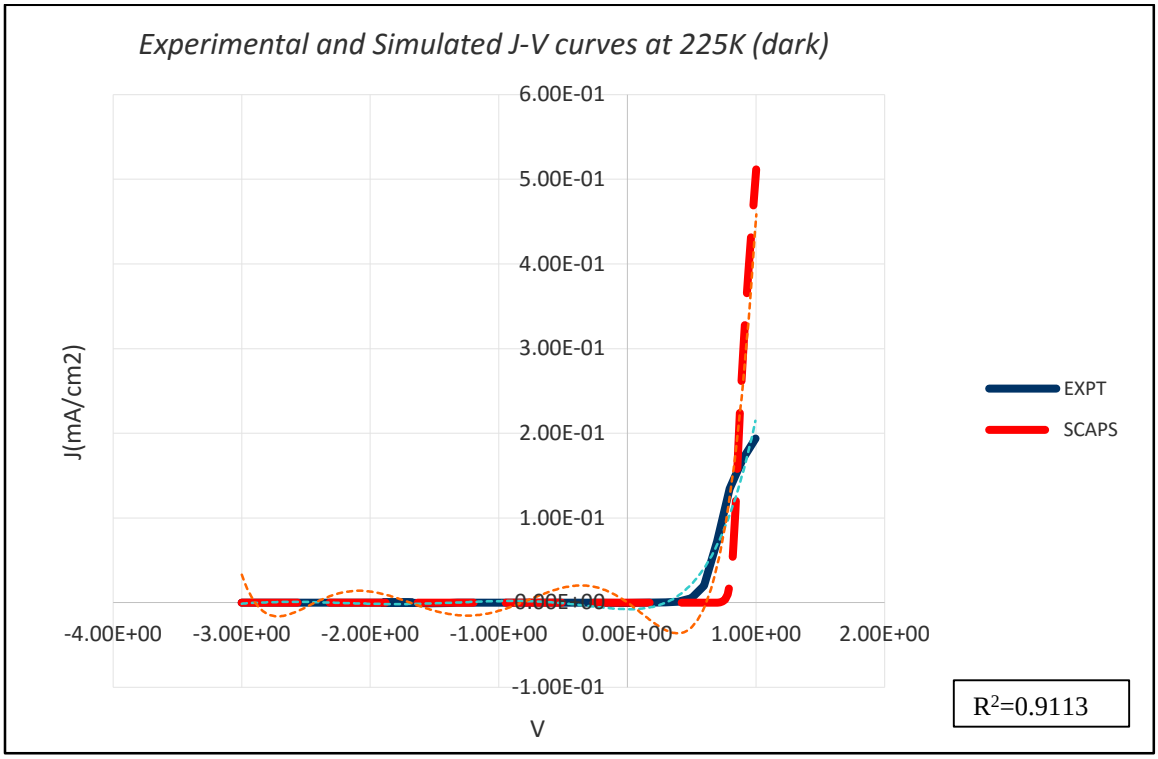

Figure 4.49 J-V curves fitting (dark) of nw-CdS/CdTe device at 225K

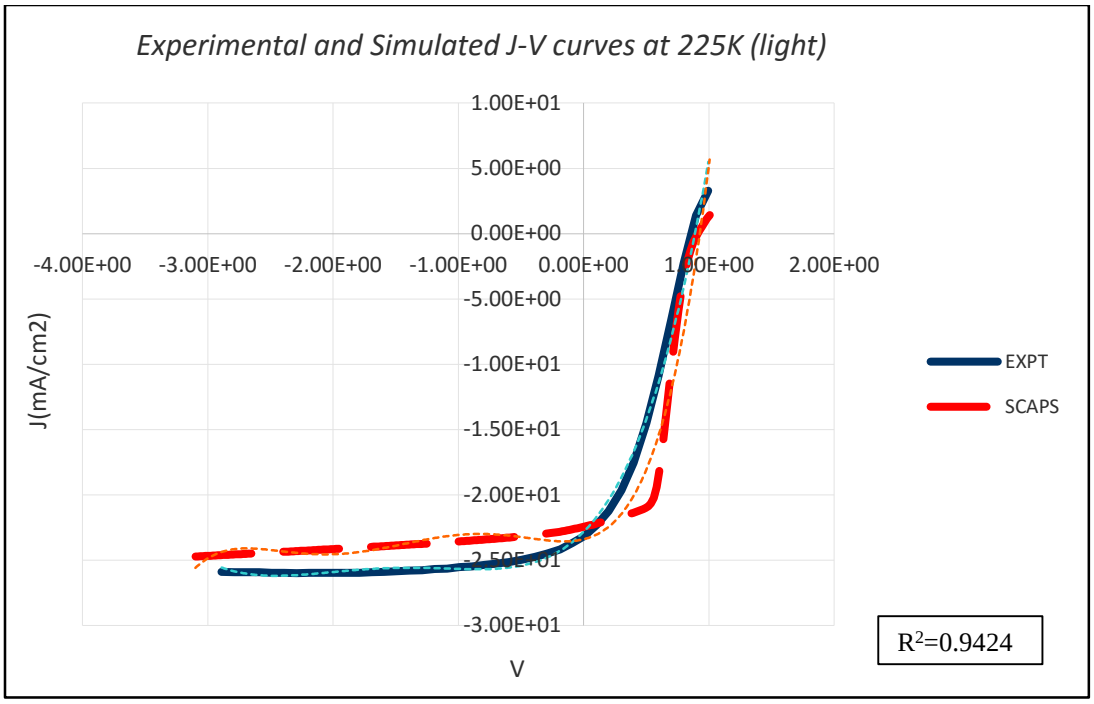

Figure 4.50 J-V curves fitting (light) of nw-CdS/CdTe device at 225K

The above figures show that the simulated curves are similar to the experimental curves obtained at various temperatures.

The variations in the simulated results can be attributed to the following reasons:

(1) The parameters for thin layer CdS in SCAPS-1D have been optimized for nanowire CdS embedded in AAO membrane.

(2) Various defects might be actually present in the device. In the simulation, only acceptor level defect in CdTe was considered along with the acceptor level defect in the interface of nw-CdS and CdTe layers.

(3) SCAPS-1D treats energy bandgap and mobilities as temperature independent. However, both the parameters are actually temperature dependent. [5]

4.3 Crossover Effect

The crossover effect is generally observed in CdTe solar cells. At higher forward bias, the light current-voltage characteristic crosses over and reaches above the dark current-voltage characteristic. The crossover effect has been attributed to various causes including,

(i) The photoconductivity effect; the bulk resistance of both CdS and CdTe is reduced when sunlight is shined on them. This leads to reduced series resistance and hence higher light current compared to the dark current is observed at voltages higher than the crossover point.

(ii) Sensitivity of the CdS-CdTe heterojunction to the sunlight radiation; electron occupation of interface states and traps near the junction alters when sunlight falls on the device. This leads to a reduced junction potential barrier under illumination and hence higher light current compared to the dark current is observed at voltages higher than the crossover point.

(iii) Sensitivity of the CdTe-Graphite Schottky diode junction to the sunlight radiation; some sunlight generated electrons reach the interface between the CdTe layer and the graphite electrode, and then recombine via surface states. This increases the value of the effective reverse saturation current (j_0) in light compared to the value of (j_0) in the dark, and leads to higher light current compared to the dark current at voltages higher than the crossover point. The simulations done by Burgelman et. al., in SCAPS-1D, have indicated that the crossover effect occurred due to the minority carrier recombination at metal/CdTe contact. [28] This recombination current is directly proportional to the illumination intensity. This needs to be added to the dark saturation current of the back diode. Thus, the total recombination current at illumination is higher than the dark, at a given voltage. It is negligible at low bias. However, it may become comparable with the back contact saturation current at higher bias.

(iv) Sensitivity of the CdS/ i-SnO_2 junction to the sunlight radiation; some sunlight generated electrons reach the interface between the CdTe layer and i-SnO_2

layer, and then recombine via traps and interface states. This increases the value of the effective reverse saturation current (j_0) in light compared to the value of (j_0) in the dark, and leads to higher light current compared to the dark current at voltages higher than the crossover point.

In our study, we focused on the fourth effect. The following curves represent the J-V curves (dark and light) at 300K. Here, we see the crossover is starting to appear from Fig. 4.52 and crossover is observed at 0.96 V in fig. 4.53. Table 4.8 shows the parameters which were used for simulating these curves. The CdS thickness was reduced from 100 nm to 90 nm and the defect in i-SnO_2 layer was removed. We can conclude from here that the removal of defect in i-SnO_2 increases the Jsc at particular voltage, thus producing the crossover effect. Further, reducing the thickness of CdS layer reduced the overall resistance, thus increasing the current Jsc.

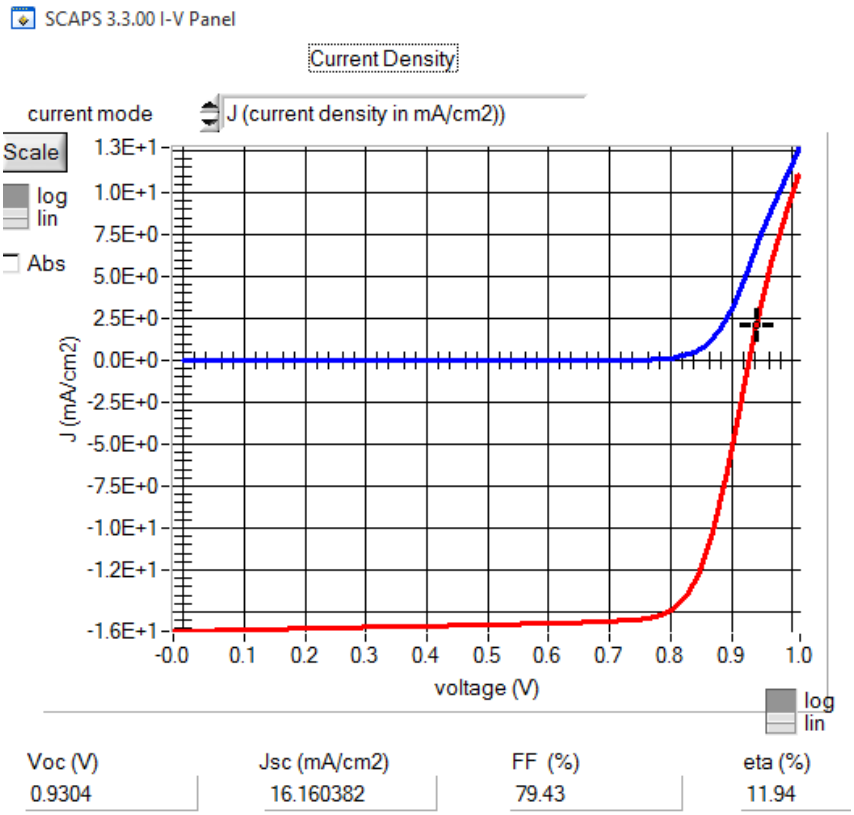

Figure 4.51 Simulated J-V curve (dark and light) at 300 K with CdS thickness-100 nm

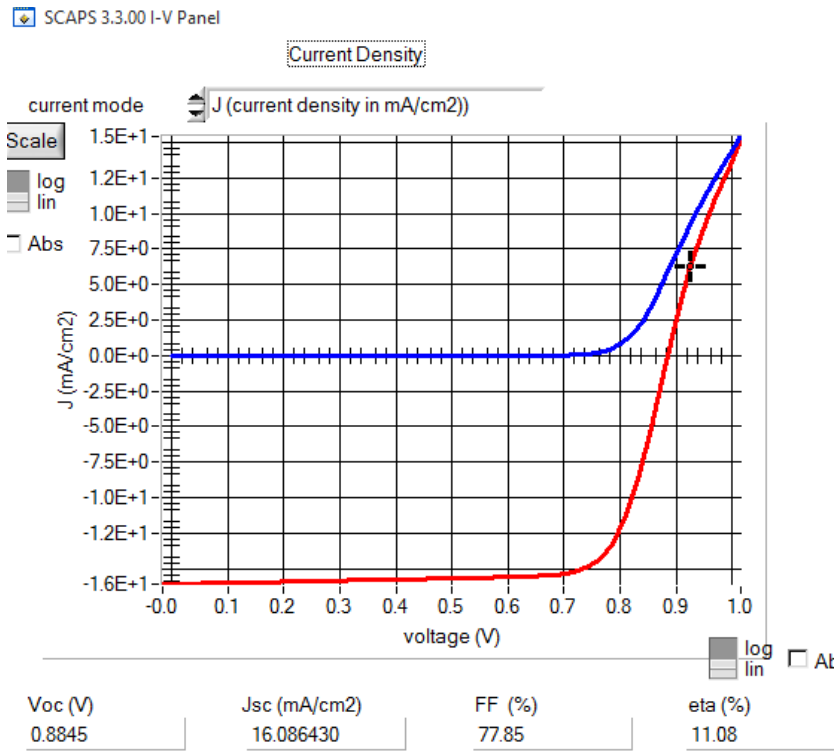

Figure 4.52 Simulated J-V curve (dark and light) at 300 K with CdS thickness-90 nm

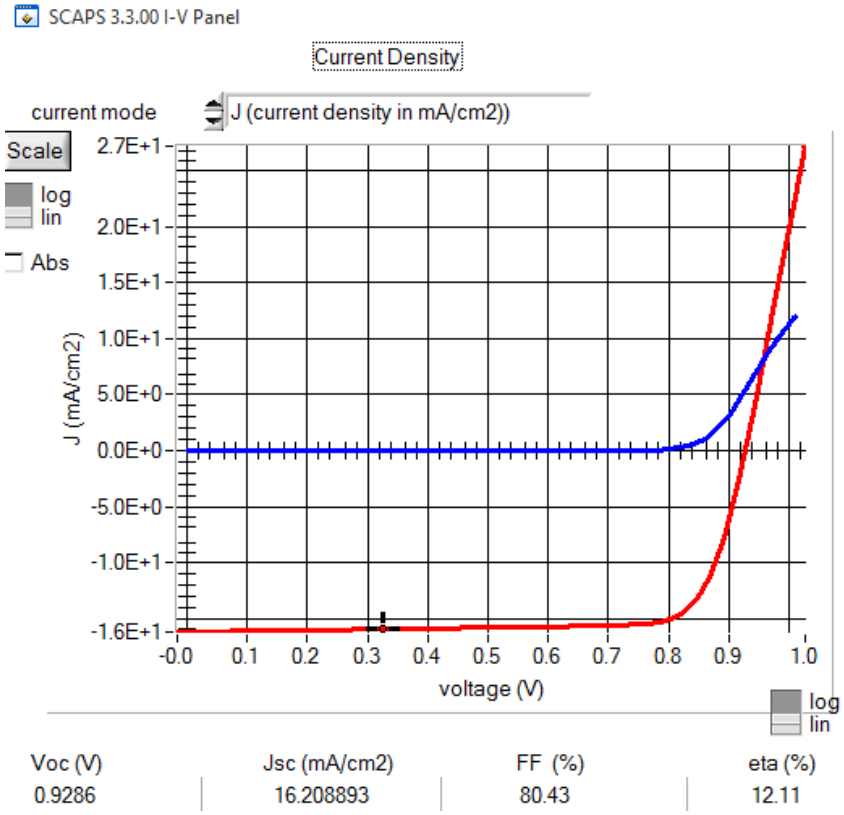

Figure 4.53 Simulated J-V curve (dark and light) at 300 K with CdS thickness-90 nm and absence of i-SnO2 defect

Table 4.8 Parameters used for explaining Crossover effect

Parameters	Figure4.17	Figure4.18	Figure4.19
CdS-nw			
thickness (µm)	**0.100**	**0.09**	**0.09**
i-SnO2			
CB effective density of states (1/cm^3)	2.200E+18	2.200E+18	2.200E+18
Defect 1 of i-SnO2			
defect type	Donor	Donor	**Removed**
capture cross section electrons (cm^2)	1.00E-15	1.00E-15	
capture cross section holes (cm^2)	1.00E-12	1.00E-12	
energetic distribution	single	single	
reference for defect energy level Et	Below Ec	Below Ec	
energy level with respect to Reference (eV)	0.2	0.2	
Nt total (1/cm^3) uniform	1.000E+15	1.000E+15	

4.4 Rollover Effect

Because of the relatively high work function of p-CdTe, it is rather difficult to make an ohmic contact to it. To achieve a conducting contact, surface of CdTe must be cleaned, etched and its chemical composition modified in such a way that becomes tellurium rich, and highly conductive at the surface. In spite of careful processing, it is not uncommon for the CdTe-top electrode contact to become a Schottky diode. Many times, the solar cell, as made has a conducting contact between CdTe and the top electrode, but the contact degrades with time into a Schottky diode type because of insufficient encapsulation and the resultant oxidation of the CdTe surface. As this happens, the solar cell begins to behave like two back-to-back diodes [28-29]. One diode is made up of the main p-n heterojunction between n-CdS and p-CdTe, and the other is the Schottky diode between the surface of p-CdTe and the top electrode, which is typically graphite, or a metal like gold (Au).

The current-voltage characteristics now display a saturation like behavior, which manifests as an S-shaped curvature in the I-V curve at high voltages. This effect, called the Rollover Effect, is illustrated in Fig. 4.54. It can be seen when the cell is the dark and also when under illumination.

In the past, the Rollover Effect in planar CdS-CdTe solar cell devices has been explained by Singh et al [29] in terms of the tunneling breakdown of the Schottky diode; as thermionic emission and shunt conductance by Stollwerk et al [30]; and as drift and diffusion by Niemegeers et al [28].

Rollover effect can be explained by two diode model. The majority carrier current transport through CdTe back contact diode is limited by thermionic emission, or by drift and diffusion in the contact space charge layer, or a combination of both. However, slope of I-V curve at forward bias cannot be explained only by thermionic emission. The reason being current limited by thermionic emission is independent of voltage at forward bias. Further, the I-V curve shows a slope beyond the rollover point, which decreases exponentially with temperature. The shunt conductance at the contact, though shows the slope of I-V curve, does not explain the temperature dependence. According to Niemegeers et al [28], the current transport across the CdTe back contact is limited by drift and diffusion. The electric field at the metal contact depends on the voltage over the contact diode, which explains the voltage dependence of the saturation current. The Boltzmann factor $\exp(-q\emptyset_B)$ explains the temperature dependence of the saturation current.

It is interesting to note that all of the three theories mentioned above, for the planar CdS-CdTe solar cell device rely upon the presence of a diode at the junction between the surface of CdTe and the top electrode. To check the validity of these theories for the nanowire CdS-CdTe device, we simulated the effect of varying the height of the Schottky barrier on the current-voltage characteristics of the solar cell. The barrier height (energy difference between the metal Fermi level and the top of the valence band) was altered from 0.5 eV to 0.4 eV. Fig. 4.54 shows the J-V curves (light) at 300 K and Table 4.9 shows parameters varied for removing the rollover effect. It is clear that the barrier

height of this Schottky diode at the CdTe surface plays a critical role in determining cell performance. The curve corresponding to the 0.5 eV barrier exhibits a strong rollover effect, while this effect has disappeared when the barrier was reduced to 0.4 eV. The fact that the 2-diode model is applicable to the nanowire CdS-CdTe-graphite solar cell as the planar CdS-CdTe-graphite cell is not surprising because the CdTe-graphite junction is the same in both cases.

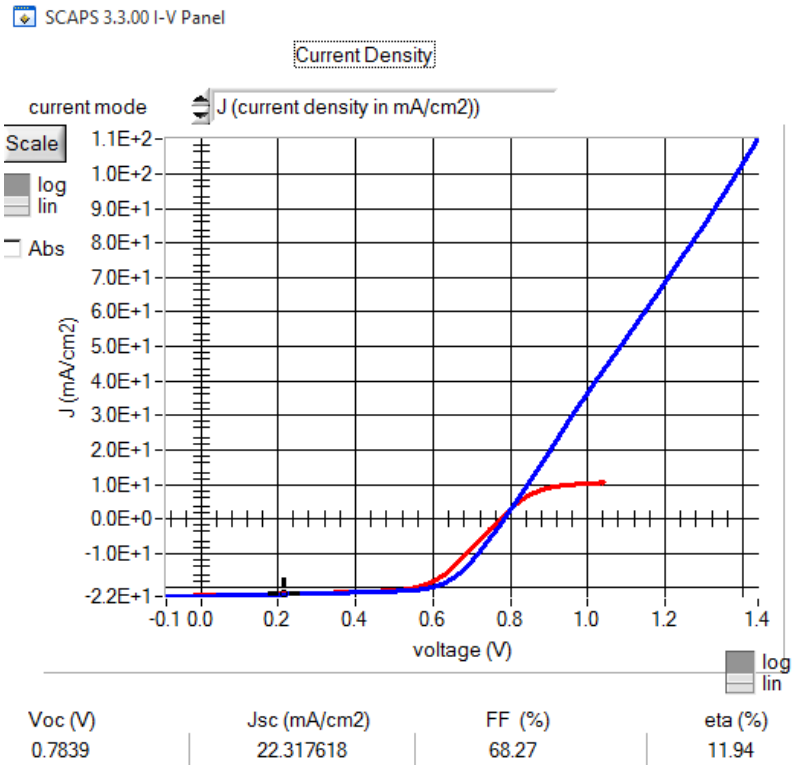

Figure 4.54 Simulated J-V curves (light) at 300 K

Table 4.9 Parameters varied for removing the rollover effect

	Red curve	Blue Curve
Majority carrier barrier height [relative to E_f](eV)	0.5	0.4
Majority carrier barrier height [relative to E_v](eV)	0.3271	0.2271

5. Conclusion and Future Work

CdS nanowires have several advantages over the planar CdS such as the improvement in open circuit voltage due to reduced junction area and improvement in short circuit current due to higher optical transmission through CdS nanowires. The modeling of the nw-CdS/ CdTe was studied by using SCAPS-1D in order to identify and evaluate the parameters responsible for improving the efficiency of this solar cell.

The effects of various parameters including interface state density, CdS and CdTe state densities, trap concentration, metal work function on light I-V curves were studied and the optimum values for these parameters were obtained in order to get the highest efficiency without convergence failure and with no crossover or rollover effect. The highest efficiency for nw-CdS/ CdTe structure obtained was 22.26% withJsc= 26.724 mA/cm^2, V_{oc}= 0.9828 V and FF=84.27 at 300K. It can be concluded here that the efficiency can be improved by improving the interface and contact properties of nw-CdS/CdTe structure. The fill factor can be improved by reducing the series resistance and increasing the shunt resistance.

The simulations for J-V characteristics of nw-CdS/CdTe solar cell were performed using SCAPS-1D for getting the curve fit with the experimental characteristics for 300 K. The experimental J-V measurements at 300 K were V_{oc}=0.770 V, J_{sc} = 26 mA/cm^2, FF=60% and the efficiency of 12%. The simulated J-V curves considered for curve fitting were at V_{oc}=0.7919 V, J_{sc} = 22.345 mA/cm^2, FF=68.27% for the efficiency of 12.08%. The same parameters were used for obtaining the simulated J-V characteristics at lower temperatures 275K, 250K and 225K. It can be concluded here that the simulated J-V characteristics were close to the experimental characteristics with R^2 >0.9 at all temperatures. The variations in V_{oc} and J_{sc} can be attributed to the defects, assumptions made in the simulations for nw-CdS parameters and SCAPS-1D does not consider parameters such as energy bandgap and mobilities as temperature dependent.

Further, it was observed that the present simulated model explains the important effects of the nw-CdS/CdTe solar cell such as crossover and rollover effect. The crossover effect

was studied by considering the sensitivity of CdTe/i-SnO_2 under illumination. It was shown that the removal of defect in i-SnO_2 is responsible for producing the crossover effect.

The rollover effect has been explained by using back to back diode model in the literature and the simulations were performed in order to validate this theory. It was shown that the change of barrier height at the contact is a critical parameter in the rollover effect. Once the majority carrier barrier height was varied from 0.4 to 0.5 eV, the curve corresponding to the 0.5 eV barrier showed a strong rollover effect, while this effect was disappeared when the barrier was reduced to 0.4 eV.

Overall, it can be concluded that SCAPS-1D model, which is modeled for thin film solar cells, is able to provide the realistic simulation for nw-CdS/CdTe solar cells.

For future work, C-V and external quantum efficiency (EQE) characteristics can be simulated, studied and the results can be compared with the experimental obtained data.

References

[1] Renewable Energy Policy Network for the 21st Century (Ren21), "Renewables 2015 Global status report". Available from: http://www.ren21.net/status-of-renewables/global-status-report/ (2015)

[2] Agency, I.E., Medium-Term Renewable Energy Market Report 2014, Paris (2014)

[3] Agency, I.E., Technology Roadmap: Solar Photovoltaic Energy (2014)

[4] Vesselinka Petrova-Koch, Rudolf Hezel, Adolf Goetzberger, "High –Efficient Low-Cost Photovoltaics: recent Developments", Springer series in optical sciences (2008)

[5] S.M. Sze, K. K. N., "Physics of semiconductor devices" (2007)

[6] Laboratory, N. R. E., "solar cell efficiency chart", Available from: http://www.nrel.gov.ncpv (2015)

[7] Department, E., http://energy.gov/eere/energybasics/articles/photovoltaic-cell-quantum-efficiency-basics (2016).

[8] Photovoltaic Education Network, http://pveducation.org/pvcdrom/solar-cell-operation/quantum-efficiency (2016)

[9] Purnomo Sidi Priambodo, Didik Sukoco, Wahyudi Purnomo, Harry Sudibyo and Djoko Hartanto (2013). Electric Energy Management and Engineering in Solar Cell System, Solar Cells - Research and Application Perspectives, Prof. Arturo Morales-Acevedo (Ed.), ISBN: 978-953-51-1003-3, InTech, DOI: 10.5772/52572. Available from: http://www.intechopen.com/books/solar-cells-research-and-application-perspectives/electric-energy-management-and-engineering-in-solar-cell-system

[10] Hongmei Dang, "Nanostructured Semiconductor Device Design in Solar Cells", Ph.D. Thesis, University of Kentucky (2015). Available from: http://uknowledge.uky.edu/ece_etds/77/

[11] Marc Burgelman, Johan Verschraegen, Stefaan Degrave and Peter Nollet," Modeling Thin-film PV Devices", Progress in Photovoltaics: Research and Applications, **12**, 143–153 (2004)

[12] M. S. Lundstrom, "Numerical Analysis of Silicon Solar cells" (1980)

[13] J. L. Gray, "A computer model for the simulation of thin-film silicon-hydrogenalloy solar cells," IEEE Transactions on Electron Devices, **36**, 906-912 (1989)

[14] E. K. Banghart, "Physical mechanisms contributing to nonlinear responsivity in silicon concentrator solar cells" (1989).

[15] P. D. DeMoulin and M. S. Lundstrom, "Projections of GaAs solar-cell performance limits based on two-dimensional numerical simulation," IEEE Transactions on Electron Devices, **36**, 897-905 (1989).

[16] Analysis of Microelectronic and Photonic Structures (AMPS) software, developed at Pennsylvania State University. Also, see http://www.psu.edu/dept/AMPS

[17] Schropp R, Zeman M., "Amorphous and Microcrystalline Silicon Solar Cells" Kluwer: Boston, (1998).

[18] Basore P., "Numerical modeling of textured silicon solar cells using PC-1D", IEEE Transactions on Electron Devices, **37(2),** 337 (1990).
[19]Burgelman M., Nollet P., Degrave S. , "Modeling polycrystalline semiconductor solar cells", Thin Solid Films; 361–362, 527–532 (2000). Also, see http://www.elis.ugent.be/ELISgroups/solar/projects/scaps.html
[20] Burgelman M., Gillis S., Niemegeers A., "A user program for realistic simulation of polycrystalline heterojunction solar cell: SCAPS-1D", Proceedings of the 2nd world conference on photovoltaic solar energy conversion, JRC, European Commission, Juli, 672-675 (1998)
[21] Saeed Khosroabadi, Seyyed Hossein Keshmiri, "Design of a high efficiency ultrathin CdS/CdTe solar cell using back surface field and backside distributed Bragg reflector", Optics Express, **22**, Issue S3, A921-A929 (2014)
[22] M. Burgelman, A. Niemegeers, "Effect of the Au/CdTe back contact on IV and CV characteristics of Au/CdTe/CdS/TCO solar cells", Journal of applied physics,**81(6)**,2881-2886 (1997)
[23] Nowshad Amin, Kamaruzzaman Sopian, Makoto Konagai, "Numerical modeling of CdS/CdTe and CdS/CdTe/ZnTe solar cells as a function of CdTe thickness", Solar Energy Materials & Solar Cells, **91**, 1202–1208 (2007)
[24] M. Gloeckler, A.L. Fahrenbruch, J. R. Sites, "Numerical Modeling of CIGS and CdTe solar cells: setting the baseline", 3rd world conference on photovoltaic energy conversion, Osaka, Japan, **1**,491-494 (2003)
[25] Hongmei Dang, V. P. Singh, Sai Guduru, J. T. Hastings, "Embedded nanowire window layers for enhanced quantum efficiency in window-absorber type solar cells like CdS/CdTe", Solar Energy Materials and Solar Cells,**144**,641-651 (2016)
[26] Alex Niemegeers, Marc Burgelman, Koen Decock, Johan Verschraegen, Stefaan Degrave, "SCAPS-1D Manual", version 2, March (2015). Available from: http://scaps.elis.ugent.be/
[27] H. J. Pauwels and G. Vanhoutte, "The influence of interface states and energy barriers on the efficiency of heterojunction solar cells", Journal of Physics D: Applied Physics, **11(5)**, 649-667 (1978)
[28] M. Burgelman, A. Niemegeers, "Numerical Modelling of ac characteristics of CdTe and CIS solar cells", Proc.25th IEEE Photovoltaic Specialists Conference (Washington D.C., April 1996), 901-904, IEEE, New York (1996)
[29] V. P. Singh, O.M. Erickson and J. H. Chao, "Analysis of contact degradation at the CdTe-electrode interface in thin film CdTe-CdS solar cells", J. Appl. Phys. **78**, 4538 (1995); http://dx.doi.org/10.1063/1.359796olwerck
[30] J. Stollwerck and J. R. Sites, "Analysis of CdTe Back Contact Barriers", Proceedings of the 13th European PVSEC, Nice, 2020 (1995)

Vita

Rasika Ganvir was born in Nagpur, India. She earned her Bachelors in Electrical Engineering from National Institute of Technology, Durgapur, India in May 2008. She worked for five years in NTPC Ltd., India. After receiving the PEIK scholarship, she joined the Master's program at University of Kentucky in August 2013. She is currently working as a Systems Engineer at Cummins Inc., Fridley, Minnesota.